Optical and Magnetic Approaches to Microfluidic Blood Diagnostics

Nikita Taparia

A dissertation

submitted in partial fulfillment of the

requirements for the degree of

Doctor of Philosophy

University of Washington

2020

Reading Committee:

Nathan Sniadecki, Chair
Alberto Aliseda
Nathan White

Program Authorized to Offer Degree:

Mechanical Engineering

University of Washington

Abstract

Optical and Magnetic Approaches to Microfluidic Blood Diagnostics

Nikita Taparia

Chair of the Supervisory Committee:
Nathan Sniadecki
Mechanical Engineering

Critical bleeding manifests in cardiovascular disease and trauma. As a patient bleeds, there is a loss of red blood cells, responsible for the delivery of oxygen throughout the body, and this loss is known as anemia. In trauma patients, a stable clot must form to stop bleeding. Conversely, stiff clots can form occlusions in blood vessels, which leads to stroke or myocardial infarction. Thus, evaluating platelet function could improve our understanding of a bleeding risk. The goal of this dissertation is to develop an approach that can potentially assess anemia and bleeding risks for a patient. To address this, I have split this dissertation into four aims. **Aim 1:** A microfluidic approach was taken to detect anemia in whole blood. Specifically, with this approach, severe and moderate anemia levels can be detected accurately. The use of a microfluidic device allows this approach to be rapid, use low volume of blood, and easily integrated with other blood diagnostic microfluidic approaches. **Aim 2:** An optical benchtop platform was developed

to measure the platelet forces in a microfluidic assay. The benchtop platform detected significant differences in platelet forces for patients that undergo blood transfusion within 24 hours of hospital admittance and those who did not undergo blood transfusion and healthy controls. **Aim 3**: Magnetic microscale actuators were integrated into the platelet force assay. A refined technique to embed iron particles into microstructures was explored and a new way to actuate the magnetic posts was designed and modeled. **Aim 4:** Using the assay developed in Aim 3, the mechanobiology of platelet-rich plugs during formation was investigated. The results from the assay indicated that plugs stiffen in response to the contractile force of platelets and the applied force from magnetic actuators.

TABLE OF CONTENTS

LIST OF FIGURES

LIST OF TABLES

ACKNOWLEDGEMENTS

I would like to thank my committee chair and lab PI Nathan Sniadecki for believing in a physics undergraduate to conduct biological research despite the lack of experience, and for all the guidance and support during my time at University of Washington. For the work presented in Chapter 3, I would like to thank Kimsey Platten and Kristin Anderson for their help in conducting experiments and analyzing results. For the work presented in Chapter 4, I would like to thank Lucas Ting and Shirin Feghhi for mentoring me as a new graduate student with little experience in blood research and allowing me to work on their innovative microfluidic assay. Additionally, I would like to thank Annie Smith, who assisted me in blood experiments, and Ari Karchin, who developed the heating unit of the prototype. I would also like to thank Esther Lim, Alex St. John, and Xu Wang for their work on the trauma study. For the work in Chapter 5, I would like to thank Nakul Sridhar for working on the actuation device and Teagan Mach and Ava Obenaus for their help in conducting and analyzing experiments. Special thanks to Dominic Chung for providing the ADAMTS13 during these experiments. Finally, I would like to thank the rest of my committee members: Nathan White, Alberto Aliseda, Wendy Thomas, and Lilo Pozzo for their support and advice on my research.

To the Cell Biomechanics lab, past and present members, thank you for creating an engaging workplace environment and for the endless entertaining conversations about absolutely everything imaginable.

To every student I ever taught, under the guidance and supervision of Jim Parnell and Ken Yasuhara, thank you for making me a better teacher.

To my family, thank you for the constant love and support. To my dad and mom, who taught me to color inside and outside of the lines, respectively. My curiosity, creativity, and love for learning comes directly from the both of you. Lastly, I would like to dedicate this dissertation to my late grandfather, Dr. H.C. Chowdhary, the only other Ph.D. in the family. I am so happy to be able to follow in your footsteps.

1. Introduction

Anemia, cardiovascular disease, and trauma are all associated with critical bleeding problems [1, 2]. Specifically, anemia affects a quarter of the world's population and is a result of many different factors including iron deficiency, malaria, and genetic disorders [3-6]. Cardiovascular diseases are the leading cause of death worldwide [7]. Trauma accounts for 10% of the deaths worldwide and is the primary cause of death for people under the age of forty years [8]. Because of these three major disease categories, blood assessment for critically ill patients specifically focuses on the identification of anemia and minimization of blood loss. **Thus, the goal of this dissertation is to develop an approach that can potentially assess anemia and bleeding risks for a patient.**

A rapid assessment to determine the level of anemia and bleeding risks in a critically ill patient requires a low volume of whole blood. To detect anemia, our approach must measure hemoglobin concentration. Hemoglobin is a protein within red blood cells that is responsible for oxygen transportation. Any critical bleeding can lead to inadequate oxygen delivery due to the lack of red blood cells, which leads to organ dysfunction, and eventually, death [9, 10]. To detect bleeding risks, our approach must assess platelet function. Platelets are important in hemostasis, or the physiological process to stop bleeding [11]. Specifically, platelets adhere, activate, and aggregate at a wound site to form a contractile platelet-rich plug. Recently, our lab focused on a microfluidic approach to measure platelet forces of an aggregate formed solely from shear activation and adhesion to collagen in whole blood [12]. This microfluidic approach is rapid and uses a small volume of blood but requires a fluorescence microscope with a high magnification oil lens, which is not ideal in a clinical setting.

The first part of this dissertation has two aims: (1) to develop an approach to detect anemia in whole blood and (2) to develop a clinically translatable platform to measure the platelet forces. Like previous methodologies, the main indicator of hemoglobin differences was based on optical transmission of green light [13, 14]. However, unlike these methods, this research measured the optical transmission through whole blood with different levels of hemoglobin. The microfluidic channel height and the flow conditions are varied to illustrate the capabilities of this detection method. Specifically, a nonlinear model for optical transmission of light through whole blood was adapted to determine the predictability for different levels of anemia. For the second aim, this research changed the transmission optics of the first aim to be fluorescence simply by inserting a TRITC emission filter. First, the resolution and field-of-view were quantified. Then, the measurement of platelet forces was compared between this method and a fluorescence microscope. Finally, this optical benchtop detection method was used in a prospective cross-sectional observational study of trauma patients. The platelet forces were compared between healthy controls and trauma patients who did and did not require transfusions within 24 hours.

While platelet forces are a good indicator for bleeding risk for clinicians, there is also value in understanding the response of a platelet-rich plug to external forces. Trauma patients require a stable thrombus to stop bleeding but as their blood pressure is restored from a hypotensive state due to fluid resuscitation, the bleeding reoccurs because the force “pops the clot” [15]. From a cardiology standpoint, arterial thrombosis forms a predominantly platelet-rich occlusive thrombus, which can lead to a stroke or myocardial infarction. In other words, trauma patients require a thrombus that can withstand the hemodynamic forces while cardiology patients could benefit from a thrombus of less stiffness. Moreover, studies have shown that platelets sense mechanical cues and respond through their adhesion, activation, aggregation, and contractile force [16-19]. However, most of these studies focused on single platelets and there is a lack of focus of the role of mechanotransduction by platelets in the context of early hemostasis.

Thus, the second part of this dissertation has two aims: (3) to integrate actuators into the platelet force assay and (4) to investigate the mechanobiology of platelet-rich plugs. Magnetic approaches have been used in the past to study the material properties of cells, gels, and clots [20-22]. In this research, a methodology was developed to embed magnetic iron microparticles into the force sensors presented in aim 2. Instead of utilizing previous methods for actuation, such as electromagnetic coils or a bar magnet, this research rotated a multipole ring magnet, which switches its magnetic dipole moment every ninety degrees. With this new system, the contractile force of platelets and stiffness during plug formation were measured simultaneously. Additionally, the mechanotransduction response of these plugs was evaluated by applying dynamic loading.

The development of a microfluidic platform with benchtop optical detection and magnetic actuation allows for rapid assessment of anemia and bleeding risks for a critically ill patient. Quantifying the force and stiffness of platelet-rich plug during formation can lend insight on the effect of blood transfusions and antiplatelet therapies. Because all studies are done in a microfluidic setting with whole blood, there is further potential to integrate the techniques presented here towards one novel diagnostic tool for hematological assessment.

2. Background

The purpose of this chapter is to provide an adequate biological and technical background for this dissertation. Blood comprises primarily of red blood cells (45%), white blood cells (> 1%), platelets (> 1%), and plasma (55%). Assessment of bleeding risk and blood transfusion products focus on everything other than the white blood cells, which are responsible for fighting infections. Therefore, the background will cover red blood cells and platelets/plasma, their natural functions in the body, and disease states. In addition, I will address some of the tools and innovations used to detect anemia and assess platelet function.

2.1 Red Blood Cells and Anemia

Erythrocytes, more universally known as red blood cells (RBC), transport and distribute oxygen from the lungs to the tissue within the body. These cells are highly deformable, allowing them to squeeze through blood vessels of smaller diameter, because of their biconcave disc shape and flexible plasma membrane. They lack a nucleus and other organelles typical of other cells, which means they cannot repair themselves. Instead, old RBCs are removed by the spleen and new ones are formed in the bone marrow, upholding a lifespan of approximately 120 days. While they do not have these organelles, RBCs are enriched with a high concentration of hemoglobin.

Hemoglobin is the protein that contains four oxygen-binding iron atoms. When blood loss occurs, there is a decrease in RBCs and consequently, hemoglobin. As a result, the blood suffers a decline in its ability to transport oxygen and this is known as anemia. Because of the impaired oxygen delivery, those who suffer from mild anemia have symptoms such as fatigue, dizziness, and shortness of breath [9, 10]. The lack of oxygen to the tissues can lead to organ failure. In very severe cases, the body increases cardiac output to transport more oxygen and this leads to symptoms of heart failure. For this reason, the severity of anemia is defined by hemoglobin concentration.

Anemia can also manifest due to RBC dysfunction or increased hemolysis. For instance, impaired production can occur in those who suffer from iron deficiency or a genetic disorder known as thalassemia. Iron deficiency is the most common form of anemia and it occurs not only during blood loss but from low dietary intake due to malnutrition [23]. Because hemoglobin formation depends on iron, a depletion results in abnormal red blood cells. Thalassemia occurs due to different types of mutations that target the formation of adult hemoglobin and the production of healthy RBCs. In contrast to blood loss and decreased production of RBCs, increased breakdown can also lead to anemia. In diseases like malaria, plasmodium, a parasite, infects RBCs and this can cause hemolysis and eventual organ failure [3]. Sickle cell disease is a genetic disorder due to a point mutation and as a result, abnormal hemoglobin forms, distorting the shape and elasticity of the RBCs [24]. The hemoglobin fails to deliver oxygen and the cells occlude vessels due to their inability to deform easily. Additionally, while normal RBCs have a lifespan of 120 days, sickle cells last only 10 to 20 days in the body.

As mentioned earlier, anemia severity is based on hemoglobin concentration. Normal blood typically has a hemoglobin concentration of 12 g/dL to 20 g/dL. Mild anemia is 10-12 g/dL, moderate anemia is 8-10 g/dL, and severe anemia is less than 8 g/dL [10]. In clinical settings, RBC transfusion guidelines tend to target those suffering from severe and moderate anemia, but the threshold is also dependent on the type of injury [25].

2.2 Techniques to Detect Hemoglobin for Anemia

Hematology analyzers measure hemoglobin concentration as part of a complete blood count (CBC) panel. Specifically, RBCs in a sample are lysed to release their hemoglobin. Then, hemoglobin is chemically converted to a stable form, cyanmethemoglobin, for optical detection [26]. By measuring the optical absorption of hemoglobin at a wavelength of 540 nm, the analyzer can detect the concentration because from Beer-Lambert law, the light absorbance at 540 nm is proportional to the hemoglobin concentration in a sample [13, 14]. While this method is accurate and reliable, it is expensive and rarely used in resource-poor regions, where anemia cases are the most prevalent [9].

In recent years, research efforts have focused on portable and affordable tests for these regions. While each of these methods still rely on the optical absorption of hemoglobin, they differ in how they process a blood sample. For example, a portable hemoglobinometer measures light transmission through a chemical-laced cuvette of blood [27]. Light transmission was also measured using the built-in camera sensor in a smartphone [28, 29]. Alternatively, some methods perform colorimetric analysis on treated blood absorbed onto paper [30, 31]. Also, a centrifugal microfluidics platform uses rigorous mixing of whole blood and chemicals prior to optical readouts [32]. All of these techniques can measure hemoglobin but still require the hemolysis of whole blood.

For some special cases of anemia, there have been separate efforts to diagnose blood diseases in microfluidic assays by measuring the deformability of RBCs [33, 34]. By measuring the mechanical properties of RBCs, a microfluidic assay can determine if a patient suffers from malaria or sickle-cell disease [35]. While high-risk subpopulations have been identified from hemoglobin concentration measurements, global health communities acknowledge that the reduction of anemia burden requires more detailed epidemiology which can lead to targeted treatment [35, 36]. Avoiding the process of hemolysis would be a step towards an integrated diagnostic platform for anemia and other blood-related conditions. Thus, the work presented in this dissertation will focus on utilizing microfluidics to detect anemia in whole blood [37].

2.3 Platelets in Hemostasis and Thrombosis

The blood coagulation system is primarily responsible for healing the body in event of an injury. An external or internal wound triggers an early response from platelets to form a plug, which also initiates the coagulation cascade to stem bleeding. The cascade maintains a balance between anticoagulant and procoagulant mechanisms. In severe cases of injury, the intrinsic pathway of the cascade become dysfunctional, which can lead to coagulopathy or hemorrhagic shock. Alternatively, genetic mutations that affect the coagulation system can result in bleeding disorders such as Von Willebrand disease or Bernard-Soulier syndrome. In a hospital setting, it is important to detect any imbalance in the coagulation system to determine if a patient needs a blood transfusion of red blood cells, platelets, or clotting factors. Therefore, it would be beneficial to develop a method to evaluate the hemostatic response to aid decision-making from doctors for better treatment.

Platelets preferentially bind in areas with disturbed flow such as vessel wall damage, partial occlusions, or extreme bends [38, 39]. Tensile forces from the shear (5000 s^{-1}) unfolds the globular structure of von Willebrand factor (VWF), a multimeric plasma glycoprotein, exposing its binding sites for platelet adhesion and the extracellular matrix [40, 41]. Shear also fosters VWF monomers self-association, increasing its length and platelet binding affinity. To prevent uncontrollable growth, a metalloprotease enzyme ADAMTS13 (a disintegrin and metalloproteinase with a thrombospondin type 1 motif, member 13) cleaves unfolded VWF at its A2 domain, thereby reducing its hemostatic potential [42-46].

Upon unfolding, VWF will bind to exposed collagen and promote the initial adhesion of platelets. These hemodynamic forces mechanically stimulate the bond between the A1 domain of VWF and the platelet adhesion receptor GPIbα [47-49]. The receptor-ligand bond between VWF-GPIb has low bond lifetime to quickly capture and engage platelets in flowing blood. However, the rapid association/dissociation rate causes platelets to roll on the surface rather than permanently adhere to it [50]. Other receptor-ligand bonds such as GPVI to collagen and αIIbβ3 to fibrinogen are necessary for stable, irreversible adhesion. In fact, the mechanical stimulation of GPIb is known to upregulate the intermediate activation of αIIbβ3, to aid this process [19, 48].

Upon adhesion, platelets release calcium, adenosine diphosphate (ADP), fibrinogen, and blood clotting factors from their granules, in phase known as activation. Platelets undergo a shape change and myosin-based internal contraction because of the calcium release [51]. Soluble agonists like ADP and the generation of signal molecules like thromboxane A2 (TxA_2) help recruit neighboring platelets and promote the full activation of αIIbβ3. The αIIbβ3 and fibrinogen bond helps facilitate platelet-

platelet cohesion. The platelet aggregate continues to compact in order to seal a wound site. The blood clotting factors help trigger the coagulation cascade to produce thrombin, which helps convert fibrinogen into fibrin. The cascade promotes the formation of a fibrin meshwork to aid in the long-term stability of the clot but also produces an anticoagulant factor to aid in fibrinolysis and prevent uncontrollable growth.

A plug must withstand the force from the blood pressure and any fluid resuscitation [52, 53]. In arterial thrombosis, a stiff platelet-rich aggregate occludes a blood vessel, which can lead to a stroke or myocardial infarction. Additionally, an unstable thrombus can form smaller fragments that break off due to the hydrodynamic forces, which then leads to pulmonary embolism. In contrast, platelet dysfunction from trauma-related injury or genetic disorders can result in soft and weak plugs, leading to critical bleeding. Furthermore, cardiovascular patients are often prescribed antiplatelet drugs to target platelet adhesion and agonist receptors, preventing total occlusion of a blood vessel. Thus, the platelet forces and the stiffness of a plug during its formation could be a valuable metric in a surgical or clinical setting.

Intravital microscopy of vascular injuries in mice revealed that a platelet-rich plug forms a core and a shell, which is distinguishable by the packing density or porosity [54-57]. The core has a dense packing of platelets, which is able to trap soluble molecules, especially as activated platelets continue to contract. The shell is much more porous and this difference in packing density affects the transport rates and distribution of platelet agonists within the plug. The core retained a high concentration of thrombin and the shell exhibited a gradient of ADP and TxA_2. As a result, there is a heterogeneity amongst platelets in terms of their level of activation and their contractile state.

Platelets also sense their mechanical environment, which dynamically changes due to the heterogeneity of the plug and the hemodynamic forces. Individual platelets sense stiffer environments and respond with enhanced adhesion, spreading, activation, and contraction [58, 59]. Platelet also modulate their fibrin-based architecture through their contraction [60], thereby influencing the overall stiffness of the clot [61]. The degree of contraction also controls the rate of fibrinolysis [62]. Together, this indicates that the mechanotransduction of platelets affects the overall biomechanics of a plug and can potentially help predict the overall hemostatic response, but this phenomenon is poorly understood.

Therapeutic drugs often target platelets because they are the primary mediators of hemostasis. Arterial platelet/VWF-rich clots are resistant to lysis with tissue plasminogen activator (tPA), a drug that activates plasmin to promote fibrin degradation [63]. However, the addition of ADAMTS13 proved more effective to reduce infarction volume and restore blood flow in mice. While there is interest in ADAMTS13 in the context of hemostasis and therapy, its role during shear-mediated platelet plug formation has not been characterized.

Based on animal and human models, low ADAMTS13 activity and high VWF levels may be key indicators for cardiovascular pathologies such as ischemic stroke, arterial thrombosis, atherosclerosis, and myocardial infarction [64-67]. Furthermore, an ADAMTS13 deficiency leads to thrombotic thrombocytopenic purpura (TTP), a microangiopathic disorder. If untreated, the large size of VWF promotes spontaneous formation of platelet-rich microthrombi, which can cause organ failure or death. In contrast, von Willebrand disease is a genetic bleeding disorder that either creates dysfunctional VWF or depletes the overall quantity [40]. Thus, a platelet function assay sensitive to VWF and ADAMTS13 could have broader impact.

2.4 Techniques to Study Platelet Function

To assess hemostasis, tests typically focus on the coagulation response for whole blood after it is externally stimulated with an agonist. Clinicians use a PT/INR test to diagnose bleeding disorders or response to antiplatelet therapies by measuring how long it takes to initiate aggregation in plasma. It typically takes approximately 12 seconds to conduct a test, but it is limited to the extrinsic pathway of the coagulation cascade. Multiple electrode aggregometry measures the impedance change in plasma and utilizes agonists to examine the response from many platelet receptors, making it more functional. However, both of these tests rely on only assessing aggregation in static conditions, which is not as physiological.

Clinicians use viscoelastic tests, such as thromboelastography (TEG) to measure the dynamics of a blood clot and treat patients more effectively. These devices contain two parts: a cup and a probe. In TEG, a heated cup with whole blood slowly rotates freely against a stationary probe. As clotting begins, fibrin strands develop and help form a connection between the cup and probe, which can then measure the torsion. The strength of a clot and speed of its formation and/or breakdown guide clinical decisions, but the test takes anywhere from 30-60 minutes, which is not ideal for emergency medicine. In addition, TEG is primarily tailored towards coagulation rather than shear-mediated platelet plug formation.

Recent research has focused on devices to assess platelet biomechanics in fluidic devices. One device measures the contractile force of individual platelets that have activated and adhered to a pair of fibrinogen microdots [68]. This high-throughput contraction cytometer can differentiate between different platelet subpopulations based on the response to substrate stiffness but also uses thrombin to mimic coagulation. Alternatively, researchers have made collagen microtissues and measured the contraction and stiffening due to shear-activated platelets [69]. The device can measure contractile force dynamically while the overall stiffness is relative to the stiffness of the collagen microtissue at the end of the experiment. Finally, our lab has developed a microfluidic assay that can differentiate between healthy blood and blood inhibited with antiplatelet drugs by measuring the contractile force of shear-mediated plug formation [12]. In this research, I will present this assay as a more clinically translatable tool used to determine bleeding risk and the need for blood transfusion in trauma patients. Afterwards, I modified the assay to investigate the role of mechanotransduction of platelets on the biomechanics of the overall plug during its formation. The microfluidic assay not only uses a low volume of blood and requires a short testing time of 2-5 minutes, but also uses shear instead of agonists to activate the platelets in whole blood, mimicking early hemostasis physiologically and making it favorable for clinicians.

3. A Microfluidic Approach for Anemia Detection in Whole Blood

3.1 Background

Hemoglobin is a protein within red blood cells that is responsible for oxygen transportation. When hemoglobin is either absent, flawed, or impaired, the reduced levels of oxygen in the blood lead to poor tissue oxygenation resulting in dizziness, fatigue, shortness of breath, and abnormal heart rate [9, 10]. Low hemoglobin concentration is diagnosed as anemia, which is caused by more than seventeen different diseases, mainly iron deficiency, hemoglobinopathy, and malaria [3-6]. The World Health Organization recognizes anemia as a global health problem, affecting a quarter of the global population, being highly prevalent in young children and women [9, 10, 35, 70, 71]. Thus, it is important to measure and monitor hemoglobin in these high-risk subpopulations.

For laboratory analysis, hemoglobin concentration is measured with a hematology analyzer as part of a complete blood count (CBC) panel. Hematology analyzers take advantage of the optical absorption of hemoglobin at a wavelength of 540 nm to detect its concentration. Specifically, red blood cells in a sample are lysed to release their hemoglobin. Then, hemoglobin is chemically converted to a stable form, cyanmethemoglobin, for optical detection [26]. From Beer-Lambert law, the light absorbance at 540 nm is proportional to the hemoglobin concentration in a sample [13, 14]. While this method is accurate and reliable, it requires expensive equipment and is used scarcely in resource-poor regions, which coincidently have the highest cases of anemia [9].

To advance the technology beyond its current capabilities, research has shifted focus towards methods for hemoglobin detection that are portable and affordable. These new detection methods still take advantage of the optical absorption of hemoglobin but differ in how they process a blood sample. For example, a portable hemoglobinometer measures light transmission through a chemical-laced cuvette of blood [27]. This approach has been replicated using existing smartphone hardware, in which the built-in camera sensor detects light transmission through a cuvette or microfluidic device [28, 29]. Alternatively, some methods use paper to absorb treated blood prior to performing a colorimetric analysis [30, 31]. Also, a centrifugal microfluidics platform uses rigorous mixing of whole blood and chemicals prior to optical readouts [32]. While these techniques have established a capability to measure hemoglobin, they currently rely on the hemolysis of whole blood.

Hemolysis is favorable for accurate hemoglobin measurements, but it prevents the potential integration with existing or future blood diagnostic platforms. Specifically, there have been separate efforts to diagnose blood diseases in microfluidic assays by measuring the deformability of red blood cells [33, 34]. These measurements allow one to determine the presence of malaria or sickle-cell disease, which can be an underlying cause of anemia [35]. While high-risk subpopulations have been identified from hemoglobin concentration measurements, global health communities acknowledge that the reduction of anemia burden requires more detailed epidemiology which can lead to targeted treatment [35, 36]. Avoiding the process of hemolysis would be a step towards an integrated diagnostic platform for anemia and other blood-related conditions.

Here, we present a method to measure hemoglobin concentration with whole blood in a microfluidic device [37]. Typically, light transmission through lysed blood can determine the hemoglobin concentration solely based on light absorption. Here, because of the use of whole blood, light transmission can still determine the hemoglobin concentration, but it must also account for light scattering. Using this system, we explore the effect of path length and flow rate within a microfluidic device to optimize the detection of hemoglobin for different hematocrit levels. The findings of this study serve as a preliminary step towards a more integrated approach for anemia surveillance.

3.2 Materials and Methods

3.2.1 Blood handling and sample preparation

Blood collection and a complete blood count (CBC) panel were ordered for each human subject under an institutional review board (IRB)-approved protocol from the

University of Washington. All donors were between the ages 18-65, with a weight above 110 pounds, not pregnant, and with no history of blood clotting disorders or blood born infectious diseases. Blood samples were collected in sodium citrate tubes (0.109 M/3.2%, 2.7 mL, BD Vacutainer, Becton, Dickinson, and Company). To adjust the hematocrit levels for analysis, we diluted a portion of a blood sample with calcium-free Tyrode buffer (10 mM HEPES, 138 mM NaCl, 5.5 mM glucose, 12 mM $NaHCO_3$, 0.36 mM Na_2HPO_4, 2.9 mM KCl, 0.4 mM $MgCl_2$ in DI H_2O). Each dilution was loaded into a 3-mL syringe (BD Scientific) and kept on an orbital rocker prior to experiments to prevent any cell sedimentation that would affect the measurements.

3.2.2 Fabrication of microfluidic device

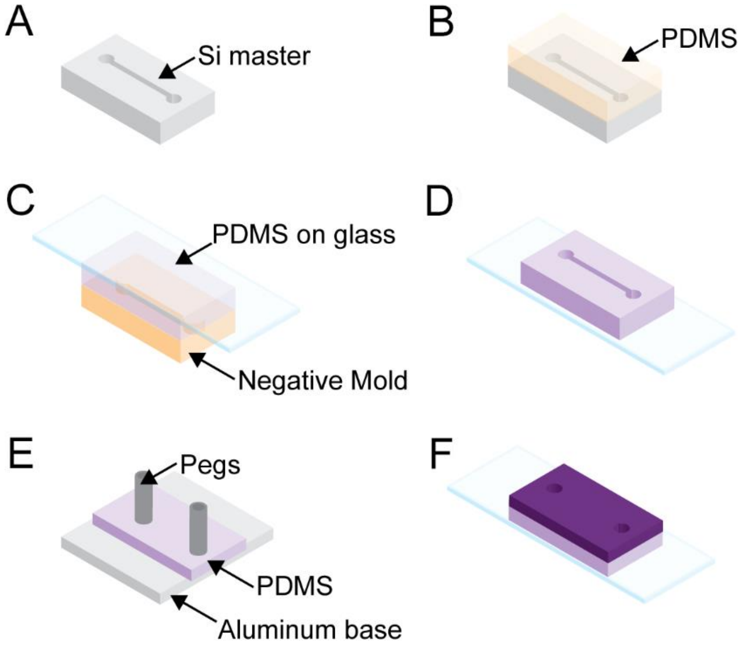

Figure 1. The fabrication of a microfluidic device.

Photolithography of SU-8 photoresist was used to create two silicon master molds for the microfluidic devices with channel heights of 50 and 115 µm, respectively (Figure 1A). Using soft lithography, polydimethylsiloxane (PDMS) (Sylgard 184, Dow Corning) was made with a 10:1 base to curing agent ratio by weight, mixed for 5 minutes, degassed for 20 minutes, and then poured over the master. The PDMS and master were placed in an oven for 10 minutes at 110 °C to form a negative mold (Figure 1B). This negative mold was exposed to plasma (Plasma Prep II, Structure Probe, Inc.)

for 10 seconds. Afterward, the molds were treated with tridecafluoroctyltrichlorosilane (United Chemical Technologies) under vacuum pressure in a desiccator for 2 hours. Uncured PDMS was degassed, poured onto the mold, cast on a microscope slide, and cured at 110 °C for 24 hours (Figure 1C). The mold was peeled away from the glass and PDMS channels remained to form the bottom layer. The top layer for the microchannel was made using a custom aluminum mold with pegs to insert silicone tubing (0.040 inch ID/ 0.085 inch OD, HelixMark) for the inlet and outlet port (Figure 1D). Degassed 10:1 PDMS was poured into the preheated aluminum mold and cured for 110 °C for 1 hour (Figure 1E). The top layer and bottom layer were plasma treated for 10 seconds and then aligned together to create a water-tight seal between the two layers (Figure 1F).

3.2.3 Optical apparatus

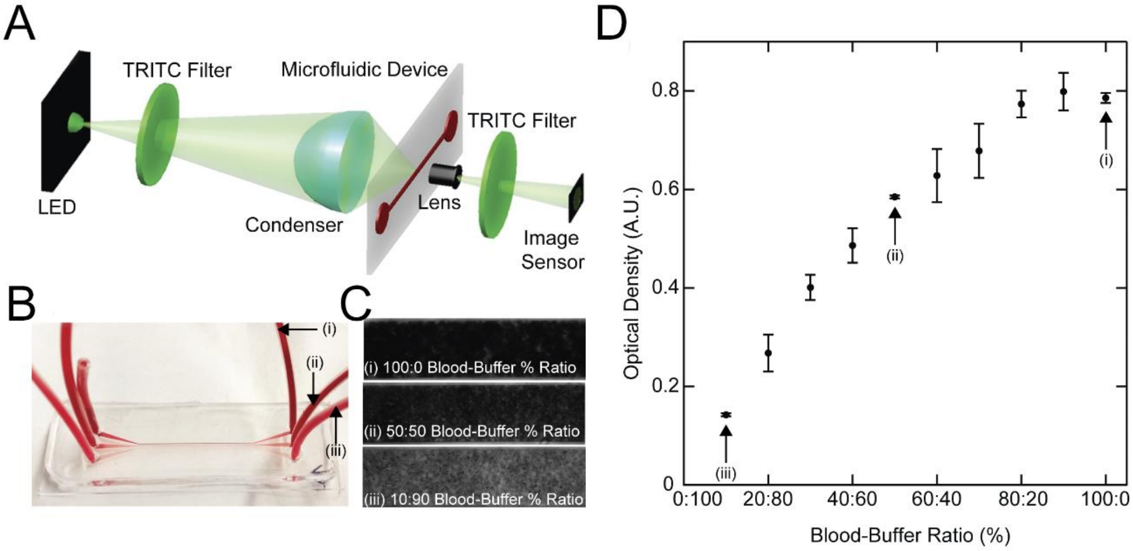

Figure 2. Experimental method to detect optical density in whole blood. (a) A light-emitting diode and TRITC excitation filter (532-552 nm) coupled with an aspheric condenser illuminate a microfluidic channel with green light. This green light goes through a lens and a second TRITC excitation filter and the final image is captured via the image sensor. (b) A microchannel is filled with different percentages of whole blood, (i) 100%, (ii) 50%, (iii) 10%. (c) The microchannel is imaged with and without blood to determine light intensity before and after the blood. (d) Optical density is obtained by measuring the transmission of light before and after blood entered the microchannel. The optical density of a sample was changed by diluting the blood with Tyrode Buffer.

A miniature microscope was constructed to measure the transmitted intensity of light (Figure 2A). The sample was illuminated with a white LED (sr-06-wn300, LuxeonStar) paired with a TRITC excitation filter (mf542-20, Thorlabs), which has a bandwidth of 532-552 nm. The light was focused onto a microfluidic channel with an aspheric condenser (acl2520, Thorlabs). Transmitted light through the microfluidic channel was captured through a board lens (tbl 2.8 5mp, ImagingSource) whose orientation was reversed to magnify the image of the channel. Another TRITC excitation filter was placed in front of the USB powered CMOS camera board (SMN-B050-U, Mightex). A motorized micrometer (Z812B, Thorlabs) was used to adjust the focus to the bottom of the channel for accurate measurements of optical transmission through the full path length. Images were taken at the same exposure time and the LED maintained the same current.

3.2.4 Experimental procedure

For each experiment, whole blood was diluted with Tyrode buffer and gently rocked prior to its injection into a microfluidic channel. Reference images of the channel were taken to measure the initial intensity of light transmission prior to perfusion. After these reference images were taken, blood was injected into the channel (Figure 2B). After blood entered the channel, data images were taken (Figure 2C).

Because of the Beer-Lambert law, we needed to determine the optimal path length for optical density measurements. We compared two different channel heights, 50 and 115 µm. Blood with different hematocrit levels was pipetted into the channel and images were taken. Each hematocrit level was tested at least two times for four subjects. In addition, extra subjects were tested to improve the baseline measurements for the fitted model.

To determine the effect of shear rate on the measurement of optical density of whole blood, a syringe pump (Model PHD Ultra 4400, Harvard Apparatus) regulated flow through the channel with a depth of 50 µm. Images were taken before blood entered the device to record the unobstructed light transmission through the channel.

Then, images were taken as blood flowed at a shear rate of 500 s^{-1}, through the channel. Immediately after the blood came to a halt in the channel, images of the static blood were taken. Hematocrit levels were tested at least two times for four subjects.

3.2.5 *Image analysis*

Ten reference images were taken before blood entered the channel and ten data images were taken after blood entered the channel. Images were imported as a stack in ImageJ. A region of interest within the channel was chosen and the average intensity was measured for each frame. The average value for the corresponding frames represented the intensity before and after blood entered the channel, respectively. These intensity measurements were used to determine optical density.

3.2.6 *Analytical model for light absorbance*

Current methods of hemoglobin detection require the lysis of red blood cells and chemical conversion of hemoglobin into a stable color product. From this procedure, a linear relationship arises between hemoglobin concentration and light absorption at a wavelength of 540 nm, otherwise known as Beer-Lambert's law. However, there is a deviation from this linear relationship if the red blood cells stay intact because their membrane scatters the light. Thus, any method that uses whole blood must account for light scatter to obtain accurate measurements of hemoglobin concentration.

For this study, we used a generalized model from Steinke and Shephard to measure hemoglobin concentration in whole blood [72]. The advantage of this model is the use of optical properties of blood such as the absorption and scattering coefficient (μ_a and μ_s) and fractional hematocrit (H).

Optical density, a unitless quantity, is typically used to describe light transmission through a medium. Optical density (OD) has a logarithmic relationship with the transmittance (T), as described by,

$$OD = -\log_{10} T. \tag{1}$$

The transmittance is represented as

$$T = e^{-\Sigma d}, \tag{2}$$

where *d* is the path length. The characteristic length (Σ) describes the macroscopic change of light flux due to whole blood and is the sum of an absorption and scattering component, represented as

$$\Sigma = \Sigma_a + \Sigma_s. \tag{3}$$

The macroscopic absorption and scattering characteristic lengths, Σ_a and Σ_s, can be defined in terms of the microscopic absorption and scattering cross section area for a single red blood cell. Steinke and Shephard [72] define these relationships as

$$\Sigma_a = \frac{\sigma_a}{V} H \tag{4}$$

$$\Sigma_s = \frac{\sigma_s}{V} H(1 - H)(1.4 - H), \tag{5}$$

where σ_a is the absorption cross section area, σ_s is the scattering cross section area, *V* is the volume of the red blood cell, and *H* is the fractional hematocrit. The coefficient, μ, for either absorption or scattering, is defined as the total cross-sectional area per unit volume. Thus, the final form of characteristic length that describes the change in light flux due to whole blood is

$$\Sigma = \mu_a H + \mu_s H(1 - H)(1.4 - H), \tag{6}$$

where μ_a and μ_s are absorption and scattering coefficients, respectively.

Using equations (1), (2) and (6) and applying a scale factor (*k*), we obtain a final expression given by

$$OD = k(\mu_a H + \mu_s H(1 - H)(1.4 - H))d. \quad (7)$$

Here, the absorption and scattering coefficients are $\mu_a = 0.0743$, and $\mu_s = 0.823$, respectively, based on a previous study that used a wavelength in our range of interest, 532-552 nm [73]. It is also known that these coefficients change relative to the shear rate on the red blood cells [74]. For our optical apparatus, we assumed coefficients related to static conditions and found the data fit well when $k = 0.15457$, which we will present in the Results section. Since hemoglobin and hematocrit have a linear dependence with each other, we can transform this model to predict hemoglobin concentration as well [13]. A Bland-Altman plot can identify the bias and limits of agreement based on the comparison of these model predictions to the actual measurement from the CBC panel.

3.3 Results

3.3.1 A. Simulation of Anemia

Anemia diagnosis is based on a lower level of hematocrit, or by equivalence, a lower level of hemoglobin concentration. To simulate a state of anemia in a blood sample, it was diluted with Tyrode buffer to change its hematocrit levels. As the percentage of blood changed, there was a monotonic change in optical density (Figure 2D). However, the optical density did not increase linearly for blood dilutions higher than 40%. As blood dilution approaches 80%, optical density becomes saturated, making it difficult to associate a hematocrit or hemoglobin measurement with an optical density reading. Thus, the saturation in the optical density at higher levels of hematocrit define the upper limits of our detection.

3.3.2 Variations in Path Length

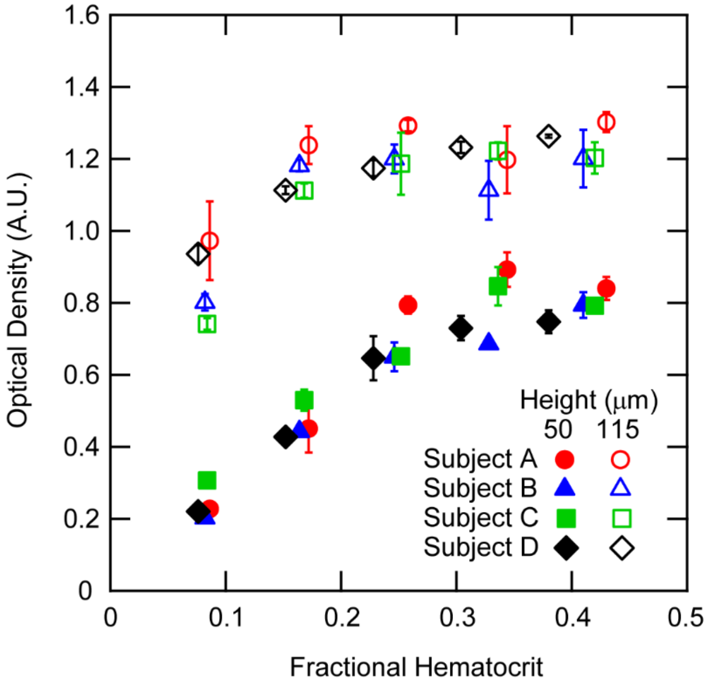

Figure 3. Microchannel height affects the detection approach. Optical density was measured in microfluidic channels with heights 50 µm (filled marker) or 115 µm (empty markers) for five different dilutions of whole blood, which we report by fractional hematocrit levels. It should be noted, the lowest hematocrit level for subject A in the 50 µm channel (red, filled circle marker) was the only data point with one repetition.

Because Beer-Lambert's law indicates a dependence on path length, it was important to test its effect with our optical detection apparatus. The effect of path length on optical density measurements was tested for two different path lengths: 50 and 115 µm. As indicated by the change of hematocrit levels, there was a monotonic change in optical density, which defined a nonlinear relationship (Figure 3). For a path length of 115 µm, changes in optical density diminished above a fractional hematocrit level of 0.15, which indicates there would be difficulty in diagnosing moderate or severe cases of anemia. In contrast, it was possible to detect changes in fractional hematocrit below 0.30 in a microchannel with a path length of 50 µm. This result indicates the optical detection of anemia should be possible for the moderate and severe cases of anemia. From this, we concluded a microfluidic device with the 50 µm channel height provided a better range of detection than the 115 µm channel height.

3.3.3 *Fit to Model and Detection Range*

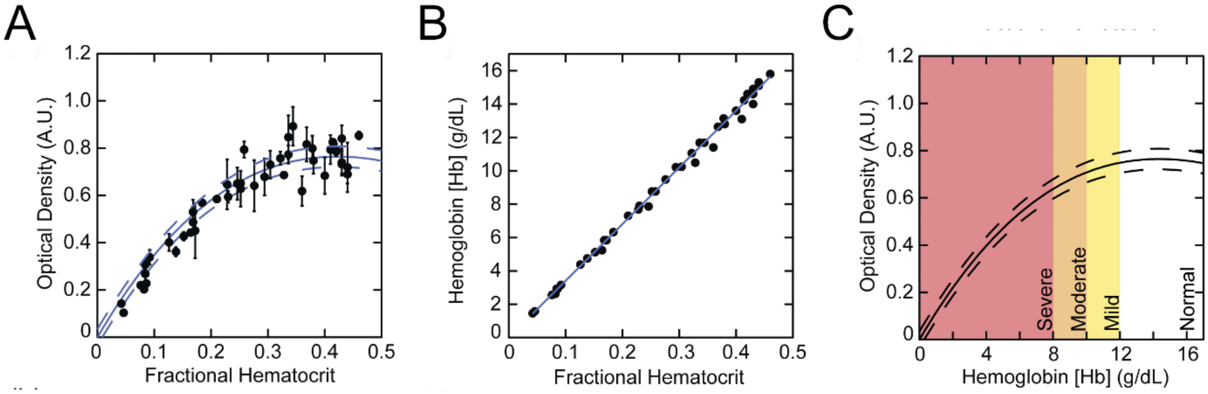

Figure 4. A nonlinear model was fitted to the data. (a) A model (solid line) given by equation 7 that uses the optical properties of the blood, hematocrit level, and path length was fitted to the data. The 95% confidence interval for the model are indicated by dashed lines. (b) A linear relationship between hemoglobin and hematocrit was verified. (c) Afterward, the model was linearly transformed to measure hemoglobin based on optical density measurements. Based on the designation from the World Health Organization, different severity regimes for anemia are designated.

We used the data for the 50 µm channel height to obtain a fit to equation 7 (Figure 4A). For the scaling parameter found, the overall fit had a root mean square error of 0.0135 and a coefficient of determination of 0.847, where the largest variance occurs in the region of higher hematocrit. Because the model originally considers fractional hematocrit, we confirmed that there was a linear relationship between hemoglobin concentration and hematocrit (Figure 4B), which has been reported previously [75]. With this relationship, we could apply the model for hemoglobin concentration to the experimental data (Figure 4C). Based on the width of the 95% confidence interval, estimations can be made about the upper limits of this detection method. Specifically, as the optical density saturates, the width of the 95% confidence bands increase, which indicates that there is less accuracy in the measurement of hemoglobin.

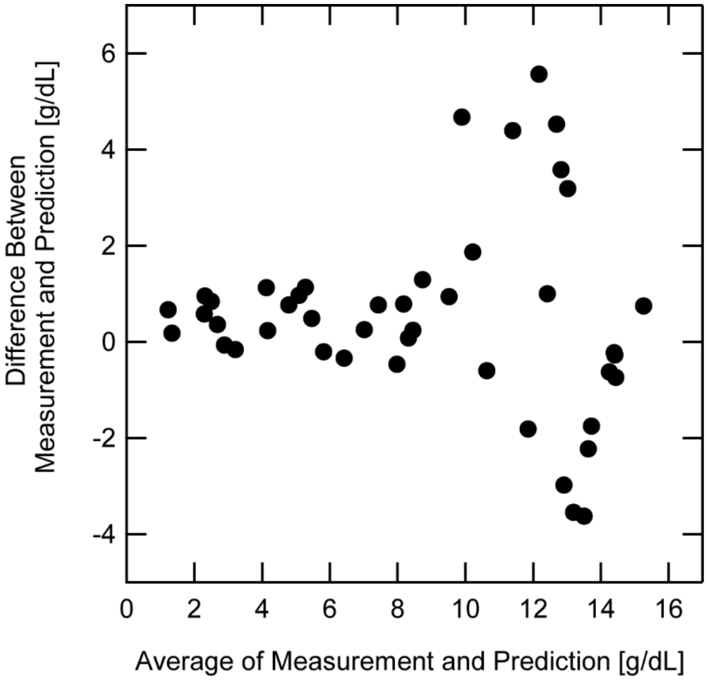

Figure 5. A Bland-Altman plot identifies the limits of agreement for the bias between the actual measurement of hemoglobin and our device prediction to increase from severe anemia to normal ranges of hemoglobin concentration. The nonlinear model was used to predict the hemoglobin level based on the measurements of the optical density. This prediction was compared to the original measurement of hemoglobin acquired from the complete blood count panel.

For a more definitive determination of the range of hemoglobin detection, a Bland-Altman plot was constructed to compare the model prediction to the original measurement from a complete blood count (Figure 5) [76]. The model and optical density measurements were used to determine the predicted hemoglobin concentration. The bias and limits of agreement were found for severe, moderate, and mild anemia, defined by the World Health Organization (Table 1). Based on the Bland-Altman assessment, our technique can determine severe and moderate anemia with higher certainty in whole blood. The limits of agreement for our technique increases to 6.444 g/dL for normal hemoglobin ranges, which indicates this technique is unlikely to give false negative anemia diagnosis.

Table 1. Results of the Bland-Altman assessment for each anemia severity range.

Anemia Severity	Range (g/dL)	Bias (g/dL)	Limits (g/dL)
Severe	0-8	0.425	±1.005
Moderate	8-10	1.336	±3.394
Mild	10-12	0.962	±5.509
Normal	>12	0.023	±6.444

3.3.4 Variations in Flow Rate

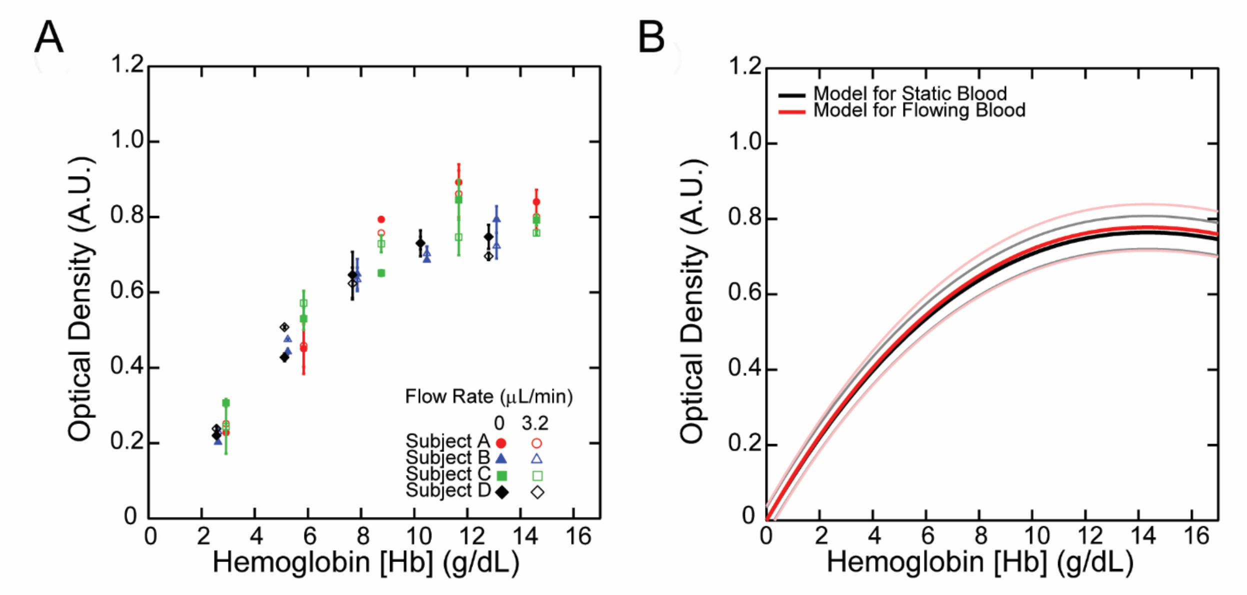

Figure 6. Flow rate did not change the hemoglobin predictions significantly. (a) The optical density for four donors' blood, subject to static and flowing blood are plotted for five different levels of hematocrit. The flow rate of 3.2 µL/min is equivalent to a shear flow of 500 s^{-1} in the 50 µm channel. It should be noted, the lowest hematocrit level for subject A in the static measurement (red, filled circle marker) was the only data point with one repetition. (b) Using the optical density data from the flowing blood measurements, a separate calibration model and its 95% confidence interval was found (red) and compared to the original static calibration model (black).

To test the effect of flow rate, the optical density was measured a shear rate of 500 s^{-1} in the microfluidic channel with a path length of 50 µm in comparison to static flow (Figure 6A). Our motivation to test the effect of shear on the optical density of whole blood was due to a previous study that reported the scattering coefficient of whole blood to be different in static conditions and at shear rates of 200 s^{-1}. As seen in equation 7, a difference in scattering coefficient would affect the measurement of optical density. However, in our technique, a separate model fit was found for the blood under flow and compared to the static flow measurements (Figure 6B). There is a direct overlap between the fit specifically in the anemic regime and this overlap deviates for measurements in the normal hemoglobin region. In addition, the fit line and its confidence band for the flow measurements fall within the confidence band of the static measurements. Thus, the model found in the static conditions can still determine severe and moderate anemia for flowing blood in a microfluidic setting.

3.4 Discussion

Anemia is a global health problem, but new affordable, portable detection methods can provide a means to diagnose the disease in low-resource regions. We developed an approach that uses simple optics and a microfluidic card to measure hemoglobin concentration without the need for hemolysis. We found a path length to measure hemoglobin before the changes in optical density became too small to distinguish between hemoglobin concentration. With this specific path length, our technique was able to determine hemoglobin concentration for hematocrit conditions that mimic severe and moderate anemia in static whole blood. This model also held for flow conditions that have previously demonstrated a shift in the scattering properties of red blood cells.

Path length is known to affect the optical transmission of light, theoretically and experimentally. Therefore, we tested path length in two different microfluidic devices with channel heights of 50 and 115 μm. In general, optical density increased in proportion to hematocrit levels until the measurable change in light transmission became too small to distinguish between hematocrit levels. This saturation effect in the optical density occurs because of the scatter from red blood cells as opposed to light absorption of hemoglobin from hemolyzed blood. As a result, the range of detection only includes the region with a positive slope relationship. A previous study found the initial slope of this detectable region changed with path length, but the range of detection remained the same [77]. However, these studies were done with red or infrared spectra lasers and explored thicker path lengths. In this study, we found a path length of 50 μm was preferable primarily because the positive slope in optical density extended through most of the anemic range before saturation.

The data in this study were fitted to a cubic model, which includes parameters for the optical properties of blood, hematocrit level, and path length. Using our model, we found our predictions for hemoglobin concentration in whole blood had a bias of 0.42 ± 1.01 g/dL for a case of severe anemia. In comparison, a paper-based method could detect hemoglobin from lysed blood for all ranges with a bias of 0.62 ± 1.24 g/dL [31]. Additionally, a microcuvette method with cell phone detection had a bias of 0.036 ± 0.585 g/dL for mild anemia and normal conditions [28]. While our method increases uncertainty towards normal conditions, it is more likely to give a false positive at a higher concentration than a false negative at a lower range.

More importantly, flow rate did not change the predicted model. In previous studies, it was found that an increase in shear rate changed the scattering and absorption properties of whole blood [74]. Specifically, for a shear rate from 0 to 200 s^{-1}, there was a decrease in the scattering coefficient in a 97 and 116 μm cuvette, respectively, which was attributed to the Fahraeus effect. The Fahraeus effect corresponds to a change in hematocrit in flow with respect to tube diameter [78]. However here, we found a shear rate of 500 s^{-1} did not alter the fitted model for static conditions. Therefore, this technique to measure the hemoglobin levels can run parallel to other microfluidic tests that require flowing intact blood cells.

Currently, methods to measure hemoglobin concentration require red blood cell lysis through chemical reactions. Hemolysis eliminates scattering effects from the red blood cell, and this leads to a linear relationship between optical density and hemoglobin concentration, solely dependent on the absorption coefficient. Thus, while lysis is advantageous for absolute measurements of hemoglobin, whole blood eliminates some of the blood handling required and allows for further testing of the same sample in a microfluidic setting. The advantage of microfluidics is to create multiple regions for different testing. As noted by Kassembaum, there are three major reasons for anemia: iron deficiency, hemoglobinopathy, and malaria [35]. The ability to detect not just the concentration of hemoglobin, but also the etiology will help determine the prevalence of anemia and its co-factors in different demographics. Currently, some of these microfluidic devices for malaria detection use red blood cell deformability or electrophoresis, and therefore, require intact whole blood [33, 34, 79]. Thus, a microfluidic device that can detect malaria and severe anemia can provide more detailed information in one test with a single sample. With our proposed method to determine anemia severity, there is potential to combine these measurement capabilities into one diagnostic platform for anemia surveillance.

4. An Optical Approach for Platelet Force Measurements

4.1 Background

To halt bleeding, platelets adhere, activate, and aggregate at a vascular injury site. Specifically, platelets adhere to exposed extracellular matrix such as collagen and surface-bound von Willebrand Factor (VWF). This adhesion leads to internal activation, which causes the platelets to undergo a shape change and release soluble agonists that recruit more platelets to form a platelet-rich plug. During this process, the plug compacts due to the contractile forces of the platelets, helping to stabilize the plug. Platelets play a crucial role in the bleeding response, and dysfunction can occur due to severe trauma or the use of anticoagulants resulting in excessive bleeding. Because of this, platelet function is often the key indicator for bleeding risk.

Cardiovascular disease is the leading cause of death worldwide, for which arterial thrombosis is the primary reason [7]. In arterial thrombosis, there is an uncontrollable growth of a platelet-rich plug. Soluble agonists like thromboxane A2 (TxA_2) promote the growth through platelet activation pathways and therefore, antiplatelet therapies often target this biochemical process. Antiplatelet treatment plans are often assisted by aggregometry, but outcomes have not improved for patients [80].

Our lab developed an assay to measure platelet function microfluidic channels that contain an array of rigid blocks and flexible posts [12]. As whole blood flows though the channel, the block creates a local high shear gradient to trigger platelet adhesion, and a plug forms between the block and post. Platelets generate myosin-based forces and the assay measures the contractility through the deflection of the posts. An expensive fluorescence microscope with a high magnification oil lens is required to track the deflections of these microposts, which is not ideal in a clinical setting. In addition to limited field of view at high resolution, microscopes require training for proper use. Thus, the goal of this aim is to design a compact, inexpensive fluorescence microscopy approach that is capable of tracking the deflections of the microposts for rapid diagnosis of platelet dysfunction.

4.2 Materials and Methods

4.2.1 Blood handling

Blood collection was performed for each human subject under an institutional review board (IRB)-approved protocol from University of Washington. All donors were between the ages 18-65, with a weight above 110 pounds, not pregnant, and with no history of blood clotting disorders or blood born infectious diseases. Blood samples were collected in sodium citrate tubes (0.109 M/3.2%, 2.7 mL, BD Vacutainer, Becton, Dickinson, and Company). Tubes were labeled with draw order and the first drawn tube was discarded to prevent puncture contamination. Blood was pooled into one 50-mL tube and kept on an orbital rocker prior to experiments to prevent cell sedimentation.

4.2.2 Fabrication of microfluidic device

Photolithography of SU-8 photoresist was used to create a silicon master mold for the microfluidic device with the block and post sensors. The blocks were 25 μm × 25 μm × 15 μm and posts that were 6 μm in diameter and 25 μm in height. Using soft lithography, polydimethylsiloxane (PDMS) (Sylgard 184, Dow Corning) was prepared with a 10:1 base to curing agent ratio, mixed for 5 minutes, degassed for 20 minutes, and then poured over the SU-8 master. The PDMS and master were placed in an oven for 10 minutes at 110 °C, allowing the PDMS to cure and form a negative mold. This negative mold was removed from the master and exposed to plasma (Plasma Prep II, Structure Probe, Inc.) for 10 seconds. Immediately afterwards, the molds were treated with tridecafluoroctyltrichlorosilane (United Chemical Technologies) under vacuum pressure in a desiccator for 2 hours. Uncured PDMS was degassed, poured onto the mold, cast on a microscope slide, and cured at 110 °C for 24 hours. The mold was peeled away from the glass and PDMS channels with black and posts remained to form the bottom layer. The top layer for the microchannel was made using a custom aluminum mold with pegs to insert the silicone tubing (0.040-inch ID/ 0.085-inch OD, HelixMark) for the inlet and outlet port. Degassed 10:1 PDMS was poured into the preheated aluminum mold and cured for 110 °C for 1 hour. The top layer and bottom layer were plasma treated for 10 seconds and then aligned together to create a water-tight seal between the two layers.

4.2.3 Functionalization of Device

The microfluidic channels were fluorescently stained with 1,1'-dioleyl-3,3,3',3'-tetramethylindocarbocyanine methanesulfonate (DiI, Life Technologies) at 5 μg/mL for two hours. The channels were than rinsed with Tyrode’s buffer (10 mM HEPES, 138 mM NaCl, 5.5 mM glucose, 12 mM NaHCO3, 0.36 mM Na2HPO4, 2.9 mM KCl, 0.4 mM MgCl2). Afterwards, rat tail collagen type I (200 ug/mL, BD Bioscience) in 0.1 M acetic acid was incubated in the microchannels for one hour at room temperature. Finally, the channel was rinsed with Tyrode’s buffer to remove excess collagen and stored in fresh buffer prior to the experiments.

4.2.4 Inhibitors

Acetylsalicylic acid (0.5 mM in DMSO) was incubated with the blood for 20 minutes prior to testing. For all controls, an equal volume of DMSO was instead added to the blood.

4.2.5 Optical Detection Solution and Design Process

The goal of this aim is to remove the necessity of a fluoresence microscope and replace it with a compact, simple benchtop system that is able to optically track the centroid of the micropost at high resolution and throughput. To solve this problem, I reversed the configuration of a webcam lens (Figure 7A). Typically, a webcam lens contains optics that shrink an image of our face down to the size of a CMOS sensor. By flipping the lens, it should theoretically magnify a small object. The distance between the lens and the CMOS sensor controls the amount of magnification and the focal length of the object. Additionally, as the distance between the lens and the CMOS sensor increases, the intensity of light reduces, so some optimization is required.

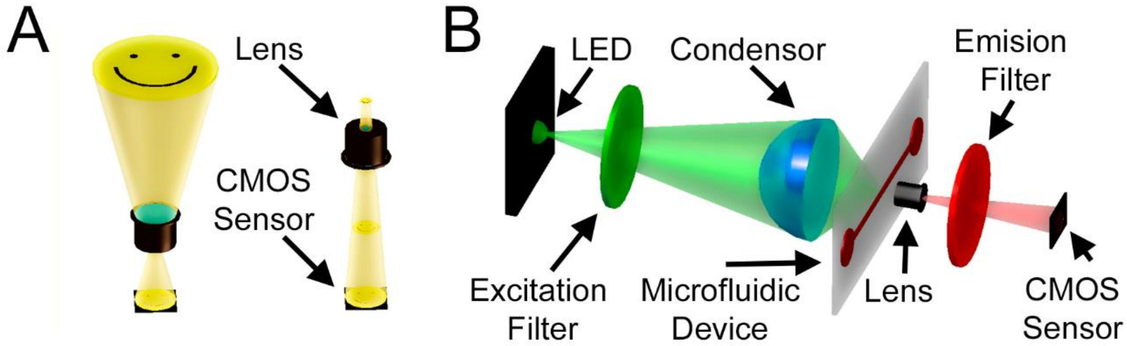

Figure 7. Conceptual Illustrations of the Optics. (A) A webcam lens in reversed configuration will magnify a small object. (B) The optics solution for magnifying fluorescence objects is to include the excitation/emission filters as well as a condenser to focus the light from an LED source at the microfluidic device.

In a fluorescence microscope, fluorescence images obtained by placing a filter cube in the light path. An excitation filter allows light of a particular wavelength to hit the sample, causingthe fluorophores for that particular wavelegnth to emit lower energy light. To capture only this emitted light, an emission filter is placed prior to the light entering the camera or eyepiece. Using this concept, the optical configuration of the benchtop design involved an LED light source paired with an excitation filter and a condensor to focus the light with a higher intensity at the area of interest (Figure 7B). After the light excites the fluorscent stain used to visualize the posts, a reversed webcam lens magnifies the image, filters only the emitted light via an emission filter, and is recorded onto a CMOS camera sensor.

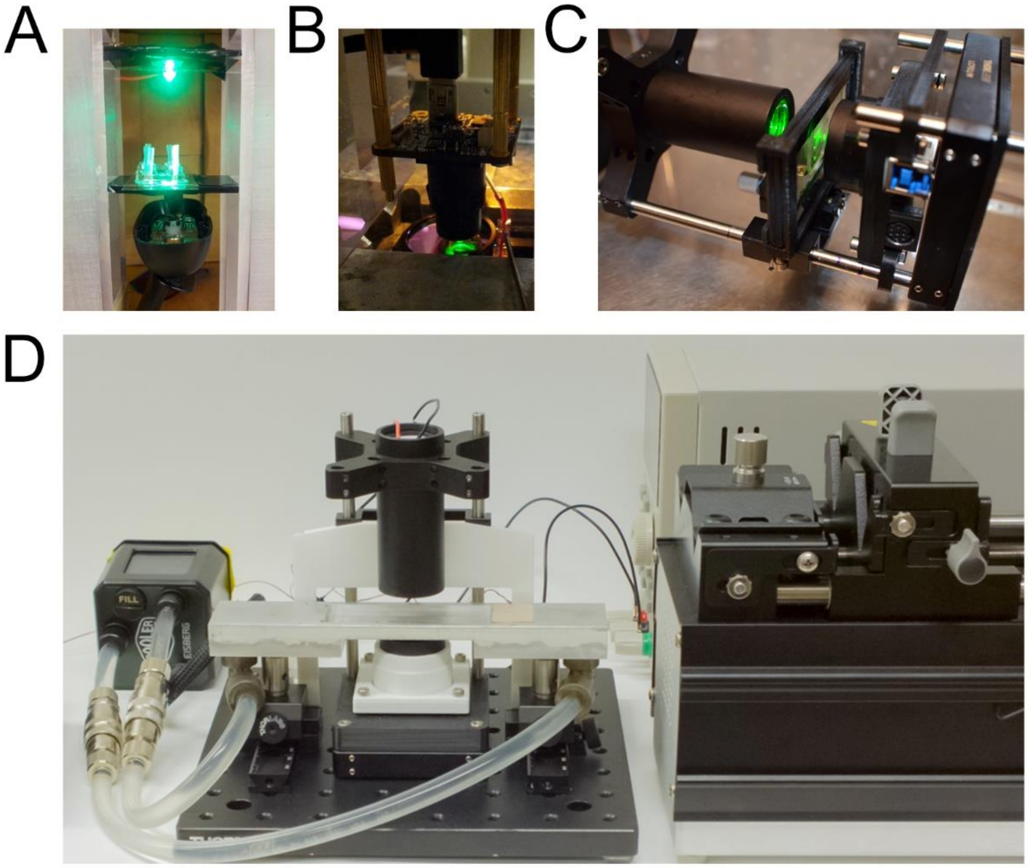

Figure 8. Prototype Designs for Optical Detection. (A) Initial proof of concept for magnification. (B) Prototype to test if CMOS sensor is sensitive enough to detect forces. (C) Prototype to test if excitation optics are as good as the microscope. (D) Prototype to conduct preliminary blood experiments included a metal holder to heat the card.

Several design iterations took place to verify each component involved for the transmission optics. The initial proof of concept for the reverse lense magnification involved the desconstruction of a simple Logitech 510 webcam system. The lens was taken out and placed in a reversed configuration at different distances above the built-in CMOS sensor. A custom acrylic rig was designed to hold the sample at the necessary focal length along with an LED above to illuminate the sample (Figure 8A). Initial experiments did not use the LED and instead relied on the lighting from the microscope using a 20x objective (Figure 8B). The light passed through the microfluidic device and encountered a filter prior to entering the built-in reversed lens (tbl 2.8 5mp, ImagingSource) and CMOS sensor board (DMM 72BUC02-ML, ImagingSource). The illumination of the samples was then switched to an LED system encclosed in a cylindrical tube that also housed a filter and condensor to focus the light (Figure 8C). The system was flipped 90 degrees and a heated chamber was constructed to keep the testing of blood within the microfluidic device at 37 degrees (Figure 8D).

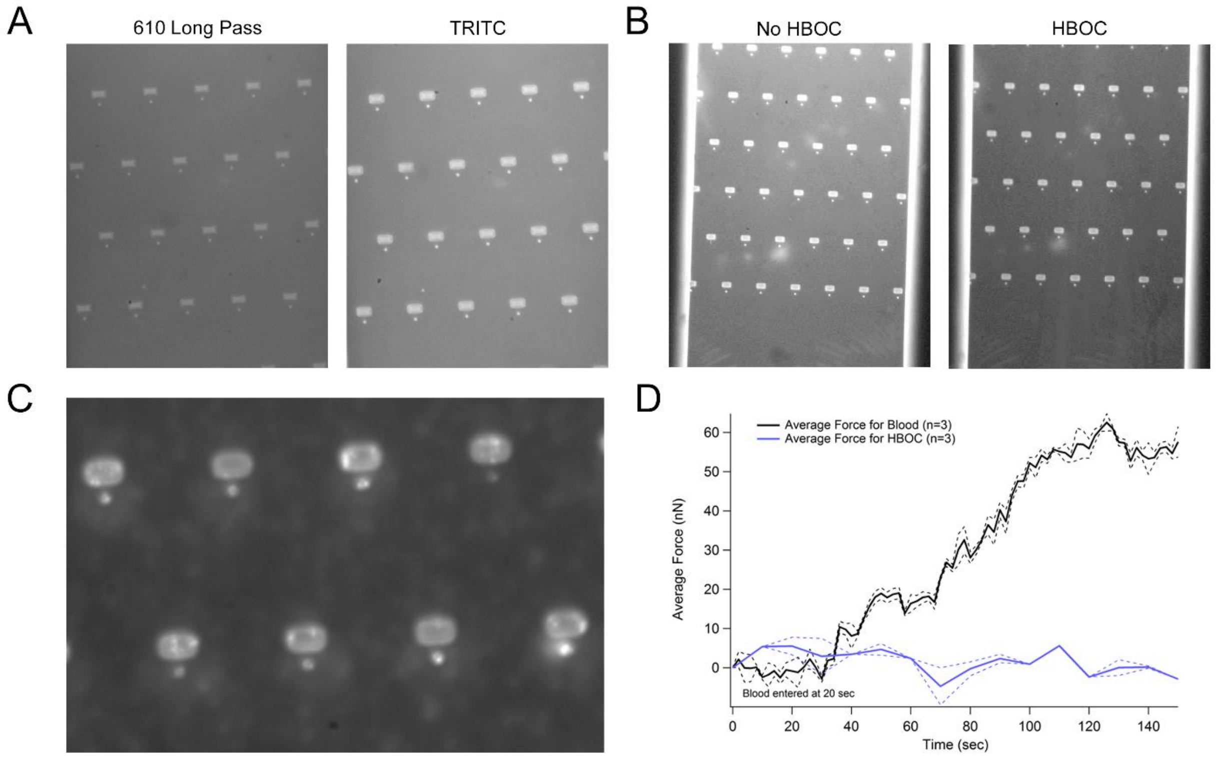

Figure 9. The first blood experiment using an early version of the optical benchtop system. (A) The initial decision to rely on TRITC filters for the illumination of DiI was due to the fluorescence signal. (B) Artificial blood was flowed into the channel to ensure there was no disruption to the fluorescence signal. (C) The platelet-rich plugs formed between the block and post. (D) The camera optics detected forces in comparison to the baseline reading from the artificial blood.

To test the initial capabilities the optics and choose proper filters, the first blood experiment was conducted using an inverted camera system and illumination from the microscope (Figure 8B). A custom microfluidic device was constructed such that the block and post arrays were inverted and could be viewed from below. A TRITC filter (Thorlabs) was more effective than a 610 Long Pass filter to visualize the fluorsence stain of the posts (Figure 9A). In the presence of artifical blood (HBOC), the background signal reduced, further improving the illumination of the posts (Figure 9B). Images were taken every two seconds as whole blood flowed through the channel to form platelet rich plugs between the block and post (Figure 9C). The distance between the block and post was tracked and the contractile force of platelets was determined in comparison to an artifical blood sample (Figure 9D). This experiment verified that a reversed lens with this specific camera board could track platelet forces, and further designs improved upon this proof-of-concept.

A final optical benchtop system was designed and manufactured to act as a miniature microscope that takes images of the microscale deflections of the posts (Figure 10). The sample was placed in a heated chamber and illuminated with a white LED (sr-06-wn300, LuxeonStar) paired with a TRITC excitation filter (mf542-20, Thorlabs), which has a bandwidth of 532-552 nm. The light was focused onto a microfluidic channel with an aspheric condenser (acl2520, Thorlabs). Transmitted light through the microfluidic channel was captured through a board lens (tbl 2.8 5mp, ImagingSource) whose orientation was reversed to magnify the image of the channel. A TRITC emission filter (mf620-52, Thorlabs), which has the bandwidth of 594-646 nm, was placed in front of the USB-powered CMOS camera board (SMN-B050-U, Mightex). The distance between the board lens and CMOS camera sensor was optimized to capture microscale forces at a high resolution while also maintaining a large field of view. A motorized micrometer (Z812B, Thorlabs) was used to adjust the focus of the lens to the top of the microposts for accurate measurements of platelet forces. The camera sensor was set to capture an image every 2 seconds, and the syringe pump, heater, and image capture were all controlled through a custom code in MATLAB.

4.2.6 Microfluidic Testing Protocol

Blood was drawn into a disposable syringe (BD Scientific) and placed into a syringe pump (Harvard Apparatus) to control the flow rate through the microfluidic device. The flow rate was set to 16,000 s^{-1} for 15 seconds (usually 30-60s in this version) to rapidly form platelet aggregates and then reduced to 500 s^{-1} to reduce the attachment of additional platelets.

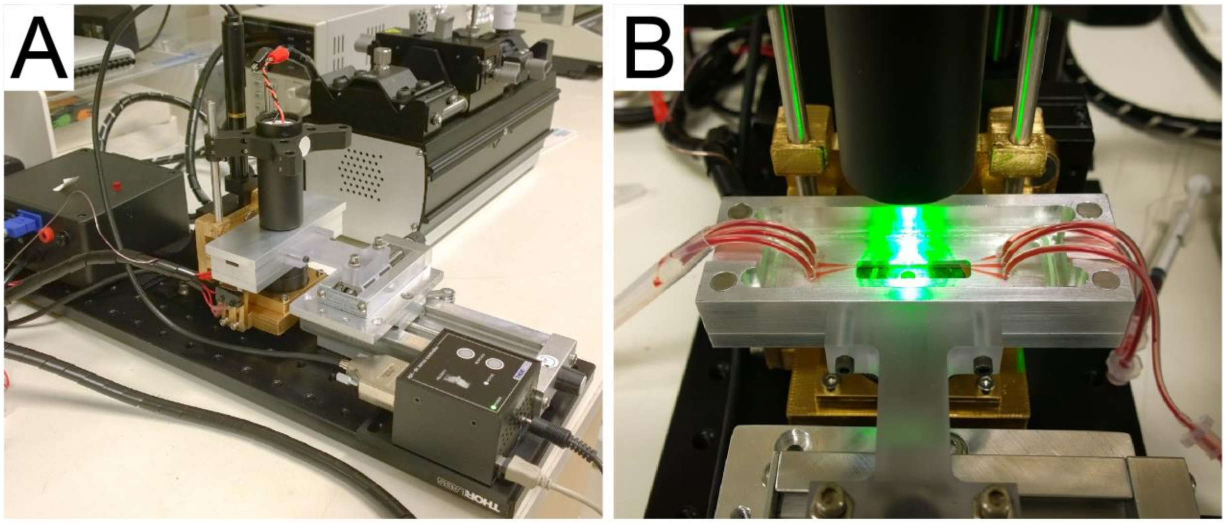

Figure 10. A miniature microscope to visualize platelet forces.

4.2.7 Image Analysis

Euler-Bernoulli beam theory is used to calculate the force (F) produced by a platelet-rich plug, given by

$$F = \left(\frac{3\pi E D^4}{64 H^3}\right)\delta. \tag{8}$$

Here, D is for diameter (6 μm), H is for height (25 μm), E is for the elastic modulus of PDMS (3.8 MPa), and δ is the deflection of the post. Therefore, to measure the platelet forces, the deflection of the posts must be measured over time. A custom-written MATLAB code analyzed each image and identified the centroid of each block and post pair. The centroids were used to calculate the displacement of the tip of the post, and platelet plug force was calculated using equation 8.

4.2.8 Statistical Analysis

For the line plots, the mean and 95% confidence interval are represented. A one-way analysis of variance (ANOVA) with Tukey's post-hoc test was used to compare the trauma groups at 120 seconds of assay time.

4.2.9 Trauma Study

Human subjects were enrolled into a cross-sectional observational study at a Level I Trauma center: Harborview Medical Center Emergency Department. Delayed consent from all study subjects was obtained to participate in the study based on an approved IRB protocol. Written consent was obtained afterwards from either each subject or an approved representative. Subject enrollment was for adults (≥18 years), not pregnant or incarcerated, presented directly from the place of injury, and had no more than three units of transfused blood products prior to a blood draw. Subjects were compared to ten additional healthy subjects, also enrolled by consent.

4.3 Results

4.3.1 Optical Characterization

There were two major goals in the optical design for a miniature fluorescence microscope. The first goal was to maintain a resolution to allow for microscale force detection. The second goal was to gain a bigger field of view to track the deflections of several force sensors. Using a 1951 USAF Resolution Target test, the resolving power of the webcam lens was determined to be between a 20x and 40x objective. It could resolve the smallest lines on the target that denote 2.2 μm (Figure 11A).

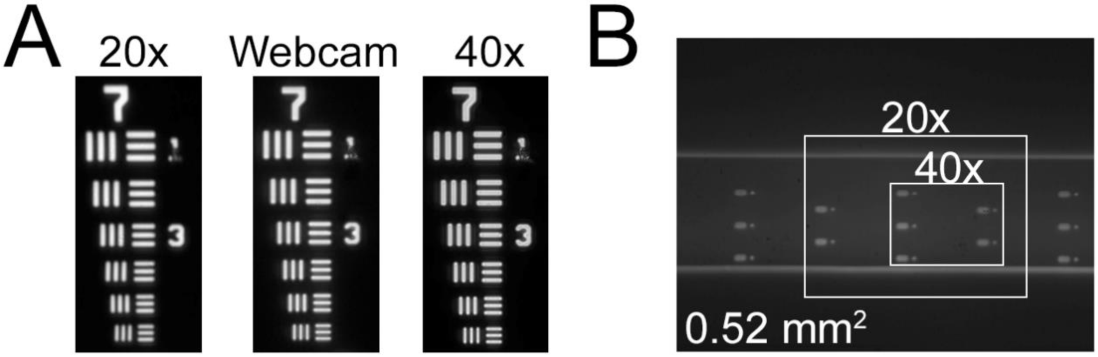

Figure 11. Optical characterization of optical solution. (A) A 1951 USAF resolution target test revealed the resolving power of the webcam lens is between a 20 and 40x microscope objective. (B) The field of view is between a 5-10x objective. In comparison, a 20x and 40x view from a microscope objective is denoted by the box.

The field of view is directly based on the CMOS sensor and the magnification. At the current distance between the lens and the CMOS image sensor, the field of view is approximately 0.778 mm by 0.584 mm and has a sensor resolution of 0.3 μm/pixel (Figure 11B). In comparison, a 40× oil objective produced a field of view 0.223 mm × 0.166 mm with a sensor resolution of 0.16 μm/pixel. Therefore, the benchtop system achieved a resolution better than a 20x objective with the field of view better than a 10x objective. While there is a loss in sensor resolution as compared to the 40x objective, the webcam method can track more microposts in a less expensive and more compact system.

4.3.2 Benchtop System vs Inverted Microscope

To compare the benchtop optical system against an inverted microscope equipped with a 20x objective, blood was drawn by an on-site phlebotomist from five donors and contractile force was measured. Blood was tested within five minutes of it being drawn from each donor. By plotting the mean and 95% confidence interval, the results indicated that the data acquired from the benchtop system was nearly identical to the inverted microscope (Figure 12).

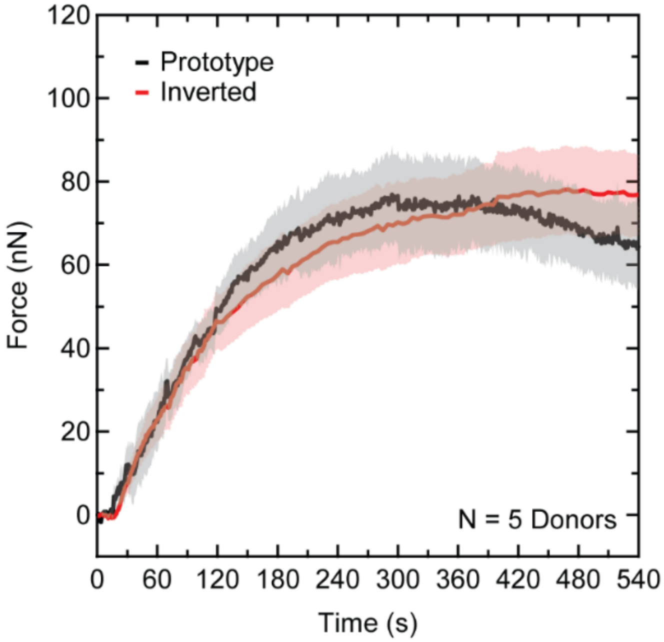

Figure 12. The force from the platelet force assay was measured using the prototype and inverted microscope. The standard error of the mean is represented by the shaded region. The force curves indicate that the measurements and the error are similar.

4.3.3 Inhibited Blood

The purpose of the benchtop system is to detect platelet dysfunction in a clinical setting. While we have shown that the benchtop system can detect forces from healthy platelets, dysfunctional platelets tend to exhibit low force production. To test if the benchtop system can detect low forces, blood was inhibited with 0.5 mM acetylsalicylic acid (ASA), which is equivalent to two extra strength tablets of aspirin. ASA targets the generation of thromboxane, a soluble agonist response in platelet recruitment and aggregation. First, a study was conducted with an inverted microscope in which ASA attenuated the force generation of platelet-rich plugs (Figure 13A). Then, the experiment was repeated using the optical benchtop system (Figure 13B) and similar results were found, indicating the benchtop system is capable of differentiating between healthy and impaired platelets.

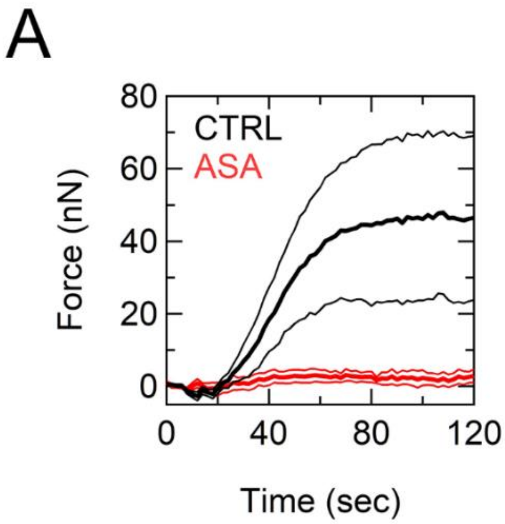

Figure 13. Blood was inhibited with 0.5 mM ASA. (A) Five donors were tested using an inverted microscope. (B) As an example, blood drawn on-site was inhibited and tested using the optical detection method.

4.3.4 Emergency Department Trauma Patients

To evaluate if this system had clinical value, a prospective cross-section observational study of Emergency Department trauma patients was conducted. Blood was taken from subjects when they arrived at the Emergency Department. The subject pool included 10 healthy control subjects and 93 trauma patients, of which 18% required blood product transfusions within the first 24 hours of hospital care. These patients received a transfusion of an average (SD) of 3.3 (4.4) packed red blood cell units (79% within the first 4 hours), 1.3 (1.5) platelet units (63% within 4 hours), and 2.8 (4.9) plasma units (85% within 4 hours). The rest of the trauma patients as well as the healthy controls did not receive blood transfusions.

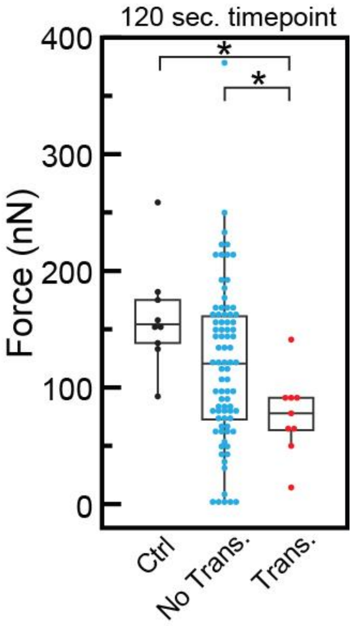

Figure 14. The force was measured for healthy control, non-transfused trauma patients and patients that received a transfused within 24 hours. A significant reduction of force was observed between the transfused group and the healthy control and non-transfused group.

The platelet forces at the 120 second mark were compared for the healthy control, transfused trauma, and non-transfused trauma groups (Figure 14). A summary of clinical data between the transfused and non-transfused trauma groups can be found in Table 2. There were statistical differences detected between the platelet forces for the transfused, non-transfused, and control group (one-way ANOVA F = 4.4, DF = 2, p = 0.015). Specifically, the platelet forces in the trauma group were decreased in comparison to the healthy controls (Tukey p=0.017) and the non-transfused trauma group (Tukey p=0.044). Thus, the optical benchtop system was able to detect bleeding risk and determine the need for blood transfusion.

Table 2. Summary of demographic and clinical data for non-transfused and transfused trauma group during the observational trial.

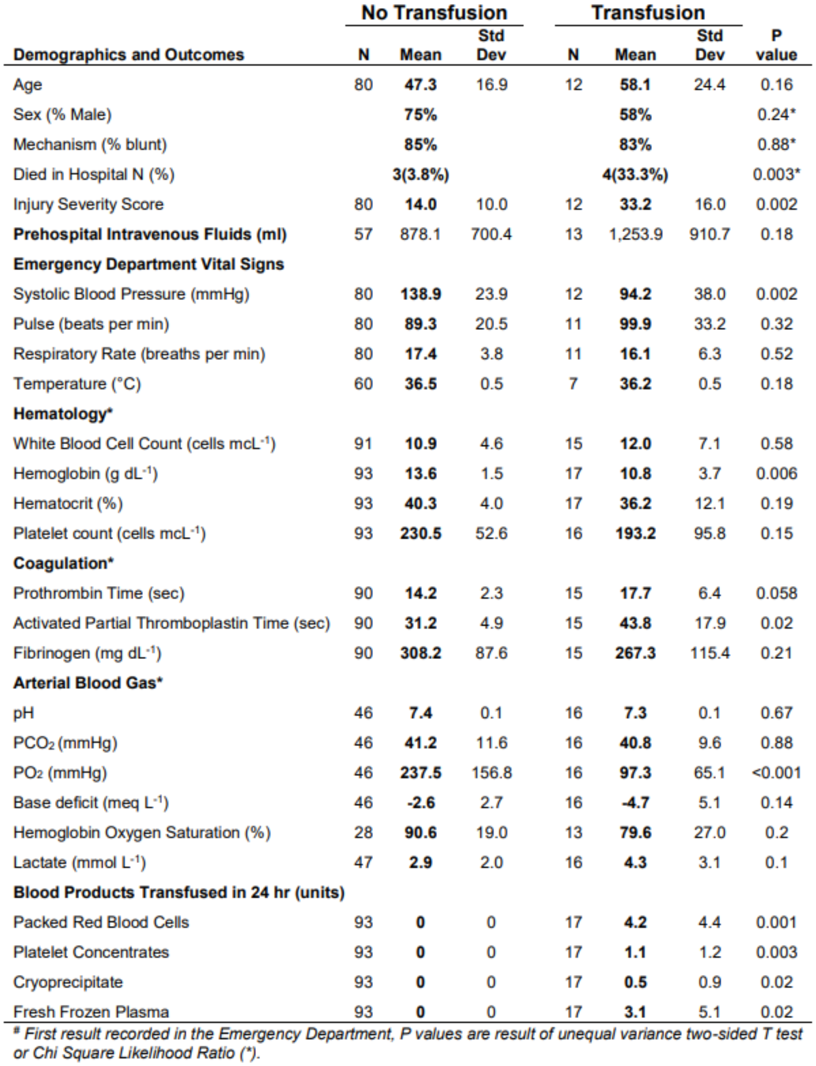

	No Transfusion			**Transfusion**			
Demographics and Outcomes	**N**	**Mean**	**Std Dev**	**N**	**Mean**	**Std Dev**	**P value**
Age	80	**47.3**	16.9	12	**58.1**	24.4	0.16
Sex (% Male)		**75%**			**58%**		0.24*
Mechanism (% blunt)		**85%**			**83%**		0.88*
Died in Hospital N (%)		**3(3.8%)**			**4(33.3%)**		0.003*
Injury Severity Score	80	**14.0**	10.0	12	**33.2**	16.0	0.002
Prehospital Intravenous Fluids (ml)	57	878.1	700.4	13	1,253.9	910.7	0.18
Emergency Department Vital Signs							
Systolic Blood Pressure (mmHg)	80	**138.9**	23.9	12	**94.2**	38.0	0.002
Pulse (beats per min)	80	**89.3**	20.5	11	**99.9**	33.2	0.32
Respiratory Rate (breaths per min)	80	**17.4**	3.8	11	**16.1**	6.3	0.52
Temperature (°C)	60	**36.5**	0.5	7	**36.2**	0.5	0.18
Hematology#							
White Blood Cell Count (cells mcL^{-1})	91	**10.9**	4.6	15	**12.0**	7.1	0.58
Hemoglobin (g dL^{-1})	93	**13.6**	1.5	17	**10.8**	3.7	0.006
Hematocrit (%)	93	**40.3**	4.0	17	**36.2**	12.1	0.19
Platelet count (cells mcL^{-1})	93	**230.5**	52.6	16	**193.2**	95.8	0.15
Coagulation#							
Prothrombin Time (sec)	90	**14.2**	2.3	15	**17.7**	6.4	0.058
Activated Partial Thromboplastin Time (sec)	90	**31.2**	4.9	15	**43.8**	17.9	0.02
Fibrinogen (mg dL^{-1})	90	**308.2**	87.6	15	**267.3**	115.4	0.21
Arterial Blood Gas#							
pH	46	**7.4**	0.1	16	**7.3**	0.1	0.67
PCO_2 (mmHg)	46	**41.2**	11.6	16	**40.8**	9.6	0.88
PO_2 (mmHg)	46	**237.5**	156.8	16	**97.3**	65.1	<0.001
Base deficit (meq L^{-1})	46	**-2.6**	2.7	16	**-4.7**	5.1	0.14
Hemoglobin Oxygen Saturation (%)	28	**90.6**	19.0	13	**79.6**	27.0	0.2
Lactate (mmol L^{-1})	47	**2.9**	2.0	16	**4.3**	3.1	0.1
Blood Products Transfused in 24 hr (units)							
Packed Red Blood Cells	93	**0**	0	17	**4.2**	4.4	0.001
Platelet Concentrates	93	**0**	0	17	**1.1**	1.2	0.003
Cryoprecipitate	93	**0**	0	17	**0.5**	0.9	0.02
Fresh Frozen Plasma	93	**0**	0	17	**3.1**	5.1	0.02

 # First result recorded in the Emergency Department, P values are result of unequal variance two-sided T test or Chi Square Likelihood Ratio (*).

4.4 Discussion

Our lab developed a rapid, microfluidic approach to measure contractile forces of platelets. Myosin-based force generation requires both the surface receptors and activation pathways for platelets. Therefore, to make this assay more clinically translatable, we built a benchtop optical system with a detection sensitivity capable of microscale deflection measurements, and a greater field of view than a conventional microscope. I was able to discern the reduction of force in our platelet force assay associated with ASA (aspirin). Therefore, this system may be able to guide antiplatelet therapies and improve clinical outcomes, but further studies are required.

Platelets improve the strength and stiffness of a clot during hemostasis, as well as prevent breakdown. During trauma, platelet dysfunction leads to impaired aggregation and clot weakening. In an emergency department setting, platelet function is often assessed because it is a key indicator for mortality and platelet transfusions manage traumatic bleeding. Currently, clinical settings rely on a number of tests to assess platelet function. For instance, platelet count is often used despite remaining in a normal range even in trauma. Viscoelastic tests of clot formation like thromboelastography (TEG) are often used to assess transfusion needs for trauma patients but these tests are unable to detect platelet dysfunction. The platelet force assay developed here is able to rapidly detect bleeding risk and determine the need for blood transfusion products. The optical solution allows for a more clinically translatable device and it is a promising avenue for platelet function assessment in a trauma setting.

5. Magnetic Actuation on the Microscale

5.1 Background

With the rise of microdevices, scientists have looked towards magnetism to add an extra layer of complexity in investigating biological questions and providing new diagnostic avenues. For example, nickel nanowires have been embedded into PDMS microposts to apply forces to cells [81], nickel shells have been attached to PDMS posts to measure whole blood clot stiffness [82], and on an even larger scale, carbonyl iron microparticles have been added to larger posts to measure the viscoelastic properties of collagen [21]. To control the magnetic material within their microstructures, these methods primarily depend on electromagnetic coils or bar magnets for actuation. Thus, the goal of this chapter is to integrate microscale magnetic actuators into the platelet force assay described in Aim 2.

5.1.1 Magnetic Materials and Their Properties

Magnetic fields manifest due to a current, or an electric charge in motion. On the atomic scale, current forms due to the electrons orbiting a nucleus and the spin about their own axis. As a result, each atom forms a magnetic dipole moment **m** perpendicular to the current loop **I** and its direction is dependent on the direction of the current loop due to the right-hand rule (Figure 15A). Each magnetic dipole produces a magnetic field in a manner similar to a macroscopic bar magnet (Figure 15B). Typically, the orientation of these dipoles is random within a material such that the net dipole moment and therefore its magnetic field, is zero. However, depending on the magnetic properties of a material, an external magnetic field will reorient these dipoles in a specific way.

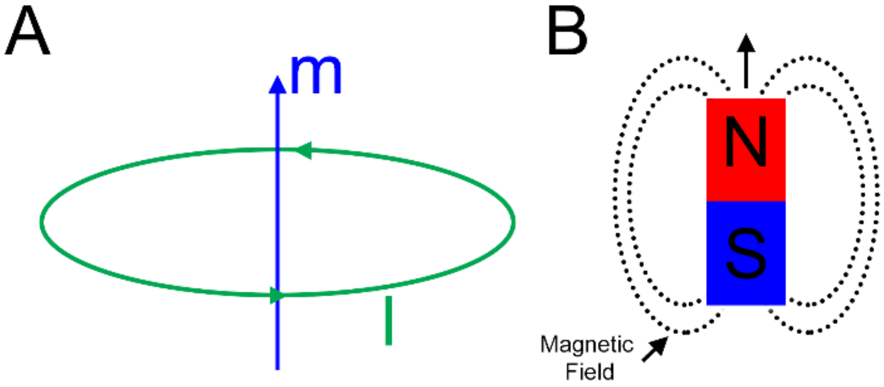

Figure 15. (A) Current loops give rise to magnetic dipole moments. (B) The magnetic dipole moment is like an infinitesimally small bar magnet that emits a magnetic field from the north end to the south end.

Magnetic materials can be defined based on the behavior of their magnetic moments and their susceptibility to magnetic fields. The response of a material to a magnetic field is designated into three categories: diamagnetism, paramagnetism, and ferromagnetism (Figure 16). Diamagnetic materials form magnetic dipoles in the opposite direction of an external field. As a result, these materials have a weak repulsion to the field. Without an external field, diamagnetic materials do not retain randomly oriented dipole moments. Paramagnetic materials already have magnetic dipole moments that are randomly oriented such that the net field is zero. In contrast to a diamagnetic material, these dipole moments will align such that the “north” orients with the field. However, if the external field is removed, the magnetic dipoles in the material become randomly oriented again. Ferromagnetic materials have domains that contain completely aligned permanent dipole moments. The domains are distributed uniformly throughout a material such that there may not be a net magnetic field. However, an external field will force these domains to align in the direction of the field and many of these domains will keep this new alignment when the field is removed. As a result, ferromagnetic materials become permanent magnets that can independently produce a magnetic field.

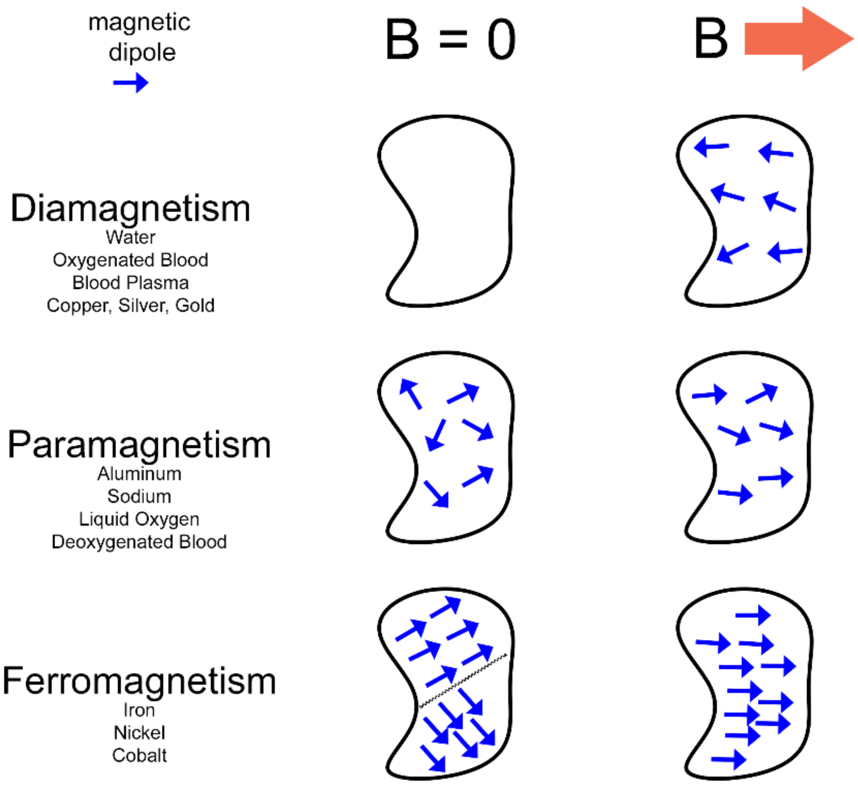

Figure 16. Magnetic materials are generally categorized in three categories based on their behavior with and without the magnetic field.

The degree of magnetic dipole alignment or the net magnetic dipole moments per unit volume is known as magnetization **M**. Magnetization is dependent on the temperature and magnetic field strength. Cooler temperatures reduce the thermal fluctuations of atoms, which makes magnetic materials more susceptible to magnetization. Hotter temperatures increase fluctuations and the random orientations of atoms leads to a loss of magnetization. At a specific temperature, known as the Curie point, a material will completely demagnetize, shifting ferromagnetic materials into a paramagnetic state.

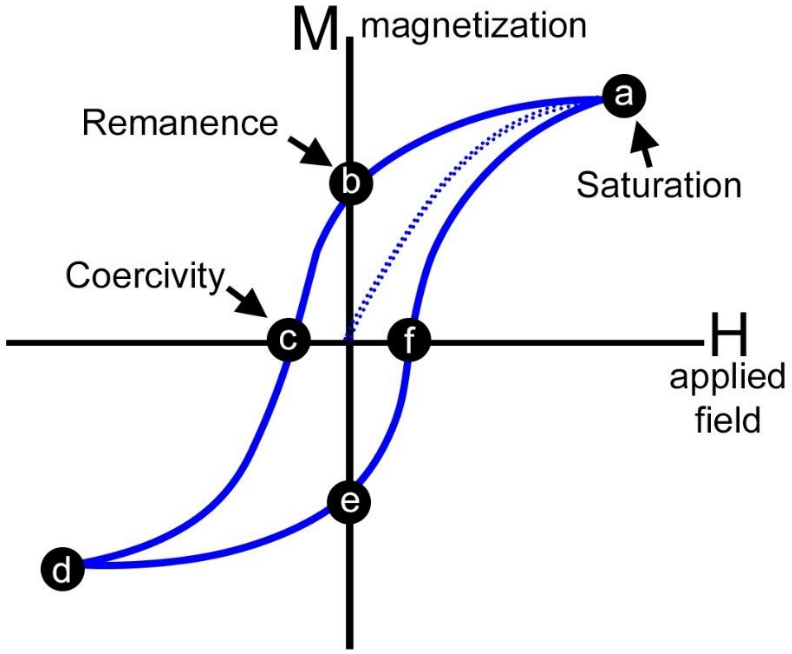

Figure 17. Ferromagnetic materials form a hysteresis curve in the presence of a magnetic field. Depending on the applied magnetic field and the material's history, the behavior of the material will vary based on this curve.

A ferromagnetic material adopts a hysteresis curve once it is exposed to a magnetic field (Figure 17). When exposed to a high magnetic field strength, the material eventually reaches a point (Figure 17a) known as saturation, in which all the dipoles are aligned in the direction of the field. If the field is removed, the material retains a certain amount of magnetization inside the material and this point (Figure 17b) is known as remanence $\mathbf{M_r}$. When the field is reversed and strong enough, eventually the material loses its magnetization at a point (Figure 17c) known as the coercive field $\mathbf{H_c}$. The material reaches saturation in the opposite direction with the continued application of this external field (Figure 17d). However, if this field is turned off, it retains a negative remanant magnetization because all the domains were previously aligned in the opposite direction (Figure 17e). By applying the external field in the original direction, the material eventually demagnetizes (Figure 17f) and reaches a positive saturation point again.

As a hysteresis curve becomes narrower (when points c and f are close together), it takes a smaller amount of energy to reverse the magnetization of the material. In Table 2, the remanant magnetization and coercive field are defined for the most common ferromagnetic materials: nickel, cobalt, and iron. It indicates that iron and nickel take less amount of energy to reverse the magnetization in comparison to cobalt, but iron retains more magnetization than nickel in the presence of no field.

Table 3. Ferromagnetic materials and their properties

Material	**Remanant Magnetization (10^6 A/m)**	**Coercive Field (A/m)**
Iron	1.71	80
Cobalt	1.42	795
Nickel	0.48	55

5.1.2 Magnetic Actuation Techniques

There are two ways to control magnetic material (Figure 18). If there is a uniform magnetic field, a magnetic dipole moment will reorient itself in the direction of the field. The misalignment with the field induces a magnetic torque on the dipole moment. In addition, magnetic bodies attract towards regions of higher intensity magnetic fields. In other words, a magnetic force will move a magnetic dipole in the direction of the field gradient.

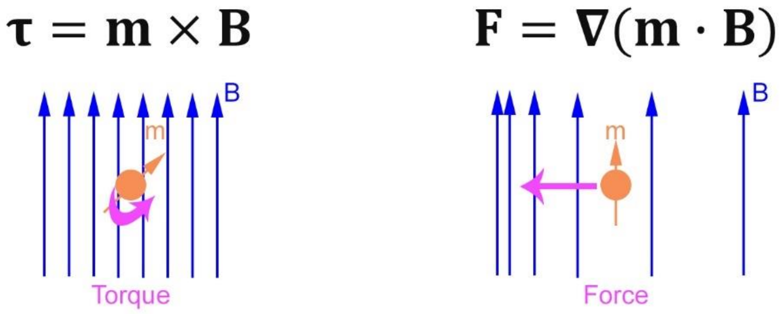

Figure 18. Magnetic actuation principles result in a torque and a force. The torque is due to the misalignment of a dipole moment with the magnetic field. The force is in the direction of the field gradient.

Different types of magnetic fields can be applied to actuate magnetic microstructures (Figure 19). For instance, magnetic fields that rotate in-plane or along the mantel of a cone can create complex movement. Alternatively, a constant magnetic field can alternate between on and off states. These types of fields induce a torque on a magnetic object. Forces can also act on magnetic microstructures in the direction of a field gradient that can occur either parallel or perpendicular to the magnetic field.

Often, these magnetic fields are created through the use of a permanent magnet or an electromagnetic coil. A permanent magnet inherently has a gradient towards its surface. These magnets have often been paired with a second magnet to maintain a constant field. Magnets have also been rotated or oscillated to control magnetic bodies. More commonly, magnetic fields are created with an electromagnetic coil with a soft ferromagnetic core. By controlling the current, complex magnetic field signals can actuate magnetic objects for rheological measurements.

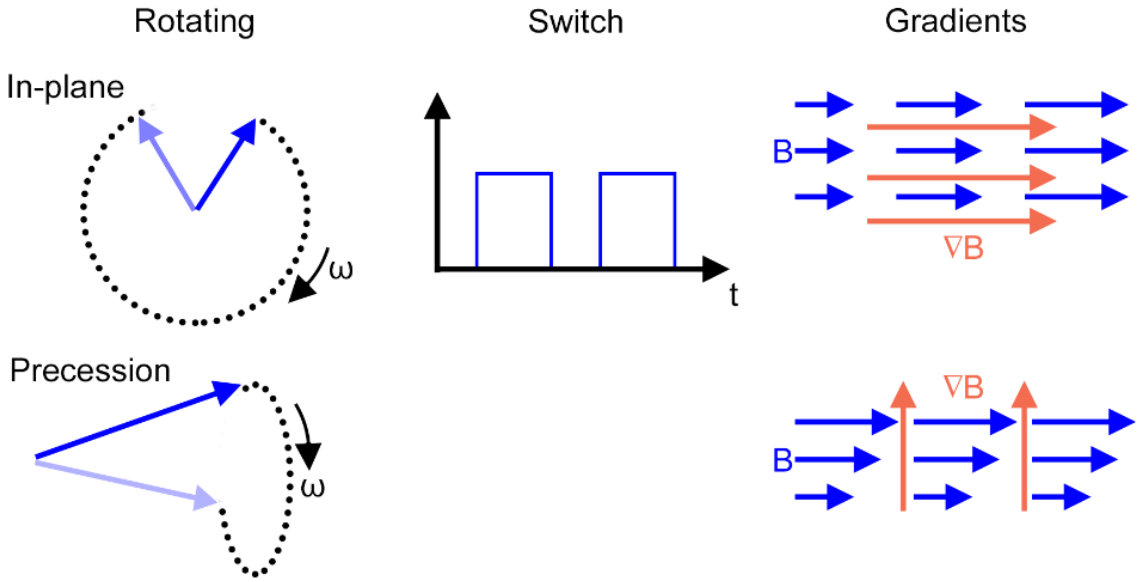

Figure 19. Types of magnetic fields for actuation to induce a torque or a force.

5.2 Magnetic Micropost Fabrication

5.2.1 Initial Fabrication Method

Initially, the process we used to embed particles into posts was based on a previous technique within our lab (Figure 20). This involved taking a PDMS negative mold from a silicon master. Carbonyl iron particles (BASF), with a diameter of 1-3 µm, were mixed into uncured PDMS at a 1:1 ratio by weight. A high strength magnet (200 mT) was placed underneath the mold to pull the particles into the microstructures. The time allotted for this process was 30 minutes, after which the mold was lifted off the magnet and a glass slide was used to scrape the excess PDMS away. Fresh PDMS was then placed on the mold and this was cast onto the glass at 110 °C for 24 hours. The negative old is peeled away and the final microstructures remain on the glass.

The silicon master used in this case are the force sensors presented in the third chapter – an array of block-post pairs. However, the size of these features was increased due to the failure to magnetize the smaller features with iron microparticles and nickel nanowires consistently. The posts in these arrays are 19 µm in diameter and 77 µm in height, which should allow for the deposition of small iron microparticles.

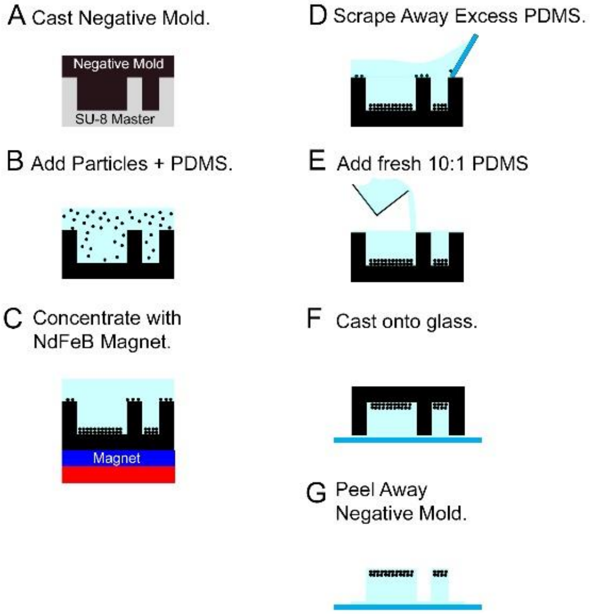

Figure 20. The initial method to embed carbonyl iron particles included using a 200 mT magnet in the third step.

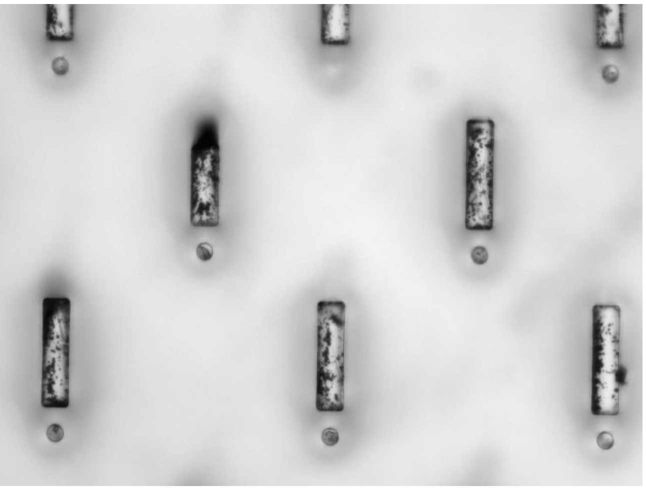

Figure 21. A representative image for microstructures cast at with 200 mT embedding field for 30 minutes. The image illustrates a lack of particles in the posts while clusters appear in the block.

However, this process did not work and in fact yielded less than 10% magnetic posts. In the represented image (Figure 21), the particles appear in the block, but their presence in the posts is sparse. Within the block, the particles appear to form clusters. In fact, under the microscope, a small droplet of these particles in PDMS was placed on a glass slide. Upon exposure to a high magnetic field, the particles appeared to form long chains and these dense chains formed larger clusters. This process occurred within a few minutes. A paper on aggregation kinetics of carbonyl iron particles further confirms these observations that the particles will form chains and it is depending on the magnetic field as well as the concentration of particles [83]. Thus, I hypothesized that these particles clustered into larger structures much bigger than the intended post diameter and at a faster rate than particle deposition into the post.

5.2.2 New Fabrication Method of Bigger Microstructures

To test this this hypothesis on iron microparticle deposition into microstructures, the method was altered to test various magnetic field strengths (0 mT, 7 mT, 35 mT, 65 mT, 200 mT) and various embedding times (3, 10, 30 minutes). Just from the representative images alone, it is clear that as magnetic field increases, the particles cluster in the block and none appear in the posts (Figure 22). It was found that only the substrates with 0 mT or 7 mT had significant amount of magnetic material.

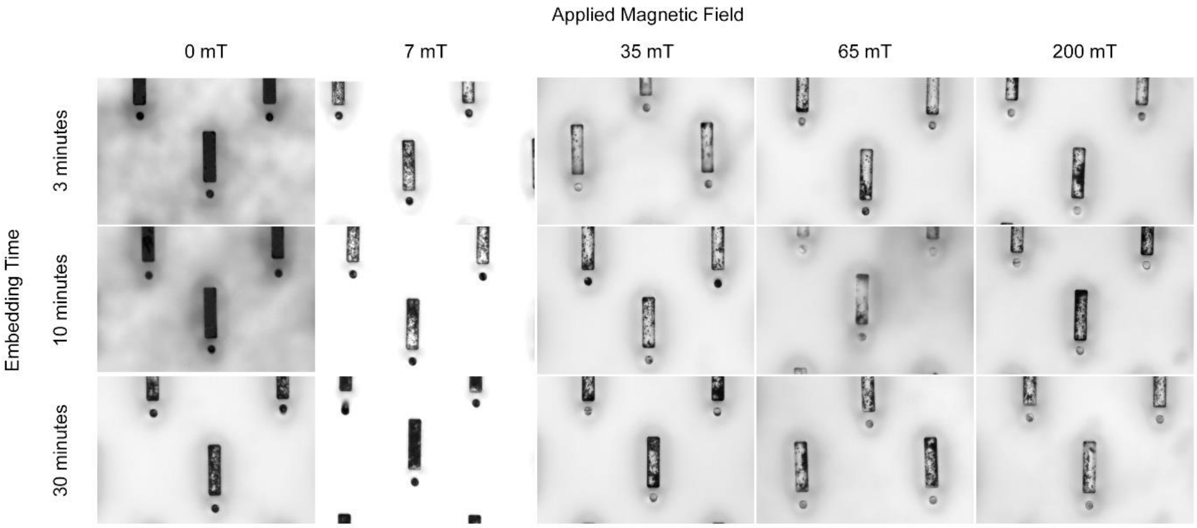

Figure 22. Representative images of magnetic posts that experienced a specific magnetic field for a certain amount of embedding time. The posts that experience little magnetic field retained more particles within the post.

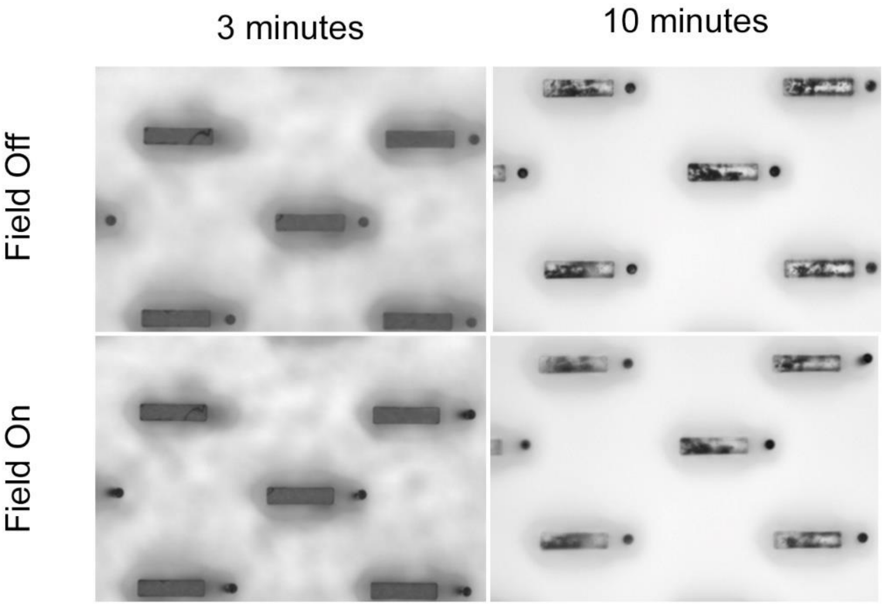

Figure 23. Representative images for 7 mT samples for an embedding time of 3 and 10 minutes. Under a magnetic field from a bar magnet, the 3-minute embedding time was more effective. Also note, the 10-minute samples appear to exhibit clustering.

This determination was based on the deflection from a bar magnet as well as the visible appearance of particles. For example, you can see visible differences for the

7mT samples that allowed for embedding to occur for 3 and 10 minutes (Figure 23). In both cases, the post has magnetic material, but for the 10-minute case, the particles in the block appear to have clustered over the longer timeframe. In addition, under the influence of a magnet, the post deflects further for the 3-minute 7 mT sample. Thus, the final method does not necessarily need to a significant amount of time to embed particles. Lastly, it should be said the 0 mT samples also had magnetic particles and deflected under the influence of a bar magnet. However, this movement only occurred when the bar magnet was at closer proximity to the sample than what was required for some of the 7 mT samples.

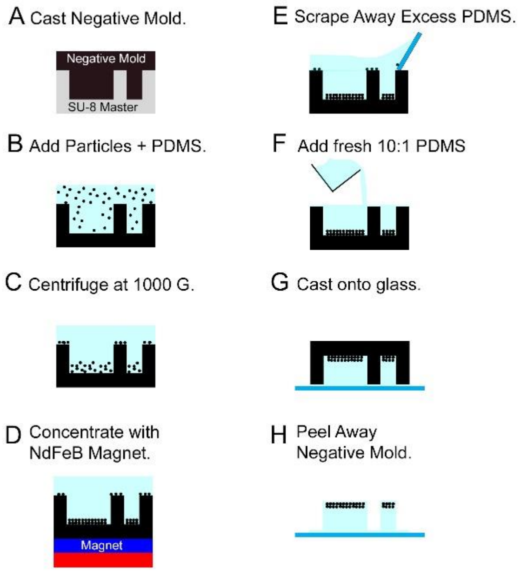

Figure 24. The final method to embed magnetic particles includes a centrifugation step (C) and a low strength magnet (D) in order to deposit magnetic particles.

The preliminary results suggested two steps were necessary. The 0 mT samples had magnetic material due to sedimentation from gravity. Thus, a centrifuge step was added to the protocol such that instead of 1 G-force, particles would be allowed to embed into the sample at 1000 G for 3 minutes (Figure 24C). Afterwards, the molds were placed over a 7 mT magnet for one minute (Figure 24D). The reason for the magnet is to reorient all the dipole moments of each particle in the same direction rather than the scattered orientations that might occur during sedimentation. Afterwards, the rest of the steps remained the same in terms of the casting protocol.

The result of this process yielded magnetic posts (Figure 25), in which a majority of the magnetic material could be found at the tip of the post. In addition, the initial concentration was reduced to 10% weight because it was found that the initial concentration of 50% now filled the magnetic post and it did not bend like a beam and rather, moved as a solid body.

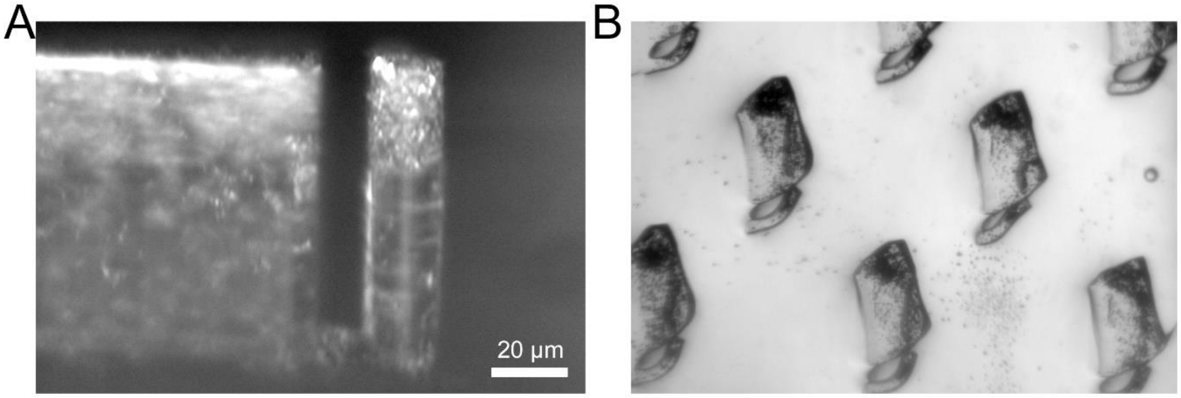

Figure 25. Representative images to visualize where the magnetic material appears in the post. (A) A side view of the magnetic posts cast using the final embedding process. (B) An image of block-post sensors after being forced down for imaging.

5.2.3 Revised Method for Small Microstructures

This method to embed carbonyl iron microparticles with a diameter of 1-3 µm is effective for structures such as these posts with a diameter of 19 µm. However, while attempting this same protocol on smaller structures such as the microfluidic devices presented in Chapter 4 or even smaller microposts with a diameter of 2-3 µm, the protocol failed to embed magnetic particles. This is most likely due to the size of the carbonyl iron particles being near the diameter of the post. Thus, I hypothesized a slightly smaller particle would resolve the issue of embedding in these microstructures.

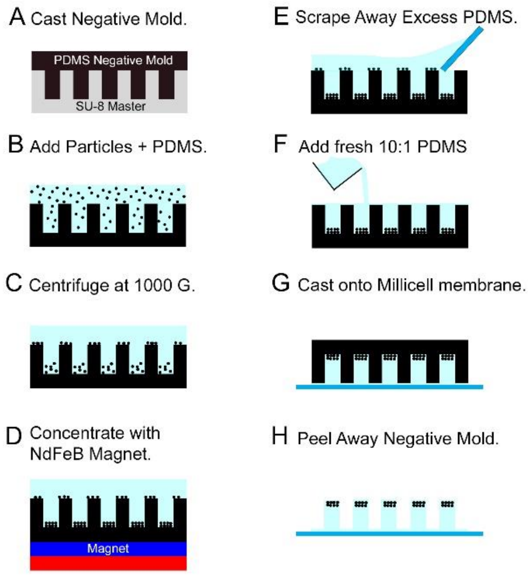

Figure 26. The embedding protocol for magnetic microposts is similar except B & C are repeated in order to ensure deposition of enough particles.

To test this theory, Ni particles (Sigma Aldrich) with a diameter less than 1 µm replaced the carbonyl Fe microparticles. Both the original microfluidic device with a micropost diameter of 6 µm, 25 µm height and microposts molds with 2.5 µm diameter, 12 µm height were used. Because of the smaller size, the concentration was increased back to 50%. This proved effective but there was still not enough magnetic material. Therefore, the centrifugation step (Figure 26B, C) was repeated twice in order ensure particle deposition occurs properly. This proved successful in the microposts but it did not produce the same amount of desired force in the microfluidic force sensors since the magnetization of the Ni is approximately a quarter of Fe (Table 3). For the microfluidic assay presented in Chapter 4, spherical iron particles with a diameter of 800 nm (US Research Nanomaterials) were used. The protocol is able to produce magnetic posts consistently though the amount of magnetic material tends to vary from sensor to sensor.

5.3 Magnetic Actuation Device

5.3.1 Actuation by a Torque Magnet

In order to actuate the magnetic posts, a specialized magnet known as a torque magnet was used to change the magnetic dipole moments. It is created by Correlated

Research (CMR), a company that specializes in ‘smart’ magnets. These magnets are ‘smart’ because rare earth materials are given specific patterns of different polarity (north or south), to yield a composite magnetic field completely unique from a conventional magnet. For example, CMR has a pair of magnets that attract at a certain distance, but as the magnet are brought together past a set distance, the repulsion forces between them increase, and the result is hovering magnets. As another example, one of the intended purposes of the torque magnet is to use them as in a pair to create a twist-release system for locking and unlocking. Another possible use is frictionless gears. These magnets draw motivation from Halbach arrays, which uses a rotating pattern of magnets to cancel fields on one side of the array while increasing the field on the other side.

5.3.2 Theoretical Model for Actuation

To characterize the movement of the magnetic micropost, a multipole ring magnet (Torque Polymagnet #1001122, Correlated Magnetics) was attached to the axle of a servo motor (Futaba). The servo was programmed to sweep between -10 to 10 degrees at steps of 2 degrees. As the ring magnet was rotated, the strength of the magnetic field in each cartesian direction was measured using a magnetometer (Lake Shore Cryotonics). The location of its Hall probe tip was positioned 1 mm above the magnet and 8 mm from its center axis for the measurements (Figure 27A). The field gradient of the magnet was also measured for different gap distances between the surface of the magnet and the magnetometer (Figure 27B).

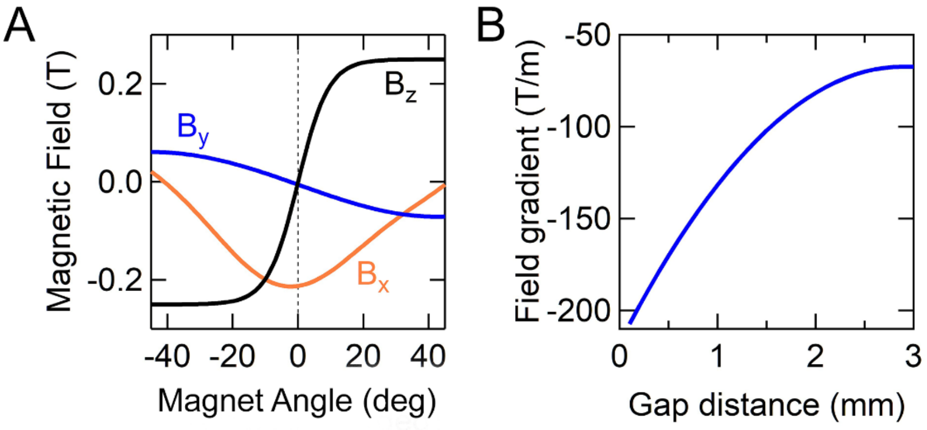

Figure 27. The surface magnetic field of the torque magnet measured with a magnetometer it (A) rotated via a servo motor. (B) The field gradient in the z-distance was also calculate based on measurements.

For our testing, we required a model that describes the actuation of a magnetic post based on the rotation of the ring magnet. Specifically, we used an energy minimization model for a flexible magnetic cantilever to find the deflection angle at its base, which is an approach that is similar to previous studies [82, 84, 85]. Here, the total energy of the system includes the elastic strain energy of the cantilever due to its bending and the magnetic energy of the cluster of iron particles due to the alignment of its dipole with respect to the applied magnetic field. The cantilever has a diameter D and contains two distinct sections: an elastic section at its base with a length L_e and a magnetic section at its top with a length L_m (Figure 28A). The bending stiffness of the block is considerably greater than the post, so we can consider its magnetic actuation due to an applied magnetic field to be negligible.

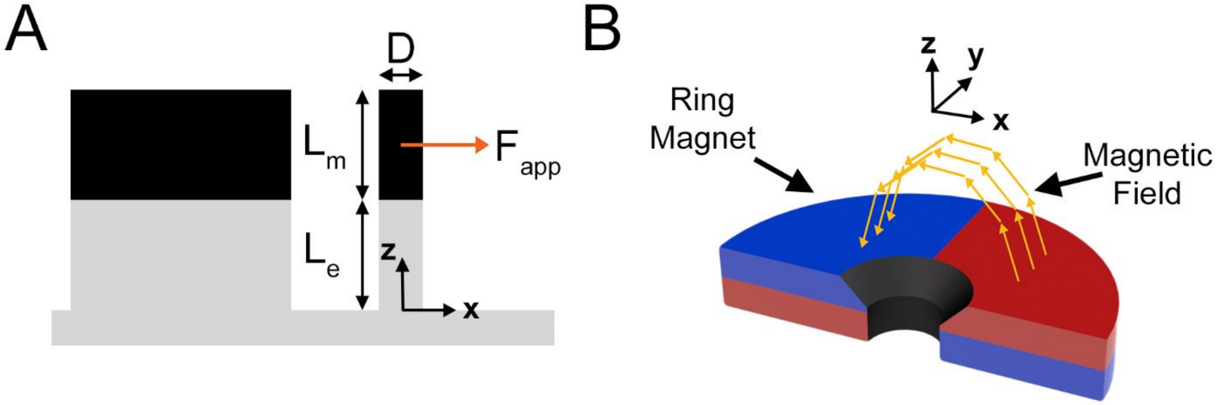

Figure 28. Conceptual illustrations for magnetic model. (A) A diagram to define different parameters in the model and (B) the magnetic field for the ring magnet.

For our system, we used a multipole ring magnet that contains four quadrants, with adjacent quadrants having magnetic dipoles with opposite orientations. As a result of the opposing poles, the magnetic field creates an arc that spans across the interface between two quadrants (Figure 28B). We defined our cartesian coordinate system to be centered at where a micropost would be situated above the ring magnet and to be oriented along the length of the interface of the ring magnet when it is positioned at zero degrees. As the magnet rotates, the post bends by a deflection angle ϕ from the vertical axis due to the presence of a magnetic field in the same plane (Figure 29A). To characterize the magnetic field, we rotated the ring magnet ±10 degrees and measured the magnetic field in each cartesian direction where the microchannel would be placed (Figure 27). From these measurements, we calculated the magnitude of the field $|\vec{B}|$ (Figure 29B) and its angle (ψ) (Figure 29C).

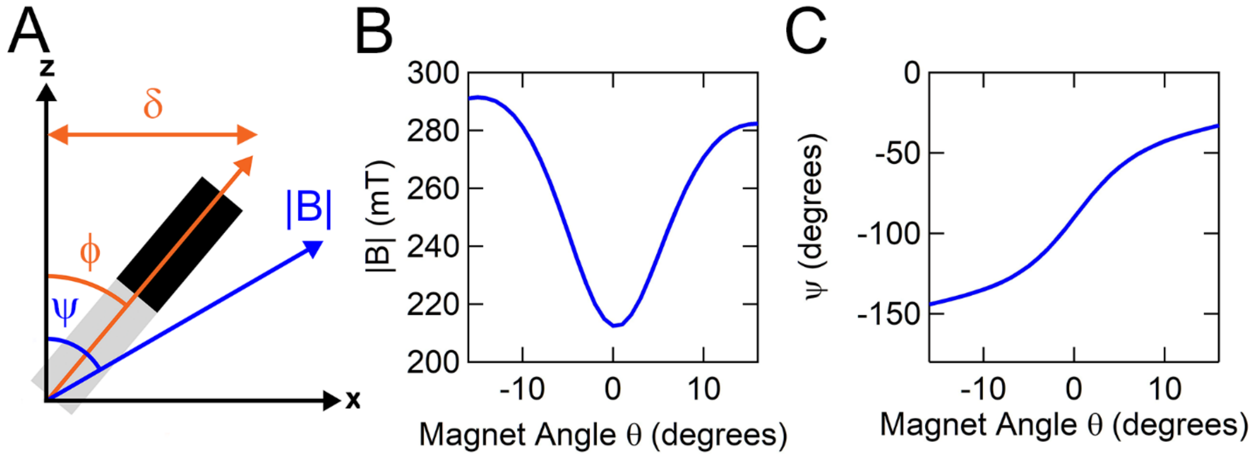

Figure 29. Magnetic Field Application. (A) The diagram to define direction for each vector in the model. The (B) magnetic field magnitude and (C) field angle were measured and used in the model.

Consequently, we are able to assume that the magnetic energy due to the magnetic field dominates over its gradient [84, 85] . To determine if the magnetic field dominates the gradient of the field, I needed to compare the ratio between the gradient term and field term derived from Evans, et. al. [85], which assumes the optimal angles for the gradient of the field (perpendicular to the post) and magnetic field (45 degrees with respect to the post). The ratio simplifies to

$$\frac{gradient}{field} = \frac{\frac{1}{2}L_m|\nabla B|}{2(n_r - n_a)\mu_0 M(B) f} \tag{9}$$

where $M(B)$ is replaced with the magnetic saturation for the extreme case, μ_0 is the permeability of free space, and f represents the fraction of the total volume of the magnetic section that accounts for the iron particles. We estimated the volume of iron to account for 10% of the total volume of the magnetic section. This estimate takes into consideration the concentration of particles used to fabricate the posts (10-33%) and the volume fraction possible for hard spheres packed within the cylindrical shape of the magnetic section of the post (64%) (Figure 30A).

Additionally, n_r and n_a represent the radial and axial demagnetization factors defined by the shape of the magnetic section (Figure 30A, B) [84]. The inverse of demagnetization factor defines its susceptibility χ in each direction (Figure 30C) but this is only valid for soft ferromagnetic materials. The susceptibility indicates the level of magnetization for a material in the presence of an applied magnetic field. Thus, with a longer magnetic section, the magnetization increases along its length as seen in Figure 30C. I assumed the cylinder was a prolate ellipsoid and as defined by Abbott et al [84], the demagnetization factor is theoretically defined as

$$n_a = \frac{1}{R^2-1}\left(\frac{R}{2\sqrt{R^2-1}}\ln\left(\frac{R+\sqrt{R^2-1}}{R-\sqrt{R^2-1}}\right)-1\right), \tag{10}$$

$$n_a + 2n_r = 1 \tag{11}$$

where R ≥ 1 is the ratio between the length of the magnetic section and diameter of the post.

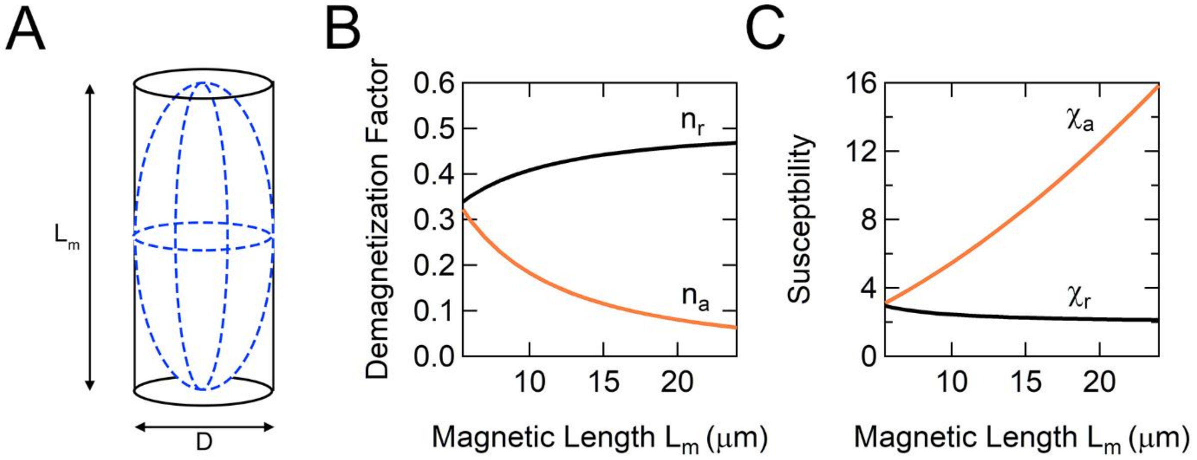

Figure 30. Demagnetization Factors. (A) The magnetic tip is a cylinder but estimated as a prolate ellipse to determine (B) the demagnetization factor. The inverse of the demagnetization factors is the (C) susceptibility.

We also assumed the magnetic field we applied is below the level needed for saturating the iron particles (Figure 31) The low and high field define the regions for which the magnetization is less than or equal to the saturation, respectively, and these equations are defined elsewhere [84]. More importantly, based on these equations, the applied magnetic field (Figure 29B) is always below these levels.

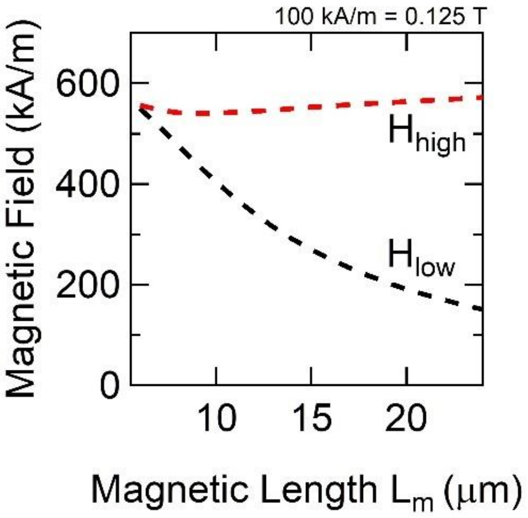

Figure 31. Theoretical low and high field changes with magnetic length.

With these considerations in mind, the energy minimization model reduces to a simple balance between the elastic torque due to the bending stiffness of the post (τ_e) and the magnetic torque due to the applied field (τ_m) [82],

$$\tau_e + \tau_m = 0. \tag{12}$$

Assuming the magnetic post bends at a constant radius of curvature, the elastic torque is given by

$$|\tau_e| = \frac{\pi E D^4}{4L_e}\phi, \tag{13}$$

where ϕ is the deflection angle and E is the elastic modulus of PDMS (3 MPa). Furthermore, the magnetic torque acting on the post is given by

$$|\tau_m| = \frac{V|n_r - n_a|}{2\mu_0 n_r n_a}\left|\vec{B}\right|^2 sin\big(2(\phi - \psi)\big), \tag{14}$$

where V is the volume of iron, defined as 10% of the volume of the magnetic section, n_r and n_a represent the radial and axial demagnetization factors (Figure 30A,B) [84], and μ_0 is the permeability of free space.

To determine the bending stiffness of the magnetic post (k_{post}) and the applied force for a given magnetic field (F_{app}), we needed to determine the length of the magnetic section (L_m) because it principally influences equations 12-14. The walls of the microchannels obstructed our ability to obtain a sideview image of the magnetic posts, but we could estimate a value for L_m by measuring the deflection of a post relative to the applied magnetic field. Thus, we used equations 12-14 and our measurements for $|\vec{B}|$ and ψ to calculate the deflection of a post for different values of L_m (Figure 32). From Castigliano's method, we derived the applied force (F_{app}) based on the deflection (δ) of the post:

$$F_{app} = k_{post}\delta = \frac{3\pi ED^4}{16\left(4L^3 - 3L^2L_m - L_m{}^3\right)}\delta, \tag{15}$$

where $L = L_e + L_m$. Thus, by estimating L_m in this manner, we could determine k_{post} and F_{app} for Chapter 6. We assumed F_{app} acted at the center of L_m and that bending of the micropost occurred only in its elastic section defined by L_e (Figure 28A).

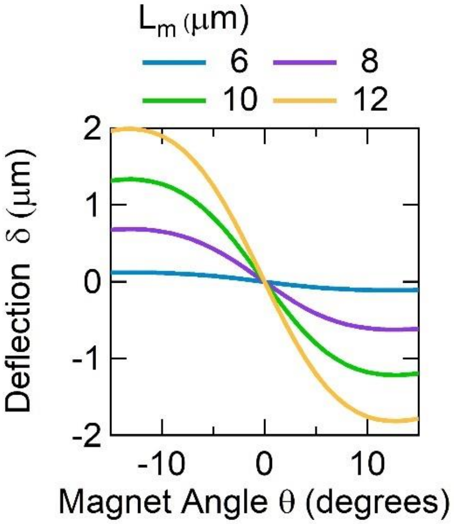

Figure 32. Characteristic curves of deflection for different magnetic lengths.

5.3.3 Experimental Use of the Model

A microfluidic device was placed above the rotating magnet for that its microchannel was at the same position where the magnetic field measurements were taken. Using a metallurgical microscope (Nikon LV-100) and a 20× objective, a sequence of images was taken by a camera (Hamamatsu C11440) to record the deflection of the post for a given rotation angle of the ring magnet. The deflection of the magnetic post was then compared to the measured magnetic field at each angle.

With these characteristic curves, we were able to determine L_m for each micropost we used in our studies based upon our measurements of its deflection, an example of which is shown in Figure 33.

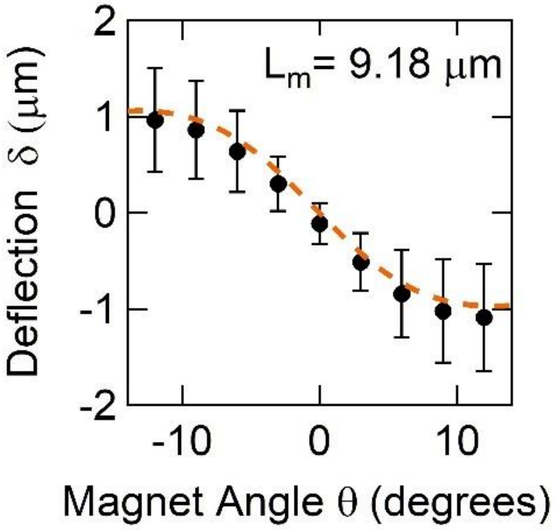

Figure 33. Estimating the length of the magnetic section based on experimental data.

5.3.4 Notes on Assumptions

One important consideration about the model is the estimation of iron particles embedded in the magnetic section of the post. The total volume of iron had to be less than 20% of this section based on the 1:1 ratio by weight and the packing density of spheres in a cylinder. Therefore, I simulated how the post's stiffness (k_{post}), the total deflection for ± 10 degrees of magnet rotation (amplitude), and the applied force of the post, changed with respect to the length of the magnetic section and the corresponding post stiffness (Figure 34). The maximum deflection occurs when the magnetic section accounts for about 75% of the post and the higher concentration increases the magnetic torque considerably. While the length of the magnetic section could not be imaged for the smaller post, the average amount of magnetic material deposited in the bigger post accounted for approximately 40% of the length of the post. If the same deposition ability translated to the smaller post, the average length should be about 10 µm. However, the maximum amplitude of the posts during the experiment was less than 2.5 µm. In a separate calibration experiment, the maximum amplitude of the post was 5 µm, most likely due to better deposition. Therefore, it is much more likely the volume of iron is around 10% of the total volume of the magnetic section.

Another assumption about this model is the movement of the post is not due to an increasingly stiff post with a large magnetic section. This is because based on the experimental data collected and discussed in Chapter 6, the maximum amplitude would correspond to a bending stiffness that would suggest the platelet-rich plug generated forces in the micronewton range. This is well over the range registered with the block-post device and even previous measurements using different assays. Thus, it is more likely the post is much softer with a reasonable amount of magnetic material to account for the total deflection.

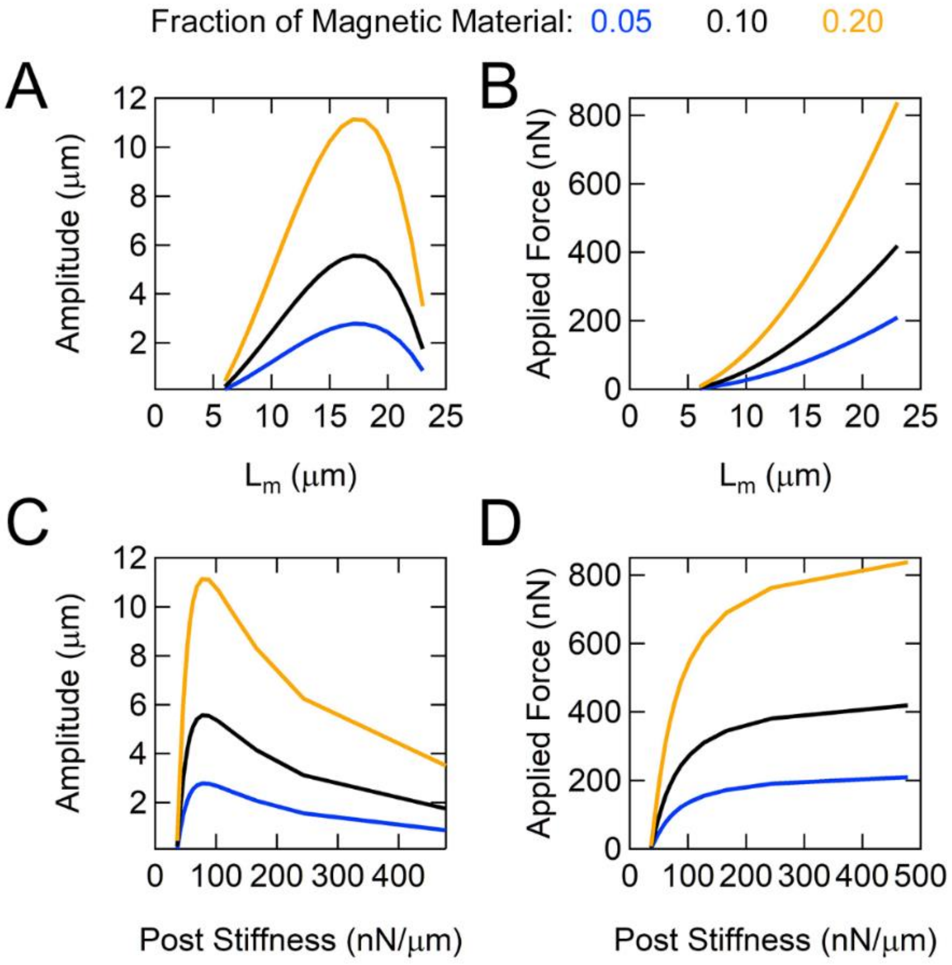

Figure 34. Simulation for fraction of magnetic material. Note, the post stiffness is dependent on magnetic length.

5.3.5 Torque Magnet Actuation Device Design and Capabilities

A simple system was designed to rotate the torque magnet (Figure 35). A stepper motor controls the rotation of the magnet through a dual axis pulley system. The pulley system consisted of a 180 mm urethane timing belt connected by two aluminum T5 timing pulleys. Additionally, a torsion band was used to remove slack in the timing belt. The pulleys' height was maintained using plastic washer bearings, which also allowed for smooth rotations. Attached to one pulley was a 3D-printed holder to hold the ring magnet. On the other end, another 3D-printed part connected the stepper motor to the pulley. The entire device was held together with an aluminum base and support. The microfluidic card with these magnetic posts was enclosed in a 3D printed holder attached to a micromanipulator. By doing this, any possible vibrations from the actuation device were separated from the microfluidic card. Additionally, a thin PDMS coating was placed below the aluminum base to dampen the vibrations from the motor.

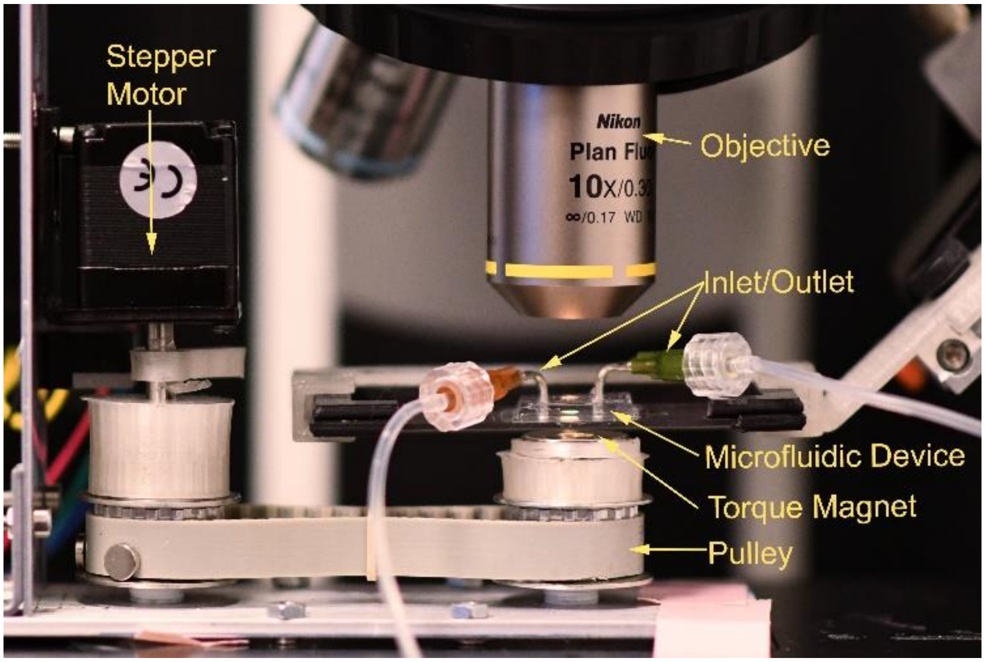

Figure 35. The final actuation device is a dual axis stepper motor driven pulley system to rotate the torque magnet. A metallurgical microscope with a 10x objective allows visualization of the iron posts. The microfluidic card is held in a custom holder attached to a micromanipulator.

A microprocessor (Arduino Uno v3) controlled the movement of the stepper motor. The step size of the motor must be hardwired as shown in the wiring diagram (Figure 36). Each full-step was 1.8 degrees (200 steps/revolution) but hardwiring allowed for microstepping capabilities, which decreased the angle for each step as described in Table 4. The driver also had a built-in potentiometer to control the current. To protect the driver and motor from a short circuit, a 100 µF capacitor was placed between the voltage in and voltage out pin.

Once hardwired, the two variables the stepper motor considers are the step size and delay between step sizes. As different microstepping options were tested, the potentiometer on the driver needed to be rotated because each configuration required a specific amount of current. Too much current increased the torque from the motor but also increased the vibrations. Based on the smallest step size possible, without any vibration problems from the motor, the frequency of rotations was determined (Table 5). From our observations, we decided to hardwire the processor to take 1/1600th of a step because it ensured smooth movement at a maximum angular velocity of 2 rad/s.

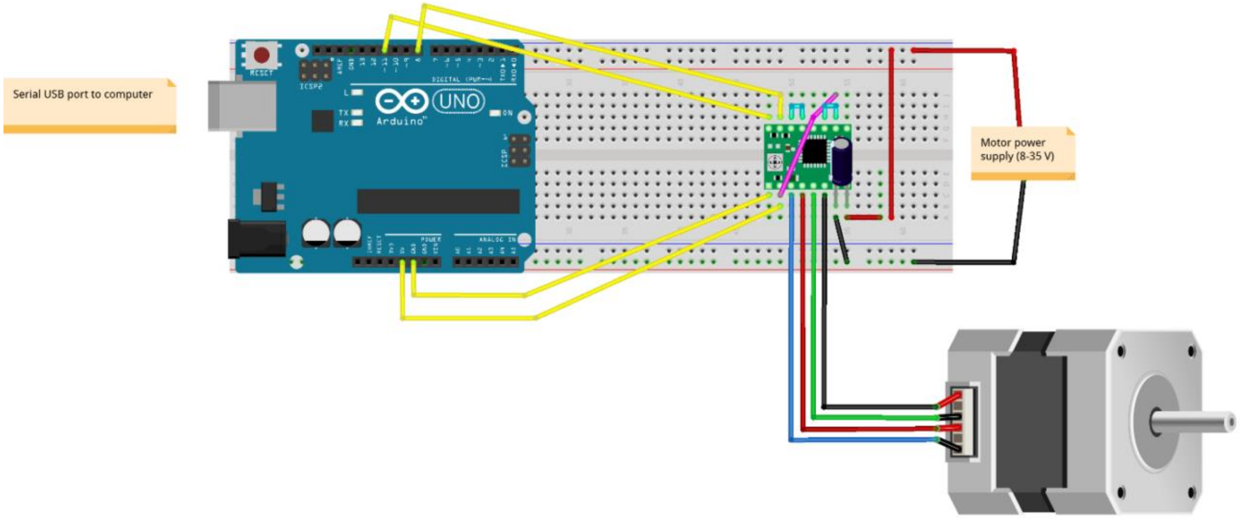

Figure 36. Wiring diagram for the magnetic actuation device between the Arduino, A4988 driver and stepper motor. A custom 3d-printed holder was made to house the Arduino and electrical board to protect it during blood experiments.

Table 4. Pull-up resister combinations on A4988 driver for microstepping resolution.

MS1	**MS2**	**MS3**	**Resolution**
LOW	LOW	LOW	Full Step
HIGH	HIGH	HIGH	Half Step
LOW	HIGH	LOW	Quarter Step
HIGH	HIGH	LOW	Eighth Step
HIGH	HIGH	HIGH	Sixteenth Step

Table 5. Characteristic for each step size resolution.

Step Size	**Steps Per Revolution**	**Total Steps For 10 degrees**	**Max Angular Velocity (rad/s)**	**Vibration Interference**
Full	200	5	16	Yes
Half	400	11	8	Yes
Quarter	800	22	4	No
Eighth	1600	44	2	No
Sixteenth	3200	89	1	No

The frequency of the signal was simulated based on the number of steps, which controls the magnet rotation angle in one direction, and the angular velocity of rotation, defined by the delay between steps (Figure 37). If the magnet rotates ± 1 degree at 2 rad/s, the posts should actuate at nearly 30 Hz. However, experimentally, the movement of the post was not reliable until at least a sweep of ± 3 degrees.

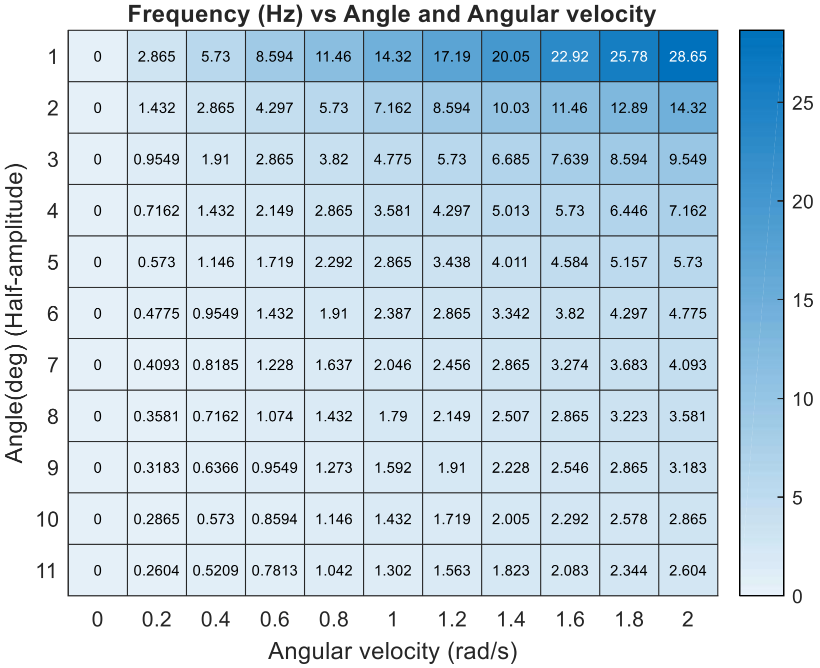

Angle(deg) (Half-amplitude) \ Angular velocity (rad/s)	0	0.2	0.4	0.6	0.8	1	1.2	1.4	1.6	1.8	2
1	0	2.865	5.73	8.594	11.46	14.32	17.19	20.05	22.92	25.78	28.65
2	0	1.432	2.865	4.297	5.73	7.162	8.594	10.03	11.46	12.89	14.32
3	0	0.9549	1.91	2.865	3.82	4.775	5.73	6.685	7.639	8.594	9.549
4	0	0.7162	1.432	2.149	2.865	3.581	4.297	5.013	5.73	6.446	7.162
5	0	0.573	1.146	1.719	2.292	2.865	3.438	4.011	4.584	5.157	5.73
6	0	0.4775	0.9549	1.432	1.91	2.387	2.865	3.342	3.82	4.297	4.775
7	0	0.4093	0.8185	1.228	1.637	2.046	2.456	2.865	3.274	3.683	4.093
8	0	0.3581	0.7162	1.074	1.432	1.79	2.149	2.507	2.865	3.223	3.581
9	0	0.3183	0.6366	0.9549	1.273	1.592	1.91	2.228	2.546	2.865	3.183
10	0	0.2865	0.573	0.8594	1.146	1.432	1.719	2.005	2.292	2.578	2.865
11	0	0.2604	0.5209	0.7813	1.042	1.302	1.563	1.823	2.083	2.344	2.604

Figure 37. The frequency was determined for different degrees of rotation (angle) and angular velocity to determine an upper and lower limit.

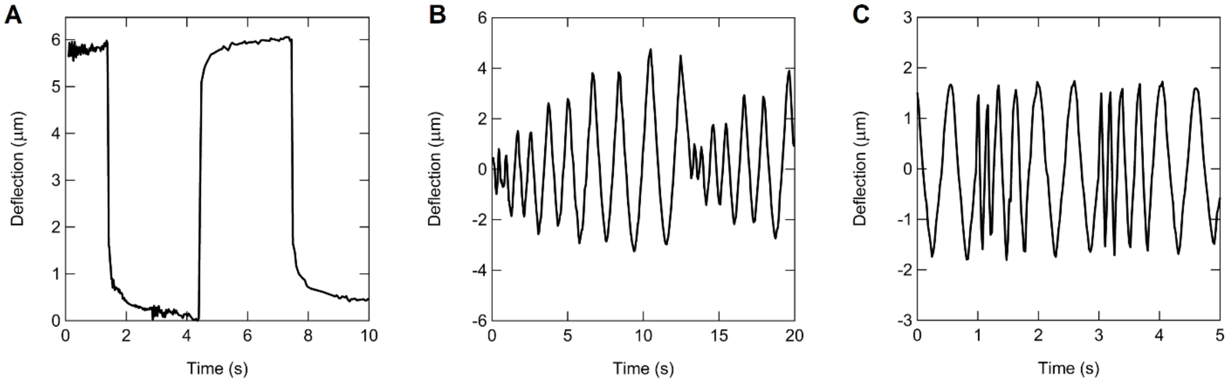

Figure 38. Different programs can be written to control the movement of the post such as a (A) step function, (B) amplitude increase, or (C) frequency increase.

Programs were written based on the step size and delay to control the post in different ways. For instance, a constant force can be applied for a period of time (Figure 38A), an amplitude increase at a constant frequency (Figure 38B), a frequency increase at a constant amplitude (Figure 38C), or any combination of these programs. For the experiments presented in Chapter 6, the stepper motor was programed to rotate between ± 10 degrees.

6. Mechanobiology of Platelet-rich Plugs

6.1 Background

Upon vascular injury, platelets form strong attachments to the exposed extracellular matrix to stem bleeding [11]. Platelets halt their circulation in the blood flow by adhering initially to surface bound von Willebrand Factor (VWF) before fully attaching to collagen. Once bound, platelets become activated and release soluble agonists to recruit more platelets to aggregate onto the growing structure of the platelet-rich plug. While this growth occurs, platelets produce contractile forces by actin-myosin interactions that retract their shape and reduce the gaps between adjacent platelets, which compacts the size of the plug and concentrates the agonists with its central region [55, 57, 86]. Further stabilization of the plug into a fibrin-based clot occurs through coagulation, but the early response from platelets to hemostasis is vital and often assessed and targeted in clinical or surgical settings [7].

A hemostatic plug must be strong enough to withstand hemodynamic forces that can dislodge it from an injury site [53, 87]. In general, fibrin-based clots that are soft fail to staunch bleeding, while those that are stiff lead to thrombosis, stroke, and myocardial infarction [53, 87]. Previous studies indicate that myosin-based forces by platelets promote greater adhesion to stiffer environments [58]. Moreover, platelet forces can modulate the stiffness of a clot by stretching its fibrin strands to induce strain hardening [18, 60, 61, 88-91]. There is growing appreciation that platelets are able to sense and respond to mechanical cues, but the role of mechanotransduction by platelets during the early phases of hemostasis is unclear [17].

Here, we present the development of an approach to measure the mechanotransduction response of platelets during shear-induced formation of a platelet-rich plug. It is an innovation from our previous microfluidic assay that uses microscale blocks and flexible microposts to measure the forces within a platelet-rich plug [12]. Since magnetic particles can be added to polydimethylsiloxane (PDMS) structures like microposts [20, 21, 82, 85, 92], we are able to embed our microposts with iron particles, and in the presence of a magnetic field, use them as mechanical actuators that apply external force to aggregated platelets during the formation of a platelet-rich plug. In this manner, we can measure the stiffness of the plug and the contractile force of the platelets in tandem during the formation of a plug. We find that the mechanotransduction response by platelets that affects plug stiffness is dependent on the magnitude of external force we apply. This mechanotransduction response is still present when VWF-based aggregation, platelet activation, or myosin-based forces are inhibited.

6.2 Materials and Methods

6.2.1 Blood handling

Whole blood was collected from human subjects under a protocol approved by institutional review board (IRB) at the University of Washington. Blood was collected in sodium citrate tubes (0.109 M/3.2%, 2.7 mL, BD Vacutainer). The blood was pooled into a 50-mL container and allowed to mix on a slow rocking agitator for at least ninety minutes prior to testing.

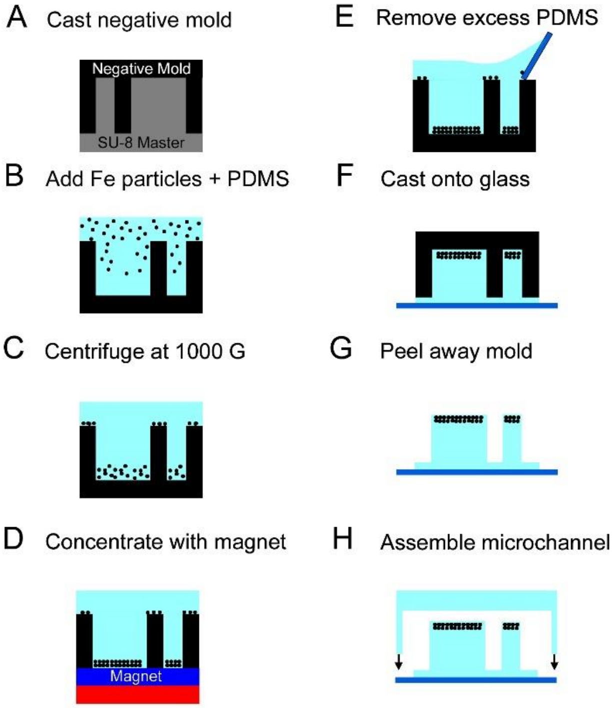

Figure 39. Microfluidic device fabrication for magnetic block-posts in a channel.

6.2.2 Microfluidic Device Fabrication

Microfluidic devices were fabricated using soft lithographic techniques with a silicon master. The silicon master had three microfluidic channels that were 3 cm in length, 50 µm in height, and 200 µm in width that contained an array of blocks and posts. The blocks were 25 µm in length, 25 µm in height, and 15 µm in width, while the posts were 6 µm in diameter and 25 µm in height. For the soft lithography process, a negative mold was cast using polydimethylsiloxane (PDMS) (Sylgard 184, Dow Corning) (Figure 39A). The surface of the negative mold was exposed to plasma (Plasma Prep II, Structure Probe, Inc.) and then treated with the vapor phase of tridecafluoroctyltrichlorosilane (United Chemical Technologies) while under vacuum pressure in a desiccator for two hours to prevent subsequent bonding. Next, iron particles with a diameter of 800 nm (US Research Nanomaterials, Inc) were added to the uncured PDMS at a 50:50 ratio by weight and then degassed. The Fe-PDMS mixture was then poured onto the negative molds (Figure 39B), which were centrifuged for 3 minutes at 1000 RCF to drive the particles to the tip of the post (Figure 39C). Afterwards, the molds were placed above a 10 mT magnet for 1 minute to cluster the particles together (Figure 39D). The excess amount of Fe-PDMS mixture on the top of the negative mold was scraped away with a glass slide to ensure that the final devices would be optically transparent for imaging under a microscope (Figure 39E). An additional amount of uncured PDMS (without Fe particles) were added onto the mold, attached to a clean glass slide, and baked at 110 ºC for more than 15 hours (Figure 39F). After curing, the mold was peeled away to leave open-top channels with an array of magnetic block-post sensors as the base layer of the microfluidic device (Figure 39G). The top layer of PDMS was made using a custom-built aluminum mold with pegs for the placement of silicon tubing (0.040-inch ID/0.085-inch OD, HelixMark) to form the ports at the inlets and outlets of the microchannels. The top and base layers of the microfluidic device were exposed to plasma and then brought into contact to create a permanent seal between them (Figure 39H).

6.2.3 Surface Coatings

Microchannels were coated with rat tail collagen type I (BD Bioscience) by injecting it as a solution into each microchannel at a concentration of 200 µg mL^{-1} in 0.1 M acetic acid and letting it adsorb for one hour. Afterwards, it was rinsed by injecting Tyrode's buffer (10 mM HEPES, 138 mM NaCl, 5.5 mM glucose, 12 mM $NaHCO_3$, 0.36 mM Na_2HPO_4, 2.8 mM KCl, 0.4 mM $MgCl_2$) into the microchannel and then stored at 4 ºC until the time of the experiment.

6.2.4 Magnetic Actuation

To actuate the magnetic posts during the experiments with a blood sample, the ring magnet was mounted on a rotating axle that was situated underneath the microfluidic device. A stepper motor and a pulley system were used to control the rotation of the ring magnet. In this configuration, the rotation of the ring magnet by the stepper motor (Pololu #1205) was controlled by a motor driver (Allegro A4988 stepper) hardwired for 1/1600 steps to achieve smooth movement of the ring magnet as it was rotated from -10 and 10 degrees. A microcontroller (Arduino Uno v3) was programmed to repeat this pattern five times during a period of 40 seconds, followed by a 20 second duration without any rotations.

6.2.5 Microfluidic Testing Protocol

Blood was drawn into a 3-mL syringe (BD Scientific) and then injected into the microfluidic channel using a syringe pump (Harvard Apparatus). The flow rate of the blood was set such that the shear rate in the microchannel was 16,000 s^{-1} for the first 15 seconds of the experiment to form a platelet-rich plug. The shear rate was then reduced to 500 s^{-1} for the remaining time of the experiment to reduce the degree of aggregation and prevent the channels from becoming obstructed.

6.2.6 Measurement of Platelet Rich Plug Force and Stiffness

Using a metallurgical microscope (Nikon LV-100) encased in a live-cell chamber (In Vivo Scientific, Inc) to maintain a 37ºC environment, the experiments were recorded by a camera (Hamamatsu C11440) using a 20× objective. Videos were initiated prior to the onset of blood flow to capture the initial magnetic actuation of the microposts while in Tyrode's buffer and continued until the end of the test. After a full video was taken, the centroid of each post within the field of view was tracked, i.e. five posts per video, and its distance from the edge of the block was analyzed using a thresholding method in Fiji/ImageJ. The projected area of the plug was measurement using manual tracing in Fiji/ImageJ.

6.2.7 Biochemical Treatments

Recombinant ADAMTS13 was obtained and purified in a process described previously [43]. For each inhibitor experiment, either recombinant ADAMTS13 (1 µg/mL), acetylsalicylic acid (0.3 mM), or blebbistatin (5 µM, Sigma Aldrich) were incubated in the blood for 10 minutes prior to testing. For all control experiments, equivalent volumes of either HEPES-Ca^{2+} buffer (10 mM 4-(2-hydroxyethyl)-1-piperazineethanesulfonic acids with 2 mM $CaCl_2$) or DMSO was added.

6.2.8 Statistical Analysis

One-way analysis of variance (ANOVA) with Tukey's post-hoc test was used to determine the significance between multiple groups. Significance was denoted for $p < 0.05$. Linear regression analysis was performed using least absolute deviation (L_1 method).

6.3 Results

6.3.1 Magnetic actuation of microposts with embedded magnetic particles

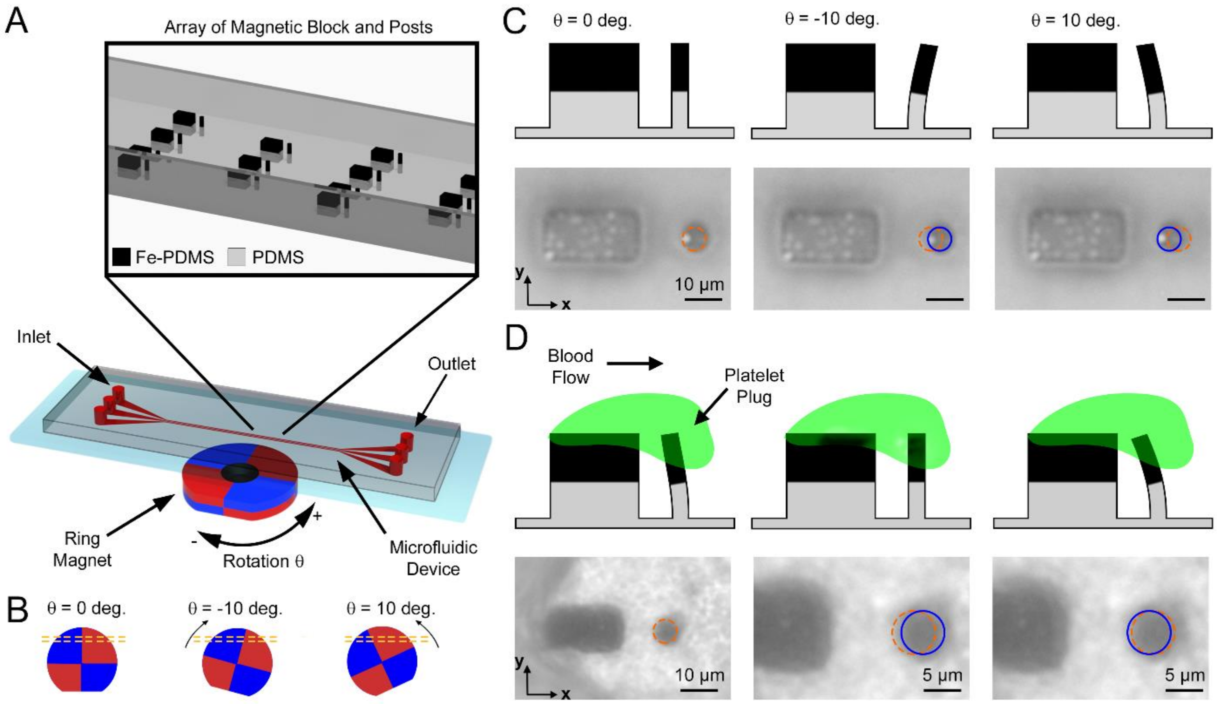

Figure 40. Conceptual illustration of magnetic actuation during platelet plug formation to determine contractile force and stiffness.

Our microfluidic devices contained an array of rigid blocks and flexible posts with embedded magnetic particles with which we can use to evaluate the contractile force of platelets and the stiffness of the platelet-rich plugs (Figure 40A). Magnetic actuation of the posts was accomplished by the rotation of a ring magnet that was situated underneath the microfluidic channel (Figure 40B). In this approach, the posts can be deflected by a magnetic force that acts on the cluster of iron particles embedded within the upper portion of the posts (Figure 40C). When blood flows into the channel, there is a shear gradient near the block that triggers the formation of a platelet-rich plug. During plug formation, we can track the displacement of the post towards the block, which indicates the contractile force of platelets (Figure 40D). We can also rotate the ring magnet to actuate the post and track its motion to measure the stiffness of the plug (Figure 40D).

Using equation 15 and the data we collected on the deflection of all microposts in our study, we found that on average, our magnetic posts can apply 12.9 nN of force and a few can achieve up to 40.8 nN of force (Figure 41). These results indicate that we can apply forces to a platelet-rich plugs using magnetic actuation to study their mechanotransduction response.

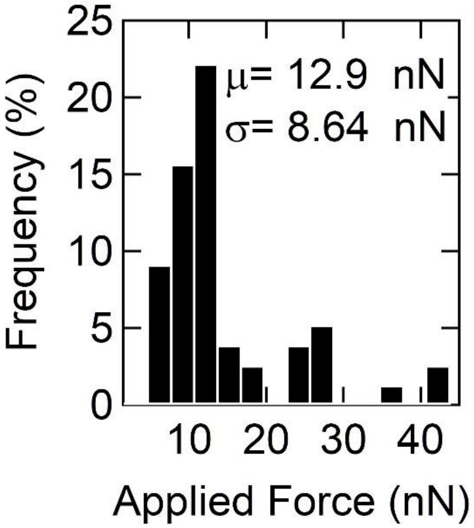

Figure 41. Distribution of applied forces for the experiments in this chapter.

6.3.2 Measurements of stiffening, force, and area during the formation of a platelet-rich plug

To examine the relationship between platelet forces and plug stiffness, a sample of whole blood was injected into the microfluidic channel at a shear rate of 16,000 s^{-1} for 15 seconds to form a platelet-rich plug on the block and post structures (Figure 42A). Immediately afterwards, the flow was reduced to a lower shear rate (500 s^{-1}) for the remainder of the test to prevent additional attachment of platelets to the plug. Before blood entered the channel, the magnetic posts were actuated five times by rotating the ring magnet (Figure 42B). We tracked the deflection of the post during this initial period to determine k_{post} and F_{app}, as mentioned earlier. This pattern of magnetic actuation was repeated five more times during testing with intermediate periods of no actuation. The displacement of the post increased steadily once blood entered the channel (denoted at t = 0) due to the contraction of platelets within the plug. We noted that the displacement of the post due to magnetic actuation was attenuated in the early phase of plug formation, but over time, the movement of the post became more pronounced.

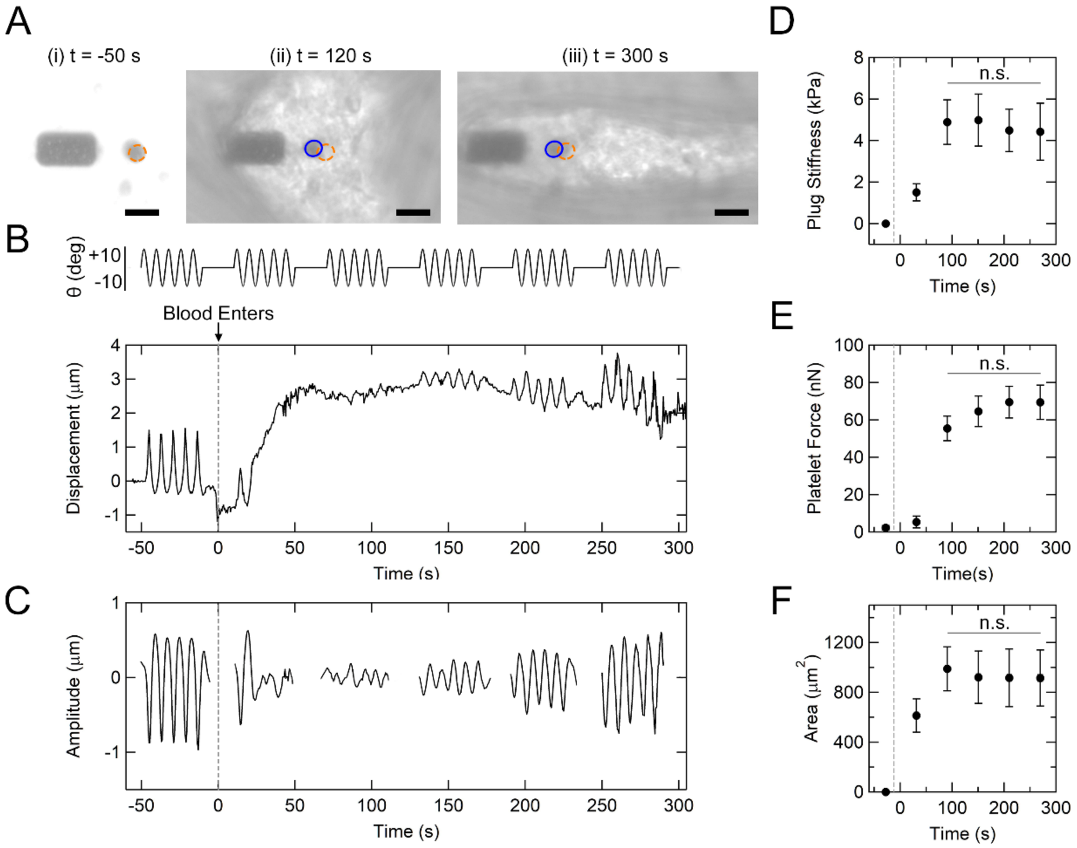

Figure 42. Measurements during platelet plug formation.

To determine the stiffness of a plug, we separated out the amplitude of the deflection during the periods of magnetic actuation (Figure 42C). By assuming that the plug (k_{plug}) and the post (k_{post}) act as two springs in series, we have

$$\mathrm{k_{plug}} = \mathrm{k_{post}} \frac{\mathrm{a_i}}{\mathrm{a_t}} - \mathrm{k_{post}} \tag{16}$$

where a_i initial amplitude prior to blood and a_t is the amplitude of interest. From this, we calculated the plug stiffness to be

$$\mathrm{E_{plug}} = \mathrm{k_{plug}} \frac{\mathrm{L_{eff}}}{\mathrm{A}} \tag{17}$$

where L_{eff} is the effective length of the plug between the block and post, which reduces as the plug contracts. We assumed a plug to be a trapezoidal prism between the block and the post with a thickness of 10 μm and used this to estimate its cross-sectional area (A).

During plug formation, the plug stiffness increased rapidly during the initial aggregation of platelets before reaching an average steady state of 4.7 kPa (Figure 42D). To quantify platelet forces, the time average the centroid displacement data helped isolate the overall deflection of post throughout the experiment. This deflection was multiplied by the post stiffness to quantify the contractile force of the plug (Figure 42E). Similar to the plug stiffness, there was a rapid increase in platelet force before reaching a steady state of 64.8 nN.

From the video frames, the project area of the plug can be measured from the video frames (Figure 42F). As the platelet-rich plug formed, the area exhibited a rapid growth that corresponds to the initial high shear rate. Afterwards, the plug area continued to grow slowly and held steady. In comparison to the mechanical measurements, the initial stiffening of the plug appeared to correspond to the initial aggregation of platelets. This average behavior also revealed the plug stiffened prior to the contraction of platelets but by applying a range of external forces, the interplay between platelet mechanotransduction and the biomechanics of a plug can be decoupled.

6.3.3 Platelet contraction and applied forces modulate plug stiffness.

To decouple the mechanical response, we took the average plug stiffness and platelet force during the steady state of formation. We defined steady state as t = 60 to 300 seconds, because the datapoints during this stage were not significantly different (Figure 42D, E). We found that a plug with higher platelet forces also achieved a higher plug stiffness and there was a strong linear correlation ($R^2 = 0.89$) (Figure 43A). We found that plug stiffened in response to high applied forces ($R^2 = 0.96$) (Figure 43B). We also found platelet forces increased in response to higher applied forces, but this correlation was much weaker ($R^2 = 0.28$) (Figure 43C). By fitting a plan through all three parameters, we found plug stiffness to depend on the applied forces and platelet force ($R^2 = 0.94$) (Figure 43D).

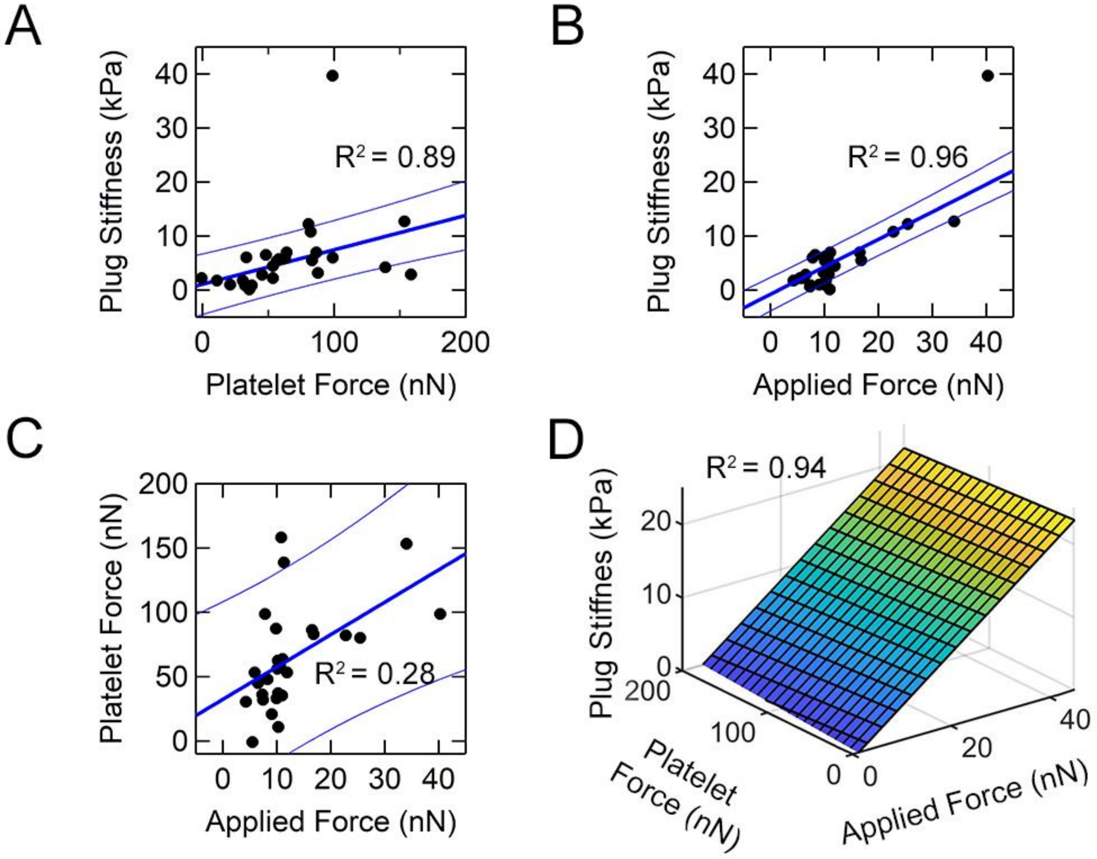

Figure 43. Decoupling the role of platelet forces and applied force on plug stiffness.

To examine the mechanotransduction during formation, we categorized the plugs based on the applied force and examined the stiffness and force dynamics (Figure 44). Plugs either experienced an applied force in the upper (>11.3 nN), middle (9.83-11.3 nN) or lower third (<9.83 nN) range. We found that during the initial adhesion and aggregation of platelets under high shear, plugs stiffened at a greater rate in response to higher applied force. In comparison, the platelet forces, regardless of applied force, remained close to zero. After the shear reduced for the remaining of the experiment, the plugs continued to stiffen and reached a final stiffness indicative of the applied force experienced. At the same time, the plug began to contract and reached a steady state that corresponds to the applied force the plug underwent throughout its formation. The data suggests a distinct mechanotransduction response in which platelets sense the environmental applied force, stiffen during aggregation accordingly, and as a result, produce a contractile force in response to the stiffness. To further study the platelet mechanobiology, we subjected whole blood samples to inhibitions that targeted different aspects of plug formation.

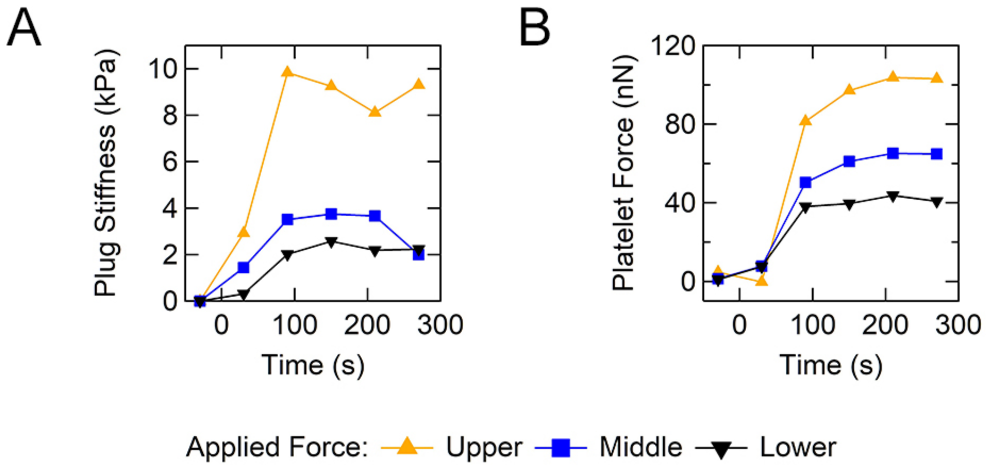

Figure 44. The effect of applied force on platelet force and plug stiffness during formation.

6.3.4 *Inhibition of plug formation reduces the platelet mechanotransduction response.*

Platelet adhesion occurs after globular von Willebrand Factor (VWF) in the blood is elongated by high shear. Elongated VWF can bind to the exposed collagen at the wound site and platelets can bind to VWF. The length of VWF is known to correspond to the platelet binding activity [40]. Thus, to regulate this process and prevent thrombosis, ADAMTS13 is a protease that cleaves VWF to shorten its length [93, 94]. This initial adhesion triggers the recruitment of more platelets through the release of soluble agonist like thromboxane TxA2. The architecture of the plug continues to change as platelets generate myosin-based forces to strengthen its adhesion to the injury site and compact the aggregate. In addition, decreased compaction of a plug reduces the retention of soluble agonists because the plug has higher porosity [55]. Overall, the changes to the plug architecture would also alter the stiffness.

To understand the mechanotransduction response, we either inhibited platelet forces or targeted the plug architecture by antiplatelet treatment and enzymatic cleavage of VWF. Whole blood was either incubated with an inhibitor or acted as a control sample. We used blebbistatin to inhibit non-muscle myosin and observed a reduction in plug stiffness, platelet force, and area (Figure 45A, B, C). Next, we targeted the synthesis of a soluble agonist TxA2 by adding acetylsalicylic acid (ASA), or aspirin, to blood samples. We found that plugs with ASA were also softer, weaker, and smaller. To truly target the formation of the plug, we incubated blood samples with recombinant ADAMTS13. Under high shear gradients, ADAMTS13 will shorten the length of unfolded VWF and lower the platelet binding activity. We found that ADAMTS13-treated plugs also failed to stiffen, contract, or aggregate as much as the control samples. Together, these results indicate the strong relationship between plug stiffness and platelet forces (R2 = 0.98) (Figure 45D).

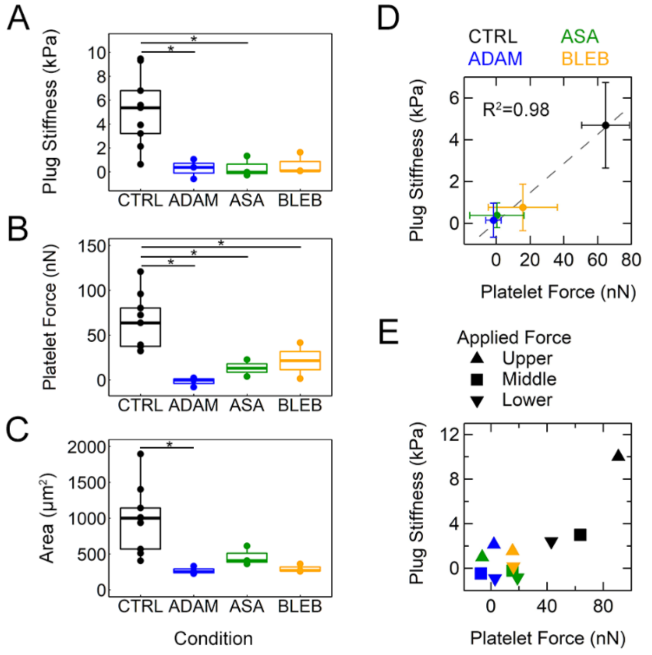

Figure 45. Inhibition studies revealed that adhesion, activation, and contractile are equally important during platelet plug formation. However, under slightly higher applied force, the inhibited plugs exhibited a higher stiffness.

We observed platelet mechanotransduction even in the presence of inhibition (Figure 45E). Here, the plugs either experienced an applied force in the upper (>11.7

nN), middle (8.31-11.3 nN) or lower third (<8.31 nN) range. We found that the control samples generated higher platelet force and stiffened more under the influence of a higher applied force. When whole blood was inhibited with blebbistatin, the myosin-generated platelet forces reduced regardless of applied force. However, the plugs with greater applied force had a higher stiffness. Similarly, blood treated with ADAMTS13 or ASA demonstrated slightly higher stiffness in the presence of applied force.

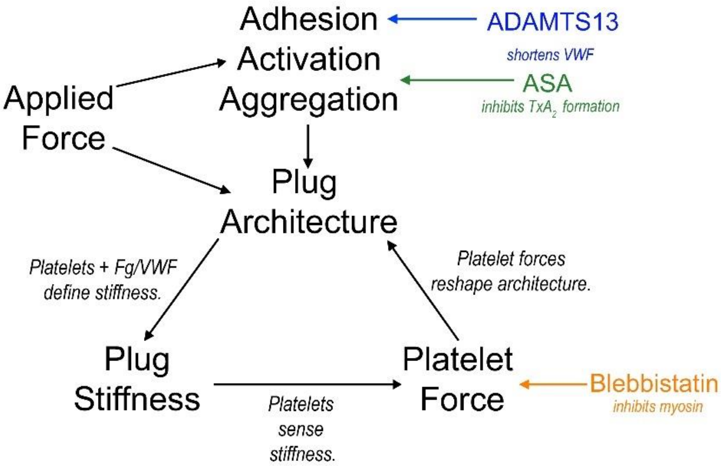

Figure 46. Flow diagram of platelet plug formation and the interplay between biomechanics and mechanobiology.

6.4 Discussion

We assessed platelet mechanotransduction during shear-induced plug formation using a microfluidic assay with an array of magnetic blocks and posts. We found that plug stiffness depends on the external force from the post actuation and the internal platelet contraction. Inhibition attenuated these responses, which indicates the relationship between platelet forces and plug stiffness, but the stiffness of plugs that experienced higher external forces did not diminish completely. Our mechanobiological approach to understanding the dynamics involved during platelet aggregation may have the potential to detect dysfunction that affects primary hemostasis.

This assay takes advantage of magnetic actuation principles that rely on the use of soft magnetic materials and the rotation of a ring magnet to induce a magnetic torque. We chose to embed iron particles into the post like Nagayama et al. [95] rather than cobalt nanowires like Sniadecki et al. [81, 96], magnetite nanoparticles like Evans et al. [85], or a nickel shell like the Superfine group [82, 92]. We integrated this method easily with the soft lithography of our microfluidic assay and found it to produce a higher manufacturing yield of magnetic posts. In contrast to these studies, we chose to rotate an axially oriented multipole ring magnet underneath the assay because it applied a local field in a much more compact design, without the need for controlling high currents through a tightly wound coil around a ferromagnetic core [21]. As Evans et al. modeled previously [85], our posts behaved similarly to a flexible magnetic rod dominated by the field and not the gradient given the distance between our assay and the magnet. We found our posts to bend a similar amount (±5º) given its aspect ratio (4.2:1) and magnetic field, with only batch-to-batch variations in the volume of embedded particles. As a result, we were able to dynamically load the platelet-rich plugs during formation to not only assess stiffening but also differentiate between the magnitude of applied force.

Our measurements of plug mechanical stiffness are on the order of ten kilopascal, which corresponds with prior measurements for single platelet assays and tissue-level elastometry [16, 69, 97, 98]. These measurements are ten times stiffer than platelet rich fibrin clots and hundred times stiffer than platelet free fibrin clots [61, 89], which are indicative of the platelet's contribution. We found our platelet-rich plugs to generate forces in the range of tens to hundreds of nanonewtons, similar to our prior measurements using a nonmagnetic version of this assay [12]. These measurements fall within the range of force produced by single platelets and platelet aggregates [16, 90, 91, 99] but these require agonist-induced activation. Similar to Chen et al. [69], we found that platelet forces and plug stiffness have a strong correlation and inhibition abrogates this response. However, our approach can simultaneously measure platelet forces and plug stiffness during shear-induced aggregation at a faster time scale without the need for collagen tissues, making it beneficial in a rapid diagnostic setting.

Platelets preferentially bind in areas with disturbed flow such as vessel wall damage, partial occlusions, or extreme bends [38, 39]. Tensile forces from the shear unfolds the globular structure of VWF, exposing its binding sites for platelet adhesion [40, 41]. Shear also fosters VWF monomers self-association, increasing its length and platelet binding affinity. To prevent uncontrollable growth, a metalloprotease enzyme ADAMTS13 cleaves unfolded VWF, thereby reducing its hemostatic potential [42-46]. Previous studies have found that high VWF levels and low ADAMTS13 activity in cardiovascular disease [64-67]. Our assay promotes VWF-dependent platelet aggregation, which is inhibited through the addition of recombinant ADAMTS13. This not only emphasizes the potential of ADAMTS13 as a therapeutic drug [63, 100] but also may indicate our assay's sensitivity to early hemostasis specific disorders.

These hemodynamic forces also mechanically stimulate the bond between VWF and the platelet adhesion receptor GPIbα, which upregulates activation and facilitates biomechanical aggregation [19, 47, 49, 101, 102]. Our assay revealed that external force also enhances mechanotransduction response of platelets. We observed that under high shear, plugs stiffened faster under higher external loading and this may have preceded their contraction response. Platelets respond to stiffer environments, around the same order of magnitude as our plugs, with enhanced adhesion, spreading, and activation [58, 59]. Platelet also modulate their fibrin-based architecture through their contraction [60], thereby influencing the overall stiffness [61]. Our data suggests that plug stiffness, not platelet forces, increased with applied force. Because platelet aggregation can unfavorably manifest as arterial thrombosis in areas with extreme shear microgradients, antiplatelet treatments are often used to combat this undesirable outcome. We observed that despite the inhibition, platelet aggregates under the influence of higher mechanical stimulus stiffened more, indicting the potential prothrombotic effects of external force during plug formation. Together, our findings improve our understanding of mechanobiological dynamics involved in the formation of a platelet-rich plug and this assay could potentially be effective in evaluating the early stages of hemostasis in a clinical setting.

7. Summary of Work and Future Outlook

This dissertation focused on approaches for assessment of anemia and bleeding risks for critically ill patients that suffer from cardiovascular disease and trauma-related injuries. Trauma patients suffer from blood loss, which results in anemia, a disease associated with impaired delivery of oxygen throughout the body. In order to stop the bleeding, a stable clot must form at the vascular injury site. In contrast, stiff clots can form occlusions in blood vessels, which lead to cardiovascular diseases like stroke or myocardial infarction. Platelets are the primary mediators of clotting and therefore, evaluating platelet function improves our understanding of bleeding risk.

The goal of the first part of this dissertation was to lay the foundation for a clinically translatable device. Specifically, a benchtop optical platform detected moderate and severe anemia and measured platelet forces in whole blood, flowing through a microfluidic assay. This range of detection is ideal for determining red blood cell transfusion needs. The technology differentiated between healthy blood and blood inhibited with antiplatelet therapy. It also detected bleeding risk and the need for blood transfusion products for trauma patients during a cross-sectional observational trial. Because both aims were done in a microfluidic setting with whole blood using similar optical detection methods, there is further potential to integrate the techniques presented here towards one novel diagnostic tool for hematological assessment.

The goal of the second part of this dissertation was to investigate the mechanobiology of platelets during plug formation. The platelet force sensors became magnetic actuators and a custom magnetic actuation device controlled the movement of these posts. Using these sensors, we dynamically loaded platelet-rich plugs during their formation. We found that internal forces from the contractile platelets and external forces from the magnetic actuators modulated the stiffness of a plug during its formation. The data indicated that the rate of stiffening increased with applied force. In addition, the contractile force response from platelets may have followed the initial increase of stiffness, but further studies are required. By inhibiting different aspects of platelet plug formation, we noticed that both plug stiffness and platelet forces reduced.

However, the plugs that experienced higher force exhibited a higher stiffness, suggesting inhibition does not necessarily target the mechanotransduction response. Additional studies exploring the role of other receptors could provide better understanding of the role of mechanotransduction during platelet-rich plug formation.

The magnetic actuators within the microfluidic assay adds an extra layer of assessment to the original design. Future work can look towards integrating magnetics into the optical detection assays. One possible avenue for improvement is utilizing magnetic sensors. While I do not believe magnetic sensors can evaluate the deflection of individual posts, it might be possible to detect the sum of all block-post sensors if the scaled-up design is used with neodymium-based powder. If possible, this would completely eliminate the need for optical detection and image analysis but at a cost of requiring more blood volume. Another possible avenue of research for the magnetic actuators is measuring adhesive or rupture force of platelet-rich plugs, but in my preliminary attempts, I failed to pull on a plug with enough force to cause breakdown. Finally, this work only evaluated plugs for elastic modulus using quasi-static dynamic loading. Further design improvements could allow for the assessment of plugs using different frequencies to determine the viscoelastic properties.

While this work only demonstrated the use of providing platelet force as a metric to evaluate bleeding risk for trauma patients, there is also potential to include plug stiffness. Under dynamic loading, platelet forces did not change as much as plug stiffness, indicating the mechanotransduction response during early hemostasis. Because plugs experience hemodynamic forces, knowledge of both plug stiffness and contractile force from platelets could aid doctors in better treatment. Furthermore, the magnetic actuation assay could evaluate the role of VWF and ADAMTS13 in plug formation because of the use of shear to facilitate platelet aggregation. This could lend insight on prothrombotic risks that are difficult to detect with current clinical tools as well as the potential use of ADAMTS13 as a therapeutic drug.

REFERENCES

1. Drews, R.E., *Critical issues in hematology: anemia, thrombocytopenia, coagulopathy, and blood product transfusions in critically ill patients.* Clin Chest Med, 2003. **24**(4): p. 607-22.
2. Zimmerman, L.H., *Causes and consequences of critical bleeding and mechanisms of blood coagulation.* Pharmacotherapy, 2007. **27**(9 Pt 2): p. 45S-56S.
3. Menendez, C., A.F. Fleming, and P.L. Alonso, *Malaria-related anaemia.* Parasitology Today, 2000. **16**(11): p. 469-476.
4. Kadima, B.T., et al., *High rate of sickle cell anaemia in Sub-Saharan Africa underlines the need to screen all children with severe anaemia for the disease.* Acta Paediatrica, 2015. **104**(12): p. 1269-1273.
5. Kateera, F., et al., *Malaria, anaemia and under-nutrition: three frequently co-existing conditions among preschool children in rural Rwanda.* Malaria Journal, 2015. **14**.
6. Nair, K.M., et al., *Characterisation of anaemia and associated factors among infants and pre-schoolers from rural India.* Public Health Nutrition, 2016. **19**(5): p. 861-871.
7. Jackson, S.P., *Arterial thrombosis-insidious, unpredictable and deadly.* Nature Medicine, 2011. **17**(11): p. 1423-1436.
8. Spahn, D.R., et al., *Management of bleeding and coagulopathy following major trauma: an updated European guideline.* Crit Care, 2013. **17**(2): p. R76.
9. Balarajan, Y., et al., *Anaemia in low-income and middle-income countries.* Lancet, 2011. **378**(9809): p. 2123-2135.
10. McLean, E., et al., *Worldwide prevalence of anaemia, WHO Vitamin and Mineral Nutrition Information System, 1993-2005.* Public Health Nutrition, 2009. **12**(4): p. 444-454.
11. Tomaiuolo, M., L.F. Brass, and T.J. Stalker, *Regulation of Platelet Activation and Coagulation and Its Role in Vascular Injury and Arterial Thrombosis.* Interv Cardiol Clin, 2017. **6**(1): p. 1-12.
12. Ting, L.H., et al., *Contractile forces in platelet aggregates under microfluidic shear gradients reflect platelet inhibition and bleeding risk.* Nat Commun, 2019. **10**(1): p. 1204.
13. Bain, B.J., *Blood Cells: A Practical Guide*2015: Wiley-Blackwell.
14. Lewis, S.M., et al., *Lauryl sulphate haemoglobin: a non-hazardous substitute for HiCN in haemoglobinometry.* Clin Lab Haematol, 1991. **13**(3): p. 279-90.
15. MD, W., *Blood pressure in trauma resuscitation: 'pop the clot' vs. 'drain the brain'?* Anaesthesia, 2017. **72**(12): p. 1448-1455.
16. Lam, W.A., et al., *Mechanics and contraction dynamics of single platelets and implications for clot stiffening.* Nat Mater, 2011. **10**(1): p. 61-6.
17. Qiu, Y., et al., *Platelets and physics: How platelets "feel" and respond to their mechanical microenvironment.* Blood Rev, 2015. **29**(6): p. 377-86.
18. Zhang, Y., et al., *Platelet integrins exhibit anisotropic mechanosensing and harness piconewton forces to mediate platelet aggregation.* Proc Natl Acad Sci U S A, 2018. **115**(2): p. 325-330.

19. Chen, Y., et al., *An integrin alphaIIbbeta3 intermediate affinity state mediates biomechanical platelet aggregation.* Nat Mater, 2019. **18**(7): p. 760-769.
20. Sniadecki NJ, A.A., Yang MT, Lamb CM, Liu Z, Kirschner SB, Liu Y, Reich DH, Chen CS, *Magnetic microposts as an approach to apply forces to living cells.* Proceedings of the National Academy of Sciences of the United States of America, 2007. **104**(37): p. 14553-8.
21. Bielawski, K.S. and N.J. Sniadecki, *A Magnetic Post Approach for Measuring the Viscoelasticity of Biomaterials.* JOURNAL OF MICROELECTROMECHANICAL SYSTEMS, 2016. **25**(1): p. 153-159.
22. Judith RM, F.J., Spero RC, Fiser BL, Turner A, Oberhardt B, Taylor RM, Falvo MR, Superfine R., *Micro-elastometry on whole blood clots using actuated surface-attached posts (ASAPs).* Lab on a Chip, 2015. **15**(5): p. 1385-1393.
23. Camaschella, C., *Iron-deficiency anemia.* N Engl J Med, 2015. **372**(19): p. 1832-43.
24. Rees, D.C., T.N. Williams, and M.T. Gladwin, *Sickle-cell disease.* Lancet, 2010. **376**(9757): p. 2018-31.
25. Docherty, A.B. and T.S. Walsh, *Anemia and blood transfusion in the critically ill patient with cardiovascular disease.* Crit Care, 2017. **21**(1): p. 61.
26. Drabkin, D.L. and J.H. Austin, *Spectrophotometric studies II. Preparations from washed blood cells; nitric oxide hemoglobin and sulfhemoglobin.* Journal of Biological Chemistry, 1935. **112**(1): p. 51-65.
27. Munoz, M., et al., *Utility of point-of-care haemoglobin measurement in the HemoCue-B haemoglobin for the initial diagnosis of anaemia.* Clin Lab Haematol, 2005. **27**(2): p. 99-104.
28. Zhu, H.Y., et al., *Cost-effective and rapid blood analysis on a cell-phone.* Lab on a Chip, 2013. **13**(7): p. 1282-1288.
29. Guo, T., et al., *Smartphone dongle for simultaneous measurement of hemoglobin concentration and detection of HIV antibodies.* Lab on a Chip, 2015. **15**(17): p. 3514-20.
30. Bond, M., et al., *Chromatography paper as a low-cost medium for accurate spectrophotometric assessment of blood hemoglobin concentration.* Lab on a Chip, 2013. **13**(12): p. 2381-2388.
31. Yang, X.X., et al., *Simple Paper-Based Test for Measuring Blood Hemoglobin Concentration in Resource-Limited Settings.* Clinical Chemistry, 2013. **59**(10): p. 1506-1513.
32. Steigert, J., et al., *Direct hemoglobin measurement on a centrifugal microfluidic platform for point-of-care diagnostics.* Sensors and Actuators a-Physical, 2006. **130**: p. 228-233.
33. Hou, H.W., et al., *Deformability based cell margination-A simple microfluidic design for malaria-infected erythrocyte separation.* Lab on a Chip, 2010. **10**(19): p. 2605-2613.
34. Shelby, J.P., et al., *A microfluidic model for single-cell capillary obstruction by Plasmodium falciparum infected erythrocytes.* Proceedings of the National Academy of Sciences of the United States of America, 2003. **100**(25): p. 14618-14622.

35. Kassebaum, N.J., et al., *A systematic analysis of global anemia burden from 1990 to 2010.* Blood, 2014. **123**(5): p. 615-24.
36. Kassebaum, N.J., *The Global Burden of Anemia.* Hematol Oncol Clin North Am, 2016. **30**(2): p. 247-308.
37. Taparia, N., et al., *A microfluidic approach for hemoglobin detection in whole blood.* AIP Advances, 2017. **7**(10): p. 105102.
38. Nesbitt, W.S., et al., *A shear gradient-dependent platelet aggregation mechanism drives thrombus formation.* Nat Med, 2009. **15**(6): p. 665-73.
39. Tovar-Lopez, F.J., et al., *A microfluidics device to monitor platelet aggregation dynamics in response to strain rate micro-gradients in flowing blood.* Lab on a Chip, 2010. **10**(3): p. 291-302.
40. Springer, T.A., *von Willebrand factor, Jedi knight of the bloodstream.* Blood, 2014. **124**(9): p. 1412-25.
41. Gogia, S. and S. Neelamegham, *Role of fluid shear stress in regulating VWF structure, function and related blood disorders.* Biorheology, 2015. **52**(5-6): p. 319-35.
42. Nieswandt, B. and G. Stoll, *The smaller, the better: VWF in stroke.* Blood, 2010. **115**(8): p. 1477-8.
43. Chen, J., et al., *Simultaneous exposure of sites in von Willebrand factor for glycoprotein Ib binding and ADAMTS13 cleavage: studies with ristocetin.* Arterioscler Thromb Vasc Biol, 2012. **32**(11): p. 2625-30.
44. Kragh, T., et al., *High shear dependent von Willebrand factor self-assembly fostered by platelet interaction and controlled by ADAMTS13.* Thromb Res, 2014. **133**(6): p. 1079-87.
45. Lippok, S., et al., *Shear-Induced Unfolding and Enzymatic Cleavage of Full-Length VWF Multimers.* Biophys J, 2016. **110**(3): p. 545-554.
46. Zhang, C., A. Kelkar, and S. Neelamegham, *von Willebrand factor self-association is regulated by the shear-dependent unfolding of the A2 domain.* Blood Adv, 2019. **3**(7): p. 957-968.
47. Ju, L., et al., *Cooperative unfolding of distinctive mechanoreceptor domains transduces force into signals.* Elife, 2016. **5**.
48. Kasirer-Friede, A., et al., *Signaling through GP Ib-IX-V activates alpha IIb beta 3 independently of other receptors.* Blood, 2004. **103**(9): p. 3403-11.
49. Mazzucato, M., et al., *Sequential cytoplasmic calcium signals in a 2-stage platelet activation process induced by the glycoprotein Ibalpha mechanoreceptor.* Blood, 2002. **100**(8): p. 2793-800.
50. Andrews, R.K. and M.C. Berndt, *Platelet adhesion: a game of catch and release.* J Clin Invest, 2008. **118**(9): p. 3009-11.
51. Johnson, G.J., et al., *The critical role of myosin IIA in platelet internal contraction.* J Thromb Haemost, 2007. **5**(7): p. 1516-29.
52. Weisel, J.W., *Structure of fibrin: impact on clot stability.* J Thromb Haemost, 2007. **5 Suppl 1**: p. 116-24.
53. Weisel, J.W., *Biomechanics in hemostasis and thrombosis.* J Thromb Haemost, 2010. **8**(5): p. 1027-9.

54. Welsh, J.D., et al., *A systems approach to hemostasis: 4. How hemostatic thrombi limit the loss of plasma-borne molecules from the microvasculature.* Blood, 2016. **127**(12): p. 1598-1605.
55. Welsh, J.D., et al., *A systems approach to hemostasis: 1. The interdependence of thrombus architecture and agonist movements in the gaps between platelets.* Blood, 2014. **124**(11): p. 1808-1815.
56. Stalker, T.J., et al., *A systems approach to hemostasis: 3. Thrombus consolidation regulates intrathrombus solute transport and local thrombin activity.* Blood, 2014. **124**(11): p. 1824-31.
57. Stalker, T.J., et al., *Hierarchical organization in the hemostatic response and its relationship to the platelet-signaling network.* Blood, 2013. **121**(10): p. 1875-85.
58. Qiu, Y., et al., *Platelet mechanosensing of substrate stiffness during clot formation mediates adhesion, spreading, and activation.* Proc Natl Acad Sci U S A, 2014. **111**(40): p. 14430-5.
59. Kee, M.F., et al., *Platelet mechanosensing of collagen matrices.* PLoS One, 2015. **10**(4): p. e0126624.
60. Kim, O.V., et al., *Quantitative structural mechanobiology of platelet-driven blood clot contraction.* Nat Commun, 2017. **8**(1): p. 1274.
61. Jen, C.J. and L.V. McIntire, *The structural properties and contractile force of a clot.* Cell Motil, 1982. **2**(5): p. 445-55.
62. Tutwiler, V., et al., *Blood clot contraction differentially modulates internal and external fibrinolysis.* J Thromb Haemost, 2019. **17**(2): p. 361-370.
63. Denorme, F., et al., *ADAMTS13-mediated thrombolysis of t-PA-resistant occlusions in ischemic stroke in mice.* Blood, 2016. **127**(19): p. 2337-45.
64. Bongers, T.N., et al., *Lower levels of ADAMTS13 are associated with cardiovascular disease in young patients.* Atherosclerosis, 2009. **207**(1): p. 250-4.
65. Sonneveld, M.A., M.P. de Maat, and F.W. Leebeek, *Von Willebrand factor and ADAMTS13 in arterial thrombosis: a systematic review and meta-analysis.* Blood Rev, 2014. **28**(4): p. 167-78.
66. Sonneveld, M.A., et al., *Von Willebrand Factor, ADAMTS13, and the Risk of Mortality: The Rotterdam Study.* Arterioscler Thromb Vasc Biol, 2016. **36**(12): p. 2446-2451.
67. Tahir, S.M., N.; Chauhdry, A.; Mustafa, G.; Hussain, S.; Shahzad, F.; Mohsin, S. , *Comparison of levels of von Willebrand factor and ADAMTS13 in Patients of Myocardial Infarction and Healthy Controls.* Journal of Rawalpindi Medical College 2019. **23**(1): p. 25-29.
68. Myers, D.R., et al., *Single-platelet nanomechanics measured by high-throughput cytometry.* Nat Mater, 2017. **16**(2): p. 230-235.
69. Chen, Z., et al., *Microclot array elastometry for integrated measurement of thrombus formation and clot biomechanics under fluid shear.* Nat Commun, 2019. **10**(1): p. 2051.
70. Stevens, G.A., et al., *Global, regional, and national trends in haemoglobin concentration and prevalence of total and severe anaemia in children and pregnant and non-pregnant women for 1995-2011: a systematic analysis of population-representative data.* Lancet Global Health, 2013. **1**(1): p. E16-E25.

71. Pasricha, S.R., *Anemia: a comprehensive global estimate.* Blood, 2014. **123**(5): p. 611-2.
72. Steinke, J.M. and A.P. Shepherd, *Diffusion-Model of the Optical Absorbance of Whole-Blood.* Journal of the Optical Society of America a-Optics Image Science and Vision, 1988. **5**(6): p. 813-822.
73. Hammer, M., et al., *Single scattering by red blood cells.* Applied Optics, 1998. **37**(31): p. 7410-7418.
74. Friebel, M., et al., *Influence of shear rate on the optical properties of human blood in the spectral range 250 to 1100 nm.* Journal of Biomedical Optics, 2007. **12**(5).
75. Billett, H.H., *Hemoglobin and Hematocrit*, in *Clinical Methods: The History, Physical, and Laboratory Examinations*, H.K. Walker, Hall, W.D., Hurst, J.W., Editor 1990, Butterworth Publishers: Boston.
76. Bland, J.M. and D.G. Altman, *Statistical Methods for Assessing Agreement between Two Methods of Clinical Measurement.* Lancet, 1986. **1**(8476): p. 307-310.
77. Zdrojkowski, R.J. and N.R. Pisharoty, *Optical Transmission and Reflection by Blood.* Ieee Transactions on Biomedical Engineering, 1970. **Bm17**(2): p. 122-+.
78. Barbee, J.H. and G.R. Cokelet, *The Fahraeus effect.* Microvasc Res, 1971. **3**(1): p. 6-16.
79. Gascoyne, P., J. Satayavivad, and M. Ruchirawat, *Microfluidic approaches to malaria detection.* Acta Tropica, 2004. **89**(3): p. 357-369.
80. Wang, T.Y., et al., *Cluster-randomized clinical trial examining the impact of platelet function testing on practice: the treatment with adenosine diphosphate receptor inhibitors: longitudinal assessment of treatment patterns and events after acute coronary syndrome prospective open label antiplatelet therapy study.* Circ Cardiovasc Interv, 2015. **8**(6): p. e001712.
81. Sniadecki, N.J., et al., *Magnetic microposts as an approach to apply forces to living cells.* Proc Natl Acad Sci U S A, 2007. **104**(37): p. 14553-8.
82. Judith, R.M., et al., *Micro-elastometry on whole blood clots using actuated surface-attached posts (ASAPs).* Lab on a Chip, 2015. **15**(5): p. 1385-93.
83. Shahrivar, K., et al., *Aggregation kinetics of carbonyl iron based magnetic suspensions in 2D.* Soft Matter, 2017. **13**(14): p. 2677-2685.
84. Abbott, J.J., Ergeneman, O., Kummer, M.P., Hirt, A. M., Nelson, B.J. , *Modeling Magnetic Torque and Force for Controlled Manipulation of Soft-Magnetic Bodies.* IEEE Transactions on Robotics, 2007. **23**(6): p. 1247-1252.
85. Evans, B.A., et al., *Magnetically actuated nanorod arrays as biomimetic cilia.* Nano Lett, 2007. **7**(5): p. 1428-34.
86. Ono, A., et al., *Identification of a fibrin-independent platelet contractile mechanism regulating primary hemostasis and thrombus growth.* Blood, 2008. **112**(1): p. 90-9.
87. Gorog, D.A., Z.A. Fayad, and V. Fuster, *Arterial Thrombus Stability: Does It Matter and Can We Detect It?* J Am Coll Cardiol, 2017. **70**(16): p. 2036-2047.
88. Carr, M.E., Jr. and S.L. Carr, *Fibrin structure and concentration alter clot elastic modulus but do not alter platelet mediated force development.* Blood Coagul Fibrinolysis, 1995. **6**(1): p. 79-86.

89. Shah, J.V., Janmey, P.A., *Strain hardening of fibrin gels and plasma clots.* Rheologica Acta, 1997. **36**(3): p. 262-268.
90. Feghhi, S., et al., *Glycoprotein Ib-IX-V Complex Transmits Cytoskeletal Forces That Enhance Platelet Adhesion.* Biophys J, 2016. **111**(3): p. 601-608.
91. Feghhi, S., W.W. Tooley, and N.J. Sniadecki, *Nonmuscle Myosin IIA Regulates Platelet Contractile Forces Through Rho Kinase and Myosin Light-Chain Kinase.* J Biomech Eng, 2016. **138**(10).
92. Fiser, B.L., et al., *Highly responsive core-shell microactuator arrays for use in viscous and viscoelastic fluids.* J Micromech Microeng, 2015. **25**(2).
93. Crawley, J.T., et al., *Unraveling the scissile bond: how ADAMTS13 recognizes and cleaves von Willebrand factor.* Blood, 2011. **118**(12): p. 3212-21.
94. Dong, J.F., et al., *ADAMTS-13 rapidly cleaves newly secreted ultralarge von Willebrand factor multimers on the endothelial surface under flowing conditions.* Blood, 2002. **100**(12): p. 4033-9.
95. Nagayama, K., et al., *A novel patterned magnetic micropillar array substrate for analysis of cellular mechanical responses.* J Biomech, 2017. **65**: p. 194-202.
96. Sniadecki, N.J., et al., *Magnetic microposts for mechanical stimulation of biological cells: fabrication, characterization, and analysis.* Rev Sci Instrum, 2008. **79**(4): p. 044302.
97. Radmacher, M., et al., *Measuring the viscoelastic properties of human platelets with the atomic force microscope.* Biophys J, 1996. **70**(1): p. 556-67.
98. Rheinlaender, J., et al., *Imaging the elastic modulus of human platelets during thrombin-induced activation using scanning ion conductance microscopy.* Thromb Haemost, 2015. **113**(2): p. 305-11.
99. Liang, X.M., et al., *Platelet retraction force measurements using flexible post force sensors.* Lab on a Chip, 2010. **10**(8): p. 991-8.
100. Eerenberg, E.S. and M. Levi, *The potential therapeutic benefit of targeting ADAMTS13 activity.* Semin Thromb Hemost, 2014. **40**(1): p. 28-33.
101. Nesbitt, W.S., et al., *Distinct glycoprotein Ib/V/IX and integrin alpha IIbbeta 3-dependent calcium signals cooperatively regulate platelet adhesion under flow.* Journal of Biological Chemistry, 2002. **277**(4): p. 2965-72.
102. Goncalves, I., et al., *Importance of temporal flow gradients and integrin alphaIIbbeta3 mechanotransduction for shear activation of platelets.* Journal of Biological Chemistry, 2005. **280**(15): p. 15430-7.

APPENDIX A: ADDITIONAL PLATELET STUDIES

Over the course of my graduate work, I also conducted preliminary studies to explore the role of the calcium dependent and independent pathways during platelet plug formation. The premise of this work began with recording calcium levels using 10 µM Fluo-3 AM, a fluorscence marker that only attaches to calcium after it enters the membrane of a cell. The fluorscence dye was inhibited into the blood for 30 minutes at 37 degrees. Afterwards, the blood flowed through the block and post assay and instead of just imaging the phase and red fluorscence of the posts, the NIS software also tracked the green fluorscence signal of the calcium ever 5 seconds. After the experiments, I wrote a custom code to create a heatmap that tracked the calcium fluorscence relative to the background and the maximum calcium signal (Figure 47). From the imaging, two things weere noticeable: (1) there were two calcium spikes that occurred and (2) the calcium progated from the center of the plug outwards, with the highest calcium signal in the center. The two spikes only appearing in blood collected with a sodium citrate vacutainer and not in heparin blood. The reason for the two spikes remained a relative mystery although we hypothesized that the first and second calcium signal were due to the engagement of the platelet adhesion and signalling receptors, respectively.

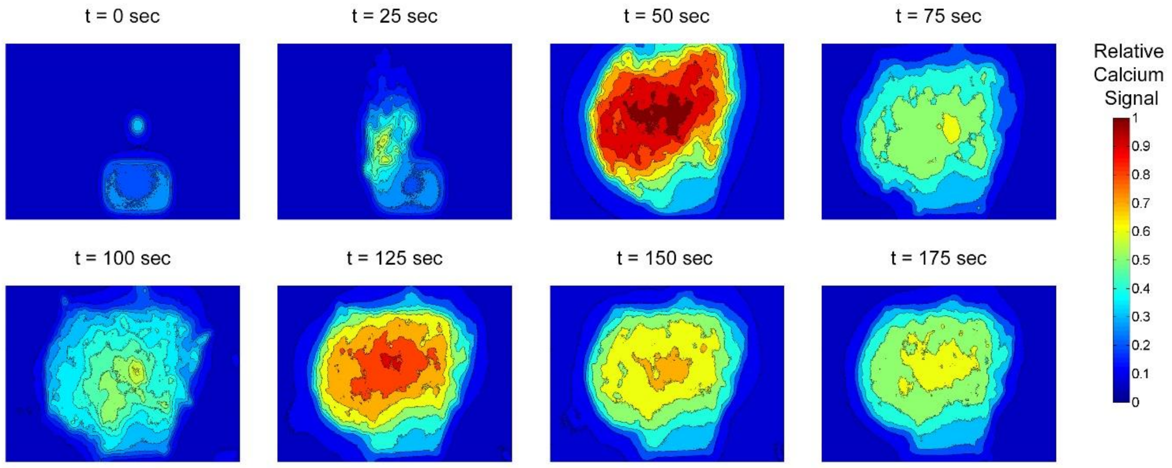

Figure 47. Calcium heatmap of a platelet plug using Fluo-3 AM.

The myosin-based contractile forces during platelet plug formation can occur from two pathways, calcium dependent and indepdent. These pathways lead to myosin phosphorylation within a platelet (Figure 48). It is well documented that engaged adhesion and signaling receptors creates an internal calcium increase, which activates myosin light chain kinase (MLCK). It is also documented that rho-kinase (ROCK), which does not require calcium, can lead to myosin phosphorylation within a platelet. The MLCK pathway is often associated with platelet shape change and activation, while the ROCK pathway is associated with contraction and secretion.

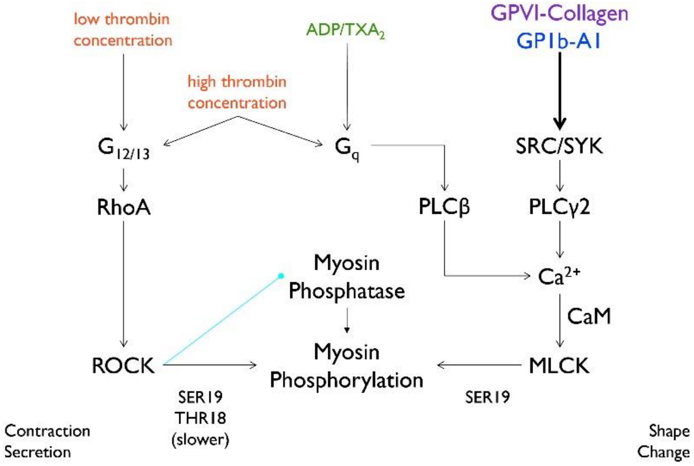

Figure 48. Two pathways of myosin phosphorylation within a platelet.

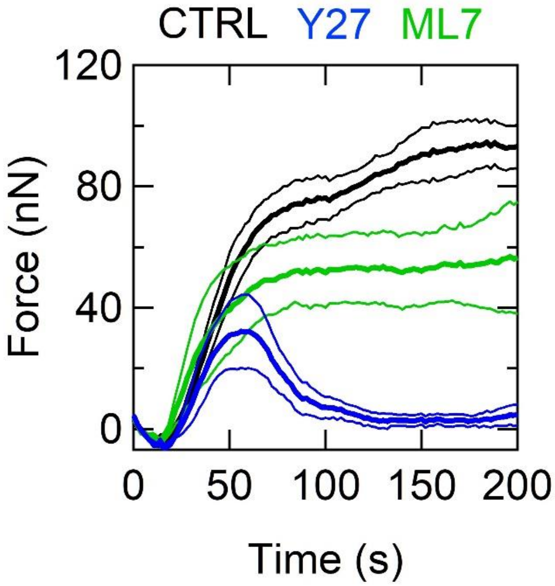

Figure 49. Inhibition of MLCK and ROCK during platelet plug formation.

To study these two pathways, I inhibited control blood with 20 µM ML-7 and 50 µM Y-27632 to target MLCK and ROCK, respectively, and repeated these experiments for four donors (Figure 49). In terms of the platelet force, the presence of only the MLCK pathway (Y-27632 inhibition) resulted in the initial growth and contraction of platelets. In contrast, the presence of only the ROCK pathway (inhibition with ML-7) produced plugs that sustained their contractile force but to a lesser degree in comparison to the control. This could also be seen through phase images (Figure 50). The plugs that only possessed the MLCK pathway (inhibition with Y-27632) did not have the same geometrical shape during platelet plug formation. While this was the extent of the preliminary experiments, it does depict the importance of both pathways during the dynamic process of platelet plug formation.

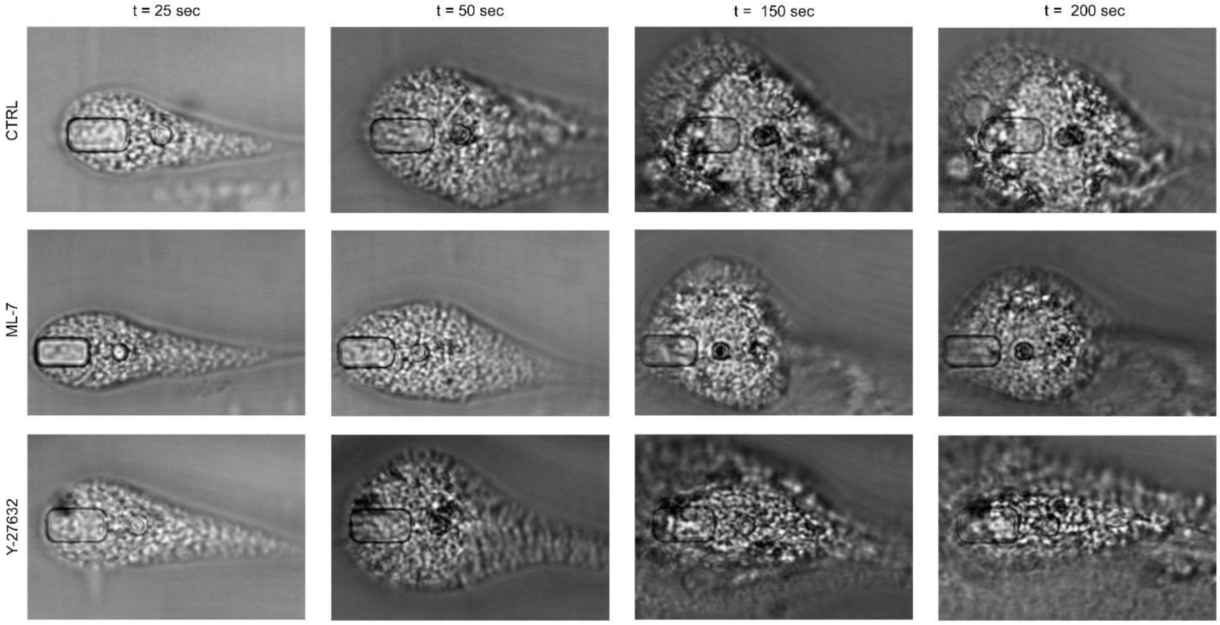

Figure 50. Phase images during the inhibition of MLCK and ROCK

APPENDIX B: TOTAL ENERGY OF A MAGNETIC POST

The purpose of this section is to demonstrate the derivation for the total energy of a bent, cantilever rod that has an elastic base and magnetic tip (Figure 29). The elastic energy of a rod bent from equilibrium is defined by Kirchhoff's model,

$$U_e = \frac{1}{2}EI\int_0^L \frac{1}{R(s)}ds$$

where *E* is the Young's modulus, *I* is the inertia for a cylindrical rod, and *R(s)* is the radius of curvature of a bent rod. The model assumes the radius of curvature is constant,

$$R(s) = R = {}^{L}\!/_{2\phi}$$

where *L* is the length of the rod and ϕ is the angle of the bent rod from the vertical axis. Because only the elastic base can bend, the elastic energy of the system can be rewritten as

$$U_e = \frac{\pi}{2}\frac{Er^4}{L_e}\phi^2.$$

The magnetic energy of the rod is denoted as

$$U_m = -A\int_0^L \boldsymbol{B_T}(s)\cdot\boldsymbol{M}(s)ds \ \ where\ \boldsymbol{B_T} = \boldsymbol{B_N} + \boldsymbol{B_I} + \boldsymbol{B_A}\ .$$

Here, *A* is the cross-sectional area of the rod, ***M*** is the magnetization at a point along the length of the rod, and $\mathbf{B_N}$, $\mathbf{B_I}$, and $\mathbf{B_A}$ correspond to the magnetic field from neighboring objects, the internal field and the applied external field. While there is the possibility for nearest neighbor effects from the magnetic material in the block, it was not experimentally observable for our assay. The nearest neighbor effects become more prevalent as you scale the device to a larger size.

The internal energy is described using Stoner-Wohlfarth model for an ellipsoid,

$$U_I = \frac{1}{2}u_0\frac{m^2}{V}(n_a - n_r)\cos^2(\alpha - \phi)\ \ where\ m = M(B)Vf.$$

For the internal magnetic energy, α is the angle from the vertical axis of the magnetic dipole moment from the magnetic tip. However, this angle becomes ψ if the dipole moment aligns with the magnetic field, which is the case in our system.

The energy due to an applied field is denoted as

$$U_A = -A\int_0^L B_A M(B)dl$$

where $B(l)$ can be expanded using series expansion and simplified to the first two terms due to the size of the rod, as shown below.

$$B(l) = B_0 + \nabla Bl\cos(\psi' - \phi) + 2l^2\frac{\partial(\nabla B)}{\partial l} + \cdots \approx B_0 + \nabla Bl\cos(\psi' - \phi).$$

The term ψ' is the angle of the gradient of the field with respect to the vertical axis. The magnetization of the material, $M(B) = \chi B(l)$, can be substituted into the expression for magnetic energy,

$$U_A = -A\chi\int_0^{L_m}(B_0 + \nabla Bl\cos(\psi' - \phi))^2 dl$$

and it can further be simplified if we consider the ratio between the applied field and the gradient of the field where the maximum length of the magnetic section is 25 µm, the maximum field gradient is approximately 150 T/m and the maximum field is approximately 300 mT. The ratio between the two terms as shown below demonstrates which term is more dominant if you were to expand the expression.

$$\frac{B}{\nabla Bl} = \frac{(0.3\,T)}{(150\,T/m)(0.000025)}\ or\ B \gg \nabla Bl$$

The expression for energy due to an applied field becomes

$$U_A = -A\chi L_m B_0\left(B_0 + \frac{1}{2}\nabla BL_m\cos(\psi' - \phi)\right) = -\frac{1}{2}m\nabla BL_m\cos(\psi' - \phi)$$

Therefore, the total energy of a flexible cantilever rod with an elastic base and a magnetic tip is

$$U_T = \frac{\pi}{2}\frac{Er^4}{L_e}\phi^2 + \frac{1}{2}u_0\frac{m^2}{V}(n_a - n_r)\cos^2(\psi - \phi) - \frac{1}{2}m\nabla BL_m\cos(\psi' - \phi).$$

In the dissertation, the total energy of the system is minimized to find the equilibrium point for the post deflection angle given different magnetic fields and magnetic lengths. Lastly, if the magnetic post were closer to the magnet, the gradient of the field would dominate the movement.